Università di Genova

UNIVERSITY OF GENOVA

PHD PROGRAM IN BIOENGINEERING AND ROBOTICS

MODELLING AND CONTROL OF CABLE-DRIVEN HYPER-REDUNDANT ROBOTS

by

Daniele Ludovico

Thesis submitted for the degree of *Doctor of Philosophy* (33° cycle)

April 2021

PhD Carlo Canali	Supervisors
PhD Ferdinando Cannella	
Prof. Darwin G. Caldwell	
Prof. Giorgio Cannata	Head of the PhD program

Thesis Jury:

Prof. David Scaradozzi	*Univerità Politecnica delle Marche*
Prof. Nicola Vitiello	*Scuola Superiore Sant'Anna*

A Barbara, Rossella e Nicola.
La mia famiglia.

Declaration

I hereby declare that except where specific reference is made to the work of others, the contents of this dissertation are original and have not been submitted in whole or in part for consideration for any other degree or qualification in this, or any other university. This dissertation is my own work and contains nothing which is the outcome of work done in collaboration with others, except as specified in the text and Acknowledgements. This dissertation contains fewer than 65,000 words including appendices, bibliography, footnotes, tables and equations and has fewer than 150 figures.

Daniele Ludovico
20th April 2021

ACKNOWLEDGEMENTS

When you reach the end of a long and demanding journey like attaining a PhD, it is natural to stop and reflect on experiences made. In these three years, I have had the chance to grow both professionally and humanly thanks to the support and guidance of all the people who have shared this path with me. First, I would like to thank Prof. Darwin G. Caldwell and PhD Ferdinando Cannella for believing in my potential by giving me the possibility of attending the PhD at the Italian Institute of Technology. I should then express my gratitude to PhD Carlo Brindesi Canali, who welcomed me into his group by giving me a purpose. Without your help, I would have been lost. I also wish to address a special thanks to PhD Jinoh Lee. With your kindness and availability, you taught me the meaning of honouring commitments. I should dedicate heartfelt thanks to Paolo, a colleague and especially a friend, without whom I would never have reached the end of this journey. You are an invaluable companion. A warm thank goes to Alessandro, the mainstay of the group. Even in hard times, you show me a way to cope with troubles with a smile. I wish sincerely to thank Roberto. You taught me modesty and commitment. I should dedicate a genuine thanks to Cristiano. You will always be a witness of consistency. I wish to thanks also all the people who have been part of AIAL. You helped me to live each day with joy. A respectful thank also goes to all the technical and administrative staff of IIT. In those years, they have always supported me and made it possible to achieve this goal. Finally, I wish to thank my mother, father, and sister because they never made me miss their love and support.

RINGRAZIAMENTI

Quando si arriva alla fine di un percorso lungo e impegnativo come quello che si intraprende affrontando un dottorato viene naturale fermarsi per riflettere sulle esperienze vissute. In questi tre anni mi è stata data l'opportunità di crescere, sia a livello professionale che umano, grazie al sostegno e alla guida di tutte le persone che hanno condiviso con me anche solo una piccola parte di questo percorso. Desidero innanzitutto ringraziare il Professor Darwin G. Caldwell e il Dottor Ferdinando Cannella per aver creduto nelle mie potenzialità dandomi la possibilità di svolgere il dottorato presso l'Istituto Italiano di Tecnologia. Vorrei rivolgere un ringraziamento speciale al Dottor Carlo Brindesi Canali che ha saputo accogliermi nel suo gruppo dandomi un obbiettivo da perseguire. Senza il tuo aiuto mi sarei perso. Desidero inoltre esprimere la mia gratitudine al Dottor Jinoh Lee. Con la tua gentilezza e disponibilità hai saputo insegnarmi cosa vuol dire onorare un impegno dedicandovi anima e corpo. Vorrei ringraziare dal più profondo del cuore Paolo, collega, ma soprattutto amico, senza il quale non sarei mai riuscito ad arrivare alla fine di questo percorso. Sei per me un compagno insostituibile. Un caloroso ringraziamento va ad Alessandro, pilastro di questo gruppo. Anche nei periodi più difficili, sei riuscito a farmi ricordare come un sorriso faccia percorrere molta più strada di un brontolio. Vorrei ringraziare sinceramente Roberto. Sei stato per me maestro di umiltà e dedizione. Desidero dedicare un profondo ringraziamento a Cristiano. Per me sarai sempre testimone di coerenza e punto di riferimento. Un sentito ringraziamento va anche a tutte le persone che hanno fatto parte di AIAL. Mi avete aiutato a vivere con allegria ogni giornata. Un doveroso ringraziamento va anche a tutto il personale tecnico

e amministrativo di IIT che in questi anni mi ha sempre supportato e ha reso possibile il raggiungimento di questo traguardo. Infine, vorrei ringraziare mia madre, mio padre e mia sorella per l'amore, l'affetto e il sostegno che non mi hanno mai fatto mai mancare.

ABSTRACT

Nowadays, inspection and maintenance of industrial sites are often carried out by specialised operators who need to enter narrow and potentially dangerous environments. In this context, cable-driven hyper-redundant robots support the operators to carry out inspection and maintenance tasks proving to be an effective solution in terms of safety. The cable transmission keeps the actuators safe from the possible extreme environmental conditions of the inspection site, and the kinematic redundancy allows the robot to move into narrow environments avoiding obstacles. This dissertation aims to study cable-driven hyper-redundant robots providing a unified modelling framework that accurately describes their dynamics and could be employed to design control algorithms. The proposed modelling technique defines a simulation environment by interconnecting all the components of a mechatronic system. This approach allows speeding up the preliminary analysis necessary to evaluate the effectiveness of different solutions highlighting possible critical aspects. Furthermore, describing each subsystem by different complexity models allows employing the optimal model for the various scenarios the designer would analyse, such as secondary dynamics studies or control algorithm design. The obtained model provides the framework to design a control algorithm able to damp the residual vibration induced by cable transmission. Since fast actuators need to be employed to increase the vibrations damping, a novel design methodology to passively compensate for gravity forces is presented to improve the actuators dynamic response. Finally, the proposed modelling framework is applied to a novel cable-driven hyper-redundant robot to prove the versatility of this method.

TABLE OF CONTENTS

LIST OF FIGURES

LIST OF TABLES

CHAPTER 1

INTRODUCTION

The technological advancement achieved by the robotic industry over the past 50 years has determined that robots spread to a wide variety of applications. One of the leading economic and social stimuli to develop new robotic systems concerns safety. Examples that are there for all to see concern the monitoring of infrastructures for accidents prevention or the possibility of acting in emergencies, such as first aid in places destroyed by natural disasters, without endangering rescuers' life. These are examples that stir up public opinion, however, there is a category of workers who daily have to perform tasks in hazardous environments that could seriously compromise their health.

One of the fields in which workers are subject to high risk is the inspection and maintenance of industrial sites such as nuclear power plants, nuclear waste sites, vessels, tanks and pipelines. Nowadays, most of these operations are carried out by specialised operators who need to enter narrow and potentially dangerous environments, often placed in remote areas that are difficult to reach. As infrastructures age, the risk of failure increases, especially for those facilities that continue to operate beyond their expected life cycle. In this context, employing robotic systems that support the operators in carrying out the inspection and maintenance tasks can be an effective solution to minimise risks.

1.1 MOTIVATION

Introducing inspection and maintenance robots into existing plants requires developing highly customised solutions. These solutions can hardly be reused in different scenarios. Consequently, development and production costs increase, slowing down the spread of such devices. Some attempts to solve this problem have been carried out by European projects such as PETROBOT [1] and ROBINS [2]. The first focused on developing inspection devices in the oil and gas industry, the second in the naval field. According to stakeholders' opinion, SPARC defined that workers' safety and reduction of plant downtime due to inspection and maintenance operation are priority objectives [3] in industries.

In the last years, several devices were developed to accomplish inspection and maintenance tasks in different fields. Crawlers and wheeled robots have been used for the inspection of power generation plants [4]. Several companies have produced drones that could be used to monitor the conditions of infrastructures and industrial plants [5]. Long-reach manipulators with the ability to move in narrow spaces have been developed to inspects harsh and hazardous environments [6].

This work focuses on studying a subset of long-reach manipulators called cable-driven hyper-redundant robots. The cable actuation allows moving the actuators from joints to chassis reducing the overall weight of the moving structure and increasing the payload capability of the robot. Furthermore, cable-driven mechanisms keep the actuators safe from possible extreme environmental conditions of the inspection site and the hyper-redundancy allows the robot to move into constrained environments. However, cables introduce non-linear elastic phenomena that can reduce the precision and accuracy of motion, stability of the control system and damping of residual vibrations. In this context, defining an accurate model becomes fundamental to simulate the system behaviour and tune parameters of the control algorithm.

This dissertation aims at advancing the state of the art by proposing a unified modelling framework for cable-driven hyper-redundant manipulators. This framework defines both complex models to accurately simulate the system be-

haviour, intending to perform analyses for the system design, or simplified models suitable for the controller design.

1.2 Ansaldo Energia's Case of Study

Ansaldo Energia is one of the world's leaders in the power generation industry. Its core businesses consist of both manufacturing turbines and generators and providing maintenance services to power plant owners. The company has collaborated since 2018 with the Advanced Robotic Department of the Italian Institute of Technology, intending to develop a robotic system to inspect the combustion chambers of their gas turbines. Up to now, this type of inspection has been performed by a specialised operator who needed to reach the power plant, which may be settled everywhere in the world, wait for the temperature inside the chamber to drop at 40°C, enter the chamber, and check if the tiles of the cover were damaged. Considering that the thermal gradient decreases as the temperature decreases, the operator may inspect the plant even one week after the alarm warning. Furthermore, the system has often no problem.

The project's mission is to develop a robotic system that can enter the combustion chamber when the temperature is about 100°C, autonomously or teleoperated. In this way, it is possible to reduce the operator's risks, the time required to accomplish the inspection, and the plant downtime.

In this context, cable-driven hyper-redundant robots may be an effective solution, even if they introduce some challenges to overcome. In the following sections a preliminary prototype of a cable-driven hyper-redundant robot is presented as a possible solution for the Ansaldo Energia case of study. A simplified scenario where a hypothetical trajectory to enter and explore a combustion chamber moving through a manhole aperture is presented as an exemplary task to highlights the effects of the cable transmission during the execution of the operation.

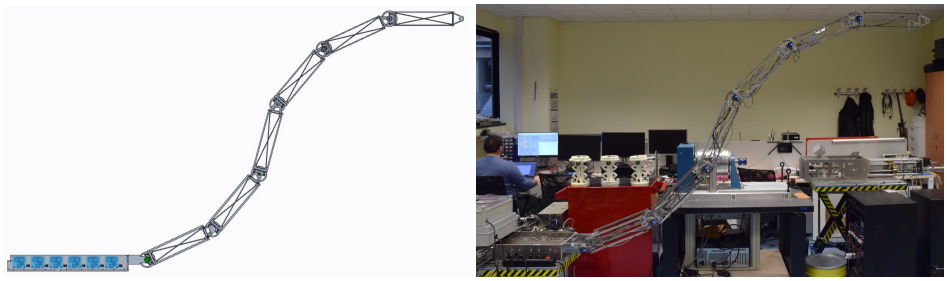

(a) CAD model. (b) Preliminary prototype.

Figure 1.1 Preliminary prototype of a cable-driven hyper-redundant robot developed for the Ansaldo Energia project.

1.2.1 Planar Robot Preliminary Prototype

The preliminary prototype of a cable-driven hyper-redundant robot, shown in Fig. 1.1, is composed of six parallel revolute joints which allow moving the end-effector in a specific Cartesian position on a plane. A dedicated device, such as a 3-axis gimbal system, can be added to the end-effector to reach any attitude in the Cartesian space. So, for the task of positioning the end-effector in a bi-dimensional Cartesian space, this robot has four degrees of redundancy. Each joint is driven by a pair of cables attached to a circular pulley fixed to a link with a length of 500 mm. The cables are routed along the structure of the robot through rollers that constrain them to pass along the neutral axis of each link. This routing criterion allows generating a map between the actuator and joint velocity that is constant and decoupled. So the corresponding Jacobian, J_l, is a diagonal and constant matrix whose elements are equal to the radius of the driving pulleys. Table 1.1 lists the DH parameters [7] describing the kinematics of the robot.

The description of all the components of this prototype are detailed in appendix A. This first design is a proof of concept for the capabilities of cable-driven hyper-redundant robots to address inspection tasks, and it can be employed as test-bench for the proposed control algorithm.

Joint	a_i [mm]	α_i [rad]	d_i [mm]	θ_i [rad]
1	0	$\pi/2$	0	q_{r_1}
2	500	0	0	q_{r_2}
⋮	⋮	⋮	⋮	⋮
6	500	0	0	q_{r_6}
End-effector	500	0	0	0

Table 1.1 DH parameters for the planar robot preliminary prototype

1.2.2 Exemplary Task

Let consider the scenario depicted in Fig. 1.2. The task assigned to the robot consists of performing a visual inspection of point F passing through the checkpoints A, B, C, D, and E by avoiding colliding with the obstacles O_1, O_2, the ground, and the ceiling. The trajectory of the robot, identified by the blue line, is generated interpolating all the checkpoints through a third-order spline.

The inspection of such a constrained environment needs a change of paradigm for the inverse kinematic problem. The obstacles and joints limit avoidance gain priority on the end-effector trajectory tracking to prevent the robot damages itself or the environment to inspect. In this context, a null-space approach to inverse kinematic is proposed. It is based on the results presented in [8, 9], setting as primary task joint limits satisfaction, as secondary task obstacles avoidance, and as tertiary task following the desired trajectory. The general formulation for a null-space inverse differential kinematic problem is written as

$$\dot{\boldsymbol{q}} = J_1^{\dagger}\boldsymbol{v_1} + \left(I - J_1^{\dagger}J_1\right)J_2^{\dagger}\boldsymbol{v_2} + \left(I - J_1^{\dagger}J_1\right)\left(I - J_2^{\dagger}J_2\right)J_3^{\dagger}\boldsymbol{v_3}, \tag{1.1}$$

where $\dot{\boldsymbol{q}}$ is the joint velocity, $\boldsymbol{v_i}$ are the desired velocity associated to each task and J_i are the Jacobian mapping the joint velocity into the i^{th} task velocity.

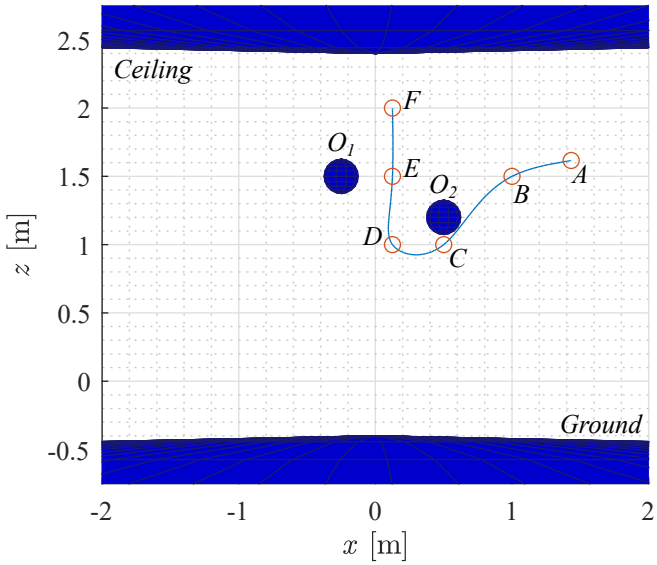

Figure 1.2 Exemplary scenario for an inspection task.

The joints limit avoidance is performed defining $J_1^\dagger$ as a diagonal activation matrix H such that

$$h_{i,i} = \begin{cases} 1 & \text{if} \quad |q_i| \geq q_{i_{max}} \\ 0 & \text{otherwise,} \end{cases} \tag{1.2}$$

and the element of $\boldsymbol{v_1}$ as

$$v_{1_i} = \begin{cases} \dot{q}_{l_i} & \text{if} \quad q_i < -q_{i_{max}} \\ -\dot{q}_{l_i} & \text{else if} \quad q_i > q_{i_{max}} \\ 0 & \text{otherwise,} \end{cases} \tag{1.3}$$

where $q_{i_{max}}$ defines the maximum joint angle, and $\dot{q}_{l_i}$ is the desired velocity which allows the joints to move into their range of motion. The obstacle avoidance task requires first to define the obstacle geometry and properties. Let assume that each obstacle is modelled as a sphere with centre $\boldsymbol{p_c}$ and radius r_o. Two types of obstacles are implemented in this application: attractive and repulsive. Attractive obstacles allow the robot to move inside the sphere pulling it to the centre if the distance between the robot and the surface of the sphere becomes

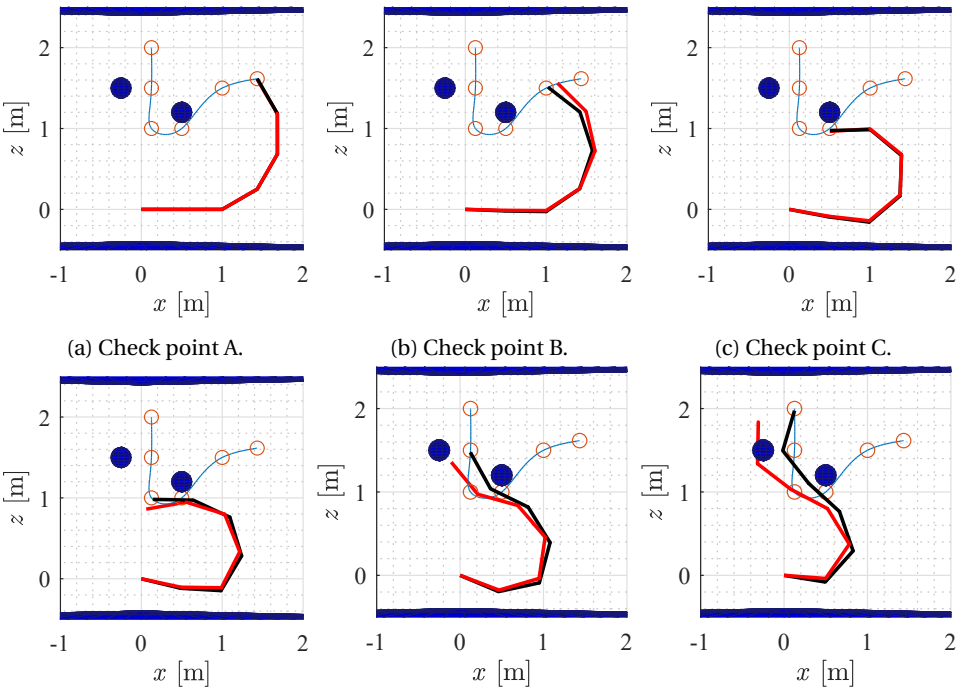

(a) Check point A. (b) Check point B. (c) Check point C.

(d) Check point D. (e) Check point E. (f) Check point F.

Figure 1.3 Effects of elasticity performing an inspection task. The piecewise black line identifies the desired configuration of the robot. The piecewise red line identifies the configuration of the physical robot affected by cable deformation.

too small. The opposite happens for repulsive obstacles. They allow the robot to move outside the sphere pushing it away from the centre if the distance between the robot and the surface of the sphere becomes critical. Introducing $\boldsymbol{p_o}$ as the point of the robot at the minimum distance from the obstacle, and

$$\boldsymbol{n_o} = \frac{\boldsymbol{p_o} - \boldsymbol{p_c}}{\left\| \boldsymbol{p_o} - \boldsymbol{p_c} \right\|}, \tag{1.4}$$

it is possible to define J_2 as the projection of the Jacobian matrix associated to $\boldsymbol{p_o}$ on $\boldsymbol{n_o}$. The vector $\boldsymbol{v_2}$ is set as the desired Cartesian velocity which allows the robot to move away from the obstacle. Finally, J_3 and $\boldsymbol{v_3}$ represent the Jacobian matrix and the desired velocity of the end-effector respectively.

The inverse kinematic algorithm provides the trajectory each actuator has to follow to reach all the check points avoiding the obstacles. Figure 1.3 shows both the desired and the real trajectory followed by the robot. It is evident that the flexibility introduced by cables degrades the ability of the robot to follow the desired end-effector trajectory with the risk of damaging both the robot and the environment to inspect.

1.3 OBJECTIVES

The main objective of this dissertation consists of providing a modelling framework to describe cable-driven hyper-redundant robots. This framework, based on the bond-graph theory, allows accurately simulating the behaviour of cable-driven hyper-redundant robots. The bond-graph approach highlights the transfer of power between components making evident the physical connection between each subsystem composing a cable-driven hyper-redundant robot. This framework allows defining several models of the same subsystem to achieve different objectives. For example, simplified models could be favourable to design a control system for a cable-driven robot. However, such models could neglect some secondary dynamics that the designer would observe in an accurate simulation.

The second objective consists of designing an appropriate controller to achieve the desired requirements concerning trajectory tracking, stability margin, and residual vibrations. The visco-elasto-plastic model of cables was exploited to design a cascade control algorithm based on the $\mathscr{H}_\infty$ theory. Such controller ensured robust stability of the inner loop. The vibration introduced by the elasticity of cable-driven transmissions needs fast actuators to be damped. This requirement goes against the need for high torque to overcome the pull of gravity. Consequently, a novel methodology for designing passive torque generators is presented to improve the dynamic response of the actuators.

Finally, preliminary analysis about the model of a novel cable-driven hyper-redundant robot is presented by including a novel model to describe the friction of cables sliding into bushings.

1.4 OUTLINES

This dissertation is structured in six chapters and three appendices. A brief summary of the topics covered in each chapter is reported below:

Chapter 2 A unified modelling framework based on the bond-graph approach is presented in this chapter to describe the dynamics of cable-driven hyper-redundant robots. First, a literature review about modelling techniques is discussed. Then, the bond-graph theory is shortly introduced and applied to define a unified modelling framework for cable-driven hyper-redundant robots.

Chapter 3 The problem of controlling cable-driven mechanism is discussed in this chapter to obtain good performances in terms of stability margin, trajectory tracking, and residual vibration damping. First, a literature review about the principal control architectures employed for flexible joints robot is presented. Consequently, a cascade control algorithm that considers the visco-elasto-plastic model of synthetic fibre cables has been proposed as a possible solution. The design of the inner force loop is based on the $\mathscr{H}_\infty$ control theory to achieve robustness to uncertainty and neglected dynamics. The outer loop consists of a PD controller with gravity compensation and is employed to control the joints motion. Its stability is analysed by exploiting the properties of port-Hamiltonian systems.

Chapter 4 The problem of relieving the actuators from generating high torques to overcome the pull of gravity acting on long-reach manipulators is discussed in this chapter. In this scenario, the study of mechanisms reducing static forces is crucial to increasing energy efficiency and the improving dynamic response of the system. In particular, the vibrations introduced by the elasticity of cable-driven transmissions need fast actuators to be damped. A novel methodology to design passive torque generators is presented to reduce the static load on long-reach manipulators and employing faster actuators able to deal with vibrations of cable-driven mechanisms.

Chapter 5 Preliminary analyses on a novel cable-driven hyper-redundant robot are presented in this chapter to validate the versatility of the proposed unified modelling framework. A novel model for the friction produced by cables sliding into bushings is presented and validated.

Chapter 6 This chapter presents the outcome of this dissertation and reports the possible future works.

Appendix A The description of the hardware employed in this work is detailed in this appendix.

Appendix B The details about the control law design for both the inner and outer loop are reported in this appendix.

Appendix C The software architecture employed to run the experiments and acquire the data is described in this appendix.

CHAPTER 2

MODELLING FRAMEWORK

Modelling arises from the need to study, predict and control the evolution of dynamic systems. The definition of simple but at the same time accurate models is crucial to design and control mechatronic devices. It allows suitably sizing each component of the system under development and, above all, analysing its behaviour in different operating conditions. Mechatronic systems are usually composed of elements belonging to different physical domains, such as the electrical, mechanical and hydraulic domain. In this context, a unified modelling framework plays a leading role in defining the dynamic equation of the entire system. Furthermore, considering cable-driven hyper-redundant robots, simplified models can be obtained exploiting their modular structure. In particular, it is possible to identify different modules that make up the system, model them individually, and finally define their interaction. In this work, the three main modules composing the system are: linear actuators, cables, and joints.

The modular structure and the ability to manage multi-physic systems perfectly fit with the bond-graph approach. The graphical nature of bond-graphs allows conceiving the essential properties of a system detecting all the critical subsystems and relevant information such as constrained states and algebraic loops. Thus, even before deriving the dynamic equations, the benefits and consequences of potential approximations or simplification became evident to the modeller. Furthermore, bond-graphs allow independently analysing the different

elements constituting a system, figuring out all the phenomena involved in each subsystem. Then, connecting each subsystem through power bonds, a model of the entire system can be derived. In this chapter, a literature review about modelling techniques is first presented, then the bond-graph theory is briefly introduced and applied to define a unified modelling framework for cable-driven hyper-redundant robots.

2.1 Literature Review

In recent years hyper-redundant robots have been employed in several applications ranging from endoscopic surgery to maintenance and inspection of industrial plants. The most applied classification splits hyper-redundant robots up continuum and rigid-backbone. The peculiarity of continuum robots is the deformable structure, which provides unprecedented freedom of motion and compliance with external forces. These characteristics led to employ continuum robots in medical fields as endoscopes [10] or tools for minimally invasive surgery [11]. Rigid-backbone robots, instead, are composed of rigid links that allow designing long-reach manipulators. Moreover, the cable actuation provides a high payload capacity making such robots ideal for maintenance and inspection in hazardous environments. The most significant examples of cable-driven hyper-redundant robots for inspection are the OC robotics snake arm, employed in nuclear sites [12] and aircraft wings [13], and the Super-Dragon developed to inspect the Fukushima nuclear power plant [14]. Cable-driven hyper-redundant robots are usually composed of an actuation box, cables and a mechanical structure. There is comprehensive literature about the dynamic modelling of each subsystem.

The Lagrange formulation is the basis of the first work about manipulator modelling [15, 16]. In [17], Hollerbach developed an efficient algorithm to derive Lagrange equations of a serial manipulator. Orin et al. in [18] presented a recursive Newton-Euler method to analyse the dynamics of spatial open-chain mechanisms. Using [18] as a baseline, researchers developed new algorithms trying to improve computational efficiency. The most relevant Newton-Euler

algorithms are the Composite Rigid Body Algorithm [19] and the Articulated Body Algorithm [20]. Featherstone et al. presented a comparison between recursive Newton-Euler algorithms [21]. Silver, in [22], demonstrated the equivalence of the Lagrange and Newton-Euler method.

The above works start from the assumption that manipulators are composed only of rigid bodies. However, to increase power efficiency and obtain safe human-machine interactions, real devices usually have compliant transmission and light-weight structure, making this assumption valid exclusively for slow motion and small interacting forces. Thus flexibility needs to be considered in the robot model to avoid the degradation of performances. Two families of flexible robots can be defined: robots with flexible links and robots with elastic joints.

Flexible link manipulator dynamic is described through partial differential equations. The state-space of a system described by partial differential equations has an infinite number of state variables. Thus, to numerically represent its behaviour, the dynamic model needs to be approximated as a system of ordinary differential equations. The most common approximation techniques are the assumed mode method and the finite element method. Book proposed a recursive Lagrangian formulation describing the link flexibility in terms of a summation of assumed mode [23]. De Luca et al. formulated a closed-form dynamic model of planar multi-link light-weight robots based on assumed modes and Lagrangian formulation [24]. A different approach, based on finite element analysis, was investigated in [25, 26]. A Newton-Euler method to model flexible link robots is shown in [27]. Bascetta et al. described an efficient recursive model for flexible link robots based on a mixed Eulerian-Lagrangian formulation [28].

Elastic joint manipulators have flexibility concentrated in the joints of the robot. One of the first studies which considered the joint elasticity in the dynamic model was [29]. Spong proposed a Lagrangian formulation which, under the assumption that the reduction ratio is high, allows simplifying the dynamic model of elastic joint manipulators [30]. Buondonno et al. proposed an efficient generalised Newton-Euler algorithm to compute the inverse dynamics of elastic joint manipulators [31].

In particular applications, both joint and link flexibility need to be considered in the dynamic model. Vakil et al. presented a closed-form solution based on assumed modes and Lagrange's equation to formulate dynamic equations of a planar robot with flexible links and flexible joints [32].

Cable-driven manipulators are a particular example of elastic joint robots. One of the most attractive characteristics of cable-driven mechanisms consists of moving actuators from joints to the chassis. This actuation strategy reduces the weight of the structure, consequently increasing the payload capability of the robot. Recently, to develop cable-driven mechanisms, researchers focus on studying the behaviour of synthetic fibre cables. Horigome et al. investigated the physical properties of synthetic fibres, such as Dyneema and Zylon PBO, to compare their characteristics with stainless wires [33]. The weight of the robot can be reduced by replacing stainless steel cables with synthetic fibre. Beside, synthetic fibres have a higher tensile strength and can wrap around pulleys with a smaller diameter than steel cables making the mechanical components extremely compact. Horigome et al. investigated the performances of different synthetic fibre in repetitive bending experiments [34]. Different models of cables were presented over the years. Fichera et al. presented a framework to create a general piece-wise elastic torque model for cable-driven robots identifying its parameters through standard procedures [35]. Choi et al. presented an integrated elasto-plastic model which describes the cables principal characteristics: creep, hysteresis and recovery [36]. Takata et al. proved that synthetic fibre cables could be modelled through Flory's model and that such model could be brought back to a conventional four-element model if a sufficient preload was applied [37].

The need for defining a unified modelling framework led to consider the bond-graph approach as a solution. The early studies about the bond-graph technique date back to 1959 [38, 39], showing the representation of power interaction between single components. The theoretical basis, definitions, and structures of this method are explained in [40–42].

The abstraction of the bond-graph approach from physical domains allows employing this modelling technique on a large variety of applications, such as biological systems [43, 44], economic and social dynamics [45, 46], the definition

of fault indicators on electro-mechanical devices [47], robotics [48, 49], and many others. Rosenberg in [50] developed a systematic procedure to derive linear state equations from bond-graphs. This procedure was extended to non-linear-systems by Martens in [51]. The causality assignment was investigated in [52, 53]. Birkett et al. presented the mathematical foundation of bond-graphs in [54–57], while Karnopp et al. provided a comprehensive review of the theory and application of bond-graphs in [58].

Modelling multibody dynamics and mechanical systems with non-linear geometry using bond-graph may introduce issue related to derivative causality. These mechanisms can be interpreted as particular IC-fields representing the subsystem as Lagrange's or Hamilton's equations [59]. This formulation hides the structure of the multibody system and information about constraint forces. To consider also these aspects, Karnopp proved that the bond-graph formulation is equivalent to Lagrange's equations of the first type introducing Lagrange multiplier and approximating the constraint forces through elastic and damping elements [60].

2.2 Bond-graph Theory

The bond-graph technique is a graphical approach mainly applied to model multi-physics systems. The bond-graph theory defines energy and power as fundamental dynamical variables and describes a physical system through the transfer of power between components. Since power and energy are quantities shared between all the physical domains, a unified representation based on power and energy variables can be derived. In the generalised notation, power variables are called effort, $e(t)$, and flow, $f(t)$, while energy variables are called momentum, $p(t)$, and displacement, $q(t)$. The relation between power and energy variables can be defined in differential form as

$$\frac{dp(t)}{dt} = e(t) \implies dp(t) = e(t)\,dt, \tag{2.1}$$

$$\frac{dq(t)}{dt} = f(t) \implies dq(t) = f(t)\,dt, \tag{2.2}$$

or in integral form as

$$p(t) = \int_{t_0}^{t} e(\tau)\, d\tau + p_0, \tag{2.3}$$

$$q(t) = \int_{t_0}^{t} f(\tau)\, d\tau + q_0. \tag{2.4}$$

where p_0 and q_0 are respectively the value of the momentum and displacement at $t = t_0$. Tables 2.1 and 2.2 show correspondences between the generalised notation and the physical variables in the main physical domains.

The connection between elements is always described by pairs of power variables and must satisfy the energy conservation principle. The causality of each power port, the place where elements or subsystems are interconnected, defines which between effort and flow signals is the input and the output. The causality of each port can be easily computed starting from simple rules [52, 53]. By exploiting the definition of power and energy variables, few basic elements are necessary to describe most of the systems in a large variety of physical domains.

Domain	Effort		Flow	
Mechanical translation	Force	[N]	Velocity	[m/s]
Mechanical rotation	Torque	[N·m]	Angular velocity	[rad/s]
Hydraulic	Pressure	[N/m^2]	Volume flow rate	[m^3/s]
Electrical	Voltage	[V]	Current	[A]

Table 2.1 Generalised power variables.

Domain	Momentum		Displacement	
Mechanical translation	Momentum	[N·s]	Position	[m]
Mechanical rotation	Angular momentum	[N·m·s]	Angular position	[rad]
Hydraulic	Pressure momentum	[N·/m^2]	Volume	[m^3]
Electrical	Flux linkage	[V]	Charge	[A]

Table 2.2 Generalised energy variables.

1-PORT

1-port elements are described by a single pair of power variables and, depending on the relation between flow and effort, can be classified as elements that dissipate power, store energy and supply power. According to this definition, a 1-port element can also represent complex subsystems. Here an overview of the basic 1-port elements is presented.

The elements characterised by a static function between effort and flow are called 1-port resistors or R-components. They usually dissipate power, so the energy entering the 1-port resistor is never given back to the system. The linear 1-port resistor is characterised by the following constitutive law

$$e(t) = Rf(t) \tag{2.5}$$

where R represents the value of the 1-port resistor. This relation can be employed to model classical elementary components such as electrical resistors and mechanical dampers. More complex components can be modelled using non-linear 1-port resistors. An example is static friction acting on a DC motor described by the following constitutive relation

$$e(t) = \mu_s \operatorname{sgn}\big(f(t)\big) + \mu_v f(t)\,. \tag{2.6}$$

Energy-storing 1-port elements are classified on the variables involved in the constitutive law. C-components or 1-port compliance, are characterised by a static relation between effort and displacement. I-components or 1-port inertia, are characterised by a static relation between flow and momentum. These devices can store energy without loss. As for R-components, Energy-storing 1-port elements can describe both linear and non-linear components. The linear 1-port compliance and inertia are characterised, respectively, by the following constitutive laws

$$e(t) = \frac{1}{C} q(t), \tag{2.7}$$

$$f(t) = \frac{1}{I} p(t), \tag{2.8}$$

where C and I represent, respectively, the value of the 1-port compliance and inertia. These relation can be employed to model classical elementary components. For example, C-components can model electrical capacitors and mechanical springs while I-components can describe electrical inductance and mass or inertia in mechanical systems. The energy stored in both 1-port compliance and inertia is defined as

$$E(t) = \int_{t_0}^{t} e(\tau) f(\tau)\, d\tau + E_0. \tag{2.9}$$

Where E_0 represents the energy stored at $t = t_0$. Using (2.7) and (2.2) in (2.9), the energy stored in the C-component can be written in function of the displacement as

$$E(q) = \int_{q_0}^{q} e(q)\, dq + E_0. \tag{2.10}$$

Instead using (2.8) and (2.1) in (2.9), the energy stored in the I-component can be written in function of the momentum as

$$E(p) = \int_{p_0}^{p} f(p)\, dp + E_0. \tag{2.11}$$

From (2.10) (2.11) the demonstration that 1-port compliance and inertia are conservative systems is trivial. A graphical tool which help visualise the relation

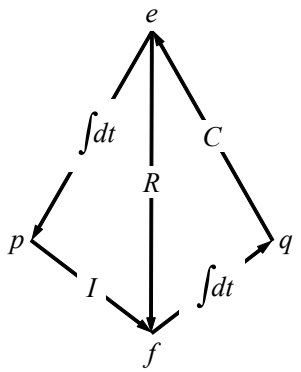

Figure 2.1 The three linear 1-port placed on the tetrahedron of states according to relation defined by constitutive laws.

between energy and power variables is the tetrahedron of state depicted in Fig. 2.1.

Power supplying 1-port elements are defined as effort source and flow source. Effort sources impose an effort independently on the flow acting on the port. Vice-versa flow sources impose a flow independently on the effort acting on the port. Some examples of effort sources are voltage generator for electrical systems and gravity force for mechanical systems. Typically these components provide power to the systems.

2-PORTS

2-ports elements are described by two pairs of power variables and the power flowing from one port to the other is conserved. This means that the following relation must always be satisfied

$$e_1(t) f_1(t) = e_2(t) f_2(t). \tag{2.12}$$

There are two basic components which satisfy (2.12). The first is called transformer and is described by the following constitutive law

$$\begin{cases} e_1(t) = m e_2(t) \\ f_2(t) = m f_1(t), \end{cases} \tag{2.13}$$

where m is the transformer modulus. Transformers are usually employed to model electrical transformers or gearbox in mechanical systems. The second is called gyrator and is described by the following constitutive law

$$\begin{cases} e_1(t) = r f_2(t) \\ e_2(t) = r f_1(t), \end{cases} \tag{2.14}$$

where r is the gyrator modulus. Gyrators are usually employed to model electromechanical transducer such as voice coil or accelerometers.

A generalisation of transformers and gyrators consists in considering m and r not constant. The obtained components are called modulated transformers and modulated gyrators. In modulated 2-ports the value of m and r usually depends on energy variables.

3-PORTS

3-ports elements, also called junctions, are described by three pairs of power variables. These components allow assembling the single elements into the entire system model. Most of the connection can be defined through two different junctions. The first is called common effort junction or 0-junction, and is defined such that all the efforts on the three ports are the same and, as for transformers and gyrators, the power is neither dissipated or stored. The constitutive law is defined as follows:

$$\begin{cases} e_1(t) = e_2(t) = e_3(t) \\ f_1(t) + f_2(t) + f_3(t) = 0 \end{cases} \tag{2.15}$$

The second is called common flow junction or 1-junction, and is defined such that all the flows on the three ports are the same and, as for transformers

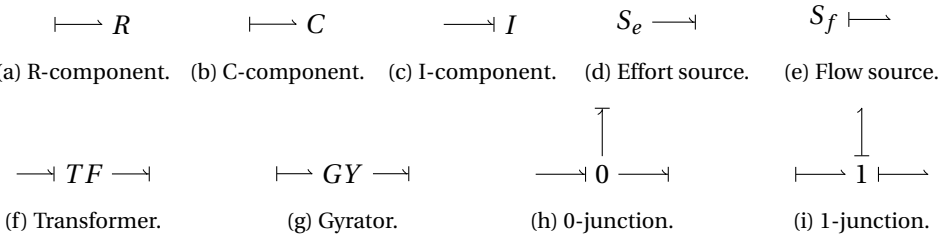

(a) R-component. (b) C-component. (c) I-component. (d) Effort source. (e) Flow source.

(f) Transformer. (g) Gyrator. (h) 0-junction. (i) 1-junction.

Figure 2.2 Symbols of the basic bond-graph elements with preferred causality.

and gyrators, the power is neither dissipated or stored. The constitutive law is defined as follows:

$$\begin{cases} f_1(t) = f_2(t) = f_3(t) \\ e_1(t) + e_2(t) + e_3(t) = 0 \end{cases} \tag{2.16}$$

Once the basic components have been defined, systems in a large variety of domain can be represented. Figure 2.2 summarises the symbols corresponding to the basic elements.

2.3 ACTUATOR MODEL

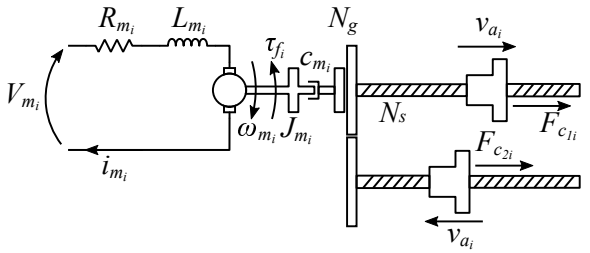

Figure 2.3 Schematic of the i^{th} linear actuator employed in this work.

In this work, several prototypes of linear actuators, developed according to the project progress, were designed to produce the forces transmitted to the cables. This section presents a general model to describe all the actuators variants by updating the appropriate parameters.

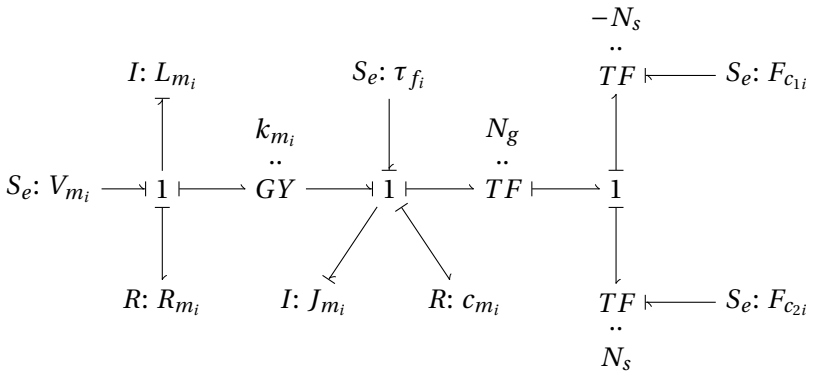

Figure 2.4 Bond graph describing the linear actuator model.

The i^{th} actuation system, represented in Fig. 2.3, is composed of a geared DC motor with winding resistance R_{m_i}, winding inductance L_{m_i}, torque constant k_{m_i}, rotary damping c_{m_i}, load inertia J_{m_i}, and a gear ratio N_g. The motor drives a pair of screw nut mechanisms with screw ratio N_s at the same speed but in the opposite direction. V_{m_i} is the command voltage, i_{m_i} the motor current, $F_{c_{1i}}$ and $F_{c_{2i}}$ are the loads applied by the cable pair, and τ_{f_i} represents the friction torque.

The bond-graph describing this system is depicted in Fig. 2.4. A peculiarity of this bond-graph concerns the modelling of friction. The element that most characterises the different versions of the actuation systems is friction. Considering friction as a source of effort allows making the actuator model generic. It appears as a load torque to model independently for each actuator version. Furthermore, this representation allows excluding the effect of friction phenomena which, being non-linear and discontinuous, often slow down the simulation.

Finally, following the bond-graph theory, the state-space representation of the actuator dynamic is computed as

$$\begin{cases} \dot{p}_{a_{ei}} = -\dfrac{R_{m_i}}{L_{m_i}} p_{a_{ei}} - \dfrac{k_{m_i}}{J_{m_i}} p_{a_{mi}} + V_{m_i} \\ \dot{p}_{a_{mi}} = \dfrac{k_{m_i}}{L_{m_i}} p_{a_{ei}} - \dfrac{c_{m_i}}{J_{m_i}} p_{a_{mi}} + \tau_{f_i} + N_t \Delta F_{c_i} \\ v_{a_i} = -N_t \dfrac{p_{a_{mi}}}{J_{m_i}}, \end{cases} \tag{2.17}$$

where $p_{a_{ei}}$ and $p_{a_{mi}}$ are the state variable representing the flux linkage and the angular momentum of the motor respectively, v_{a_i} is the output variable representing the actuator linear velocity, $\Delta F_{c_i} = F_{c_{1i}} - F_{c_{2i}}$ is the difference of the cable forces, and $N_t = N_g N_s$ is the total reduction ratio.

2.4 Screw Nut Friction Model

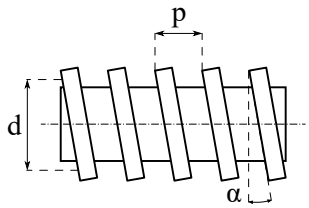

(a) Geometric parameters of a screw nut mechanism

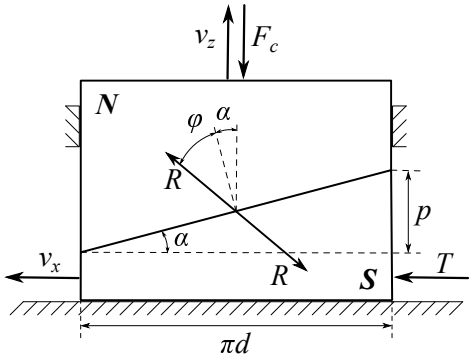

(b) Forces acting on a screw nut mechanism

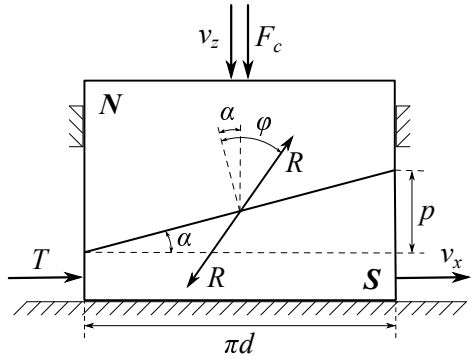

(c) Forces acting on a screw nut mechanism

Figure 2.5 Screw-nut friction model.

Screw nut mechanisms allow transforming rotational to linear motion. Their kinematics is relatively simple and allows reaching high reduction ratio $N_s = 2\pi p$, where p is the screw pitch. The main drawback of these mechanisms is the low efficiency which typically ranges from 20% to 80%. In this work, the selected screw-nut mechanism is not back-drivable, which means that the transmission efficiency is lower than 50%. Thus, dissipating more than 50% of the power due to friction, an accurate model is necessary to compensate for this phenomenon.

In a screw-nut mechanism with a rectangular thread, a mean diameter d and a helix angle α, most of the friction loss is due to the sliding contact between the screw and the nut [61]. If the thread is unrolled for a single turn, the screw can be represented by the body $\boldsymbol{S}$ in Fig. 2.5b and 2.5c, while the nut is the body $\boldsymbol{N}$. According to this representation, the angular velocity of the screw is equal to a linear velocity v_x along the horizontal axis of the body $\boldsymbol{S}$. This motion produces the vertical displacement of the nut with a velocity v_z along the vertical axis.

Let consider the case, represented in Fig. 2.5b, in which the cable applies a load F_c in the opposite direction of the nut motion. The nut applies a force R, computed as

$$R = \frac{F_c}{\cos\left(\varphi + \alpha\right)}, \tag{2.18}$$

to the screw, where φ represents the friction angle determined from the friction coefficient of the materials. Consequently, to produce the required motion, body $\boldsymbol{S}$ needs to apply a horizontal force equal to

$$T = F_c \tan\left(\varphi + \alpha\right). \tag{2.19}$$

As stated before, body $\boldsymbol{S}$ is the unrolling of the screw on a plane. Thus T represents the tangential force acting on the thread of the screw. Consequently, the torque to produce the required motion is computed as

$$\tau_s = \frac{d}{2} F_c \tan\left(\varphi + \alpha\right). \tag{2.20}$$

Let now consider the case, represented in Fig. 2.5c, in which the cable applies a load F_r in the same direction of the nut motion. Following the same procedure, the torque necessary to produce the required motion is computed as

$$\tau_s = \frac{d}{2} F_c \tan\left(\varphi - \alpha\right). \tag{2.21}$$

The linear actuator employed in this work is composed of two screw-nut mechanisms constrained to move at the same speed, but in opposite direction. So combining (2.20) and (2.21) and considering the total gear ratio, the friction

model for the i^{th} entire screw-nut mechanism is obtained as follows:

$$\tau_{f_i} = \begin{cases} -N_t \dfrac{d}{2}\left(F_{c_{1i}} \tan\left(\varphi+\alpha\right) + F_{c_{2i}} \tan\left(\varphi-\alpha\right)\right) & \omega_{m_i} > 0 \\ 0 & \omega_{m_i} = 0 \\ N_t \dfrac{d}{2}\left(F_{c_{1i}} \tan\left(\varphi-\alpha\right) + F_{c_{2i}} \tan\left(\varphi+\alpha\right)\right) & \omega_{m_i} < 0 \end{cases} \tag{2.22}$$

2.5 CABLE MODEL

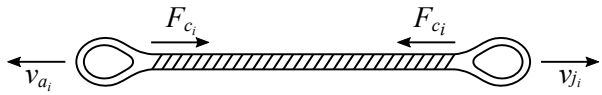

Figure 2.6 Schematic of the force and velocities acting on actuation cables.

In the system presented in this work, the motion transmission occurs through synthetic fibre cables, whose schematic is represented in Fig. 2.6. These materials present non-linear visco-elasto-plastic behaviour, so applying tension on the cable, elastic and plastic strain occurs. The choice of employing Flory's model, shown in Fig. 2.7a, allows separating the linear visco-elastic phenomena from the non-linear elasto-plastic phenomena.

The four elements model, represented in the left side of Fig. 2.7a, describes linear visco-elastic materials through a combination of elasticity, modelled by the spring K_1, viscosity, described by a damper c_2, and retarded elasticity, represented by the parallel of K_3 and c_3. The non-linear elasto-plastic behaviour is modelled by the parallel of the spring K_p and the ratchet R_p, represented in the right side of Fig. 2.7a. The ratchet element does not allow retrieving the plastic strain, while the spring retains the value of maximum tension previously applied. Thus, to further increase the plastic strain, it is necessary to apply a higher force than the maximum tension previously reached. This behaviour implies that if the maximum tension is applied on the cable, then the non-linear elasto-plastic effects can be neglected and Flory's model degenerates to the four elements model. The above mentioned parameters are normalised with respect to the

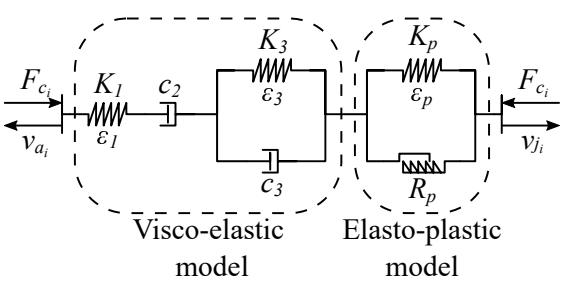

(a) Flory's model

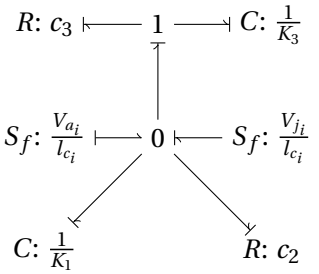

(b) Bond-graph representation of the four elements model.

Figure 2.7 Synthetic fibre cable dynamic model.

length of the cables. So if the velocity and forces acting on the cables are scaled by the cables length it is possible to describe all the cables by the same parameters.

Fig. 2.7b illustrates the equivalent bond-graph representation of the four elements model. As stated before, this bond-graph describes the behaviour of synthetic fibres only under the assumption that the maximum force was previously applied on the cable. Each actuator drives a pair of cables, thus the resulting state-space description for the i^{th} pair of cables is defined as

$$\begin{cases} \dot{q}_{c_{11_i}} = -K_1\left(\dfrac{c_2+c_3}{c_2c_3}\right)q_{c_{11_i}} + \dfrac{K_3}{c_3}q_{c_{21_i}} + \dfrac{v_{j_i}-v_{a_i}}{l_{c_i}} \\ \dot{q}_{c_{21_i}} = \dfrac{K_1}{c_3}q_{c_{11_i}} - \dfrac{K_3}{c_3}q_{c_{21_i}} \\ \dot{q}_{c_{12_i}} = -K_1\left(\dfrac{c_2+c_3}{c_2c_3}\right)q_{c_{12_i}} + \dfrac{K_3}{c_3}q_{c_{22_i}} - \dfrac{v_{j_i}-v_{a_i}}{l_{c_i}} \\ \dot{q}_{c_{22_i}} = \dfrac{K_1}{c_3}q_{c_{12_i}} - \dfrac{K_3}{c_3}q_{c_{22_i}} \\ \Delta F_{c_i} = K_1\left(q_{c_{11_i}} - q_{c_{12_i}}\right), \end{cases} \tag{2.23}$$

where $q_{c_{11_i}}$, $q_{c_{21_i}}$, $q_{c_{12_i}}$, and $q_{c_{22_i}}$ are the state variables representing the strain of the cables, ΔF_{c_i} is the output variable representing the net force applied by the cables, l_{c_i} is the length of the cable, and v_{j_i} and v_{a_i} are the linear velocity of the joint and actuator, respectively.

Let now define a new set of state variables as

$$\begin{bmatrix} \Delta q_{c_{1i}} \\ \Delta q_{c_{2i}} \end{bmatrix} = \begin{bmatrix} q_{c_{11}} - q_{c_{12}} \\ q_{c_{21}} - q_{c_{22}} \end{bmatrix}. \tag{2.24}$$

Then, using (2.24), the dynamic equation describing the pair cables can be written as

$$\begin{cases} \Delta \dot{q}_{c_{1i}} = -K_1 \left(\dfrac{c_2 + c_3}{c_2 c_3} \right) \Delta q_{c_{1_i}} + \dfrac{K_3}{c_3} \Delta q_{c_{2i}} + 2 \dfrac{v_{j_i} - v_{a_i}}{l_{c_i}} \\ \Delta \dot{q}_{c_{2i}} = \dfrac{K_1}{c_3} \Delta q_{c_{1i}} - \dfrac{K_3}{c_3} \Delta q_{c_{2i}} \\ \Delta F_{c_i} = K_1 \Delta q_{c_{1i}}, \end{cases} \tag{2.25}$$

2.6 MULTIBODY MODEL

Multibody dynamics is a branch of mechanics which studies the motion of connected bodies. The bond-graph representation of complex mechanical systems is hard to manage due to algebraic loops and derivative causality.

A possible solution to model complex mechanical systems is to exploit the parallel between the Lagrange formulation in Hamiltonian form and IC-fields. The Lagrangian of a scleronomic mechanical system is defined as

$$\mathscr{L} = \mathscr{T} - \mathscr{U}, \tag{2.26}$$

where $\mathscr{T}$ and $\mathscr{U}$ represent the total kinetic co-energy and potential energy respectively. The dynamic equations can be derived from the Lagrangian as

$$\frac{d}{dt} \frac{\partial \mathscr{L}}{\partial \dot{\boldsymbol{q}}} - \frac{\partial \mathscr{L}}{\partial \boldsymbol{q}} = \frac{d}{dt} \frac{\partial \mathscr{T}}{\partial \dot{\boldsymbol{q}}} - \frac{\partial \mathscr{T}}{\partial \boldsymbol{q}} + \frac{\partial \mathscr{U}}{\partial \boldsymbol{q}} = \boldsymbol{\xi}, \tag{2.27}$$

where $\boldsymbol{q}$ and $\dot{\boldsymbol{q}}$ represent the generalised coordinates and $\boldsymbol{\xi}$ are the generalised forces. Defining

$$\boldsymbol{p} = M(\boldsymbol{q})\,\dot{\boldsymbol{q}} = \frac{\partial \mathscr{T}}{\partial \dot{\boldsymbol{q}}}, \tag{2.28}$$

$$\boldsymbol{g}(\boldsymbol{q}) = \frac{\partial \mathscr{U}}{\partial \boldsymbol{q}}, \tag{2.29}$$

where $\boldsymbol{p}$ represents the generalised momentum, $M(\boldsymbol{q})$ is the inertia matrix, and $\boldsymbol{g}(\boldsymbol{q})$ represents the torque generated by gravity, the dynamic equations (2.27) can be written in Hamiltonian form as

$$\begin{cases} \dot{\boldsymbol{q}} = M^{-1}(\boldsymbol{q})\,\boldsymbol{p} \\ \dot{\boldsymbol{p}} = \boldsymbol{\xi} - \boldsymbol{g}(\boldsymbol{q}) - \dfrac{\partial \mathscr{T}}{\partial \boldsymbol{q}}, \end{cases} \tag{2.30}$$

where $\boldsymbol{\xi}$ is the vector of generalised forces. Consider a skew-symmetric matrix $C(\boldsymbol{q}, \dot{\boldsymbol{q}})$ whose elements are defined as

$$c_{ij} = \frac{1}{2}\sum_{k=1}^{n} \dot{q}_k \left(\frac{\partial m_{ik}}{\partial q_j} - \frac{\partial m_{jk}}{\partial q_i} \right), \tag{2.31}$$

where n is the number of generalised coordinates $\boldsymbol{q}$ and m_{ij} are the elements of $M(\boldsymbol{q})$. Then the following equality holds:

$$C(\boldsymbol{q}, \dot{\boldsymbol{q}})\,\dot{\boldsymbol{q}} = \frac{1}{2}\dot{M}(\boldsymbol{q})\,\dot{\boldsymbol{q}} + \frac{\partial \mathscr{T}}{\partial \boldsymbol{q}} \tag{2.32}$$

Finally substituting (2.32) in (2.30) and exploiting the definition of generalised momentum the dynamic equations describing a multi-body system can be written in compact form as follows:

$$\begin{cases} \dot{\boldsymbol{q}} = M^{-1}(\boldsymbol{q})\,\boldsymbol{p} \\ \dot{\boldsymbol{p}} = \left(\dfrac{1}{2}\dot{M}(\boldsymbol{q}) - C(\boldsymbol{q}, \boldsymbol{p}) \right) M^{-1}(\boldsymbol{q})\,\boldsymbol{p} - \boldsymbol{g}(\boldsymbol{q}) + \boldsymbol{\xi}, \end{cases} \tag{2.33}$$

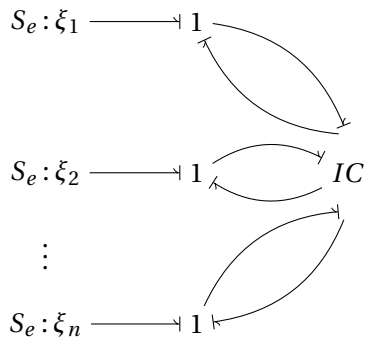

Figure 2.8 IC-field representation of the Hamiltonian form describing mechanical systems.

This representation is a particular case of the equations describing IC-fields. Thus complex mechanical systems can be represented by the bond-graph depicted in Fig. 2.8.

Let now consider a cable-driven hyper-redundant robot described by the generalised coordinates $\boldsymbol{q_r}$ and $\boldsymbol{p_r}$. The generalised forces are computed as

$$\boldsymbol{\xi_r} = J_l^T\left(\boldsymbol{q_r}\right)\Delta\boldsymbol{F_c}, \tag{2.34}$$

where $J_l\left(\boldsymbol{q_r}\right)$ is the full rank Jacobian matrix which maps the linear velocities of cables anchor points into angular joint velocities, and $\Delta\boldsymbol{F_c}$ are the differences between the cable forces acting on each joint. Furthermore substituting (2.34) in (2.33) the state-space representation of the system can be derived as

$$\begin{cases} \dot{\boldsymbol{q}}_{\boldsymbol{r}} = M^{-1}\left(\boldsymbol{q_r}\right)\boldsymbol{p_r} \\ \dot{\boldsymbol{p}}_{\boldsymbol{r}} = \left(\frac{1}{2}\dot{M}\left(\boldsymbol{q_r}\right) - C\left(\boldsymbol{q_r},\boldsymbol{p_r}\right)\right)M^{-1}\left(\boldsymbol{q_r}\right)\boldsymbol{p_r} - \boldsymbol{g}\left(\boldsymbol{q_r}\right) + J_l^T\left(\boldsymbol{q}\right)\Delta\boldsymbol{F_c} \\ \boldsymbol{v_j} = J_l\left(\boldsymbol{q_r}\right)M^{-1}\left(\boldsymbol{q_r}\right)\boldsymbol{p_r}, \end{cases} \tag{2.35}$$

2.7 Robot Model

In previous sections all the subsystems which describe a cable-driven hyper-redundant robot were analysed independently providing their equivalent bond-graph representation and dynamic equations. Let now consider a robot with n_j joints. For each joint of the robot it is necessary to have a linear actuator and a pair of cables. Considering the vectors $\boldsymbol{p_{a_e}}$, $\boldsymbol{p_{a_m}}$, $\boldsymbol{V_m}$, $\boldsymbol{\tau_f}$, and $\Delta\boldsymbol{F_c}$ defined as

$$\begin{aligned}
\boldsymbol{p_{a_e}} &= \left[p_{a_{e1}},\ldots,p_{a_{ei}},\ldots,p_{a_{en_j}}\right]^T \\
\boldsymbol{p_{a_m}} &= \left[p_{a_{m1}},\ldots,p_{a_{mi}},\ldots,p_{a_{mn_j}}\right]^T \\
\boldsymbol{V_m} &= \left[V_{m_1},\ldots,V_{m_i},\ldots,V_{m_{n_j}}\right]^T \\
\boldsymbol{\tau_f} &= \left[\tau_{f_1},\ldots,\tau_{f_i},\ldots,\tau_{f_{n_j}}\right]^T \\
\Delta\boldsymbol{F_c} &= \left[\Delta F_{c_1},\ldots,\Delta F_{c_i},\ldots,\Delta F_{c_{n_j}}\right]^T,
\end{aligned} \tag{2.36}$$

a compact representation of actuators dynamic equations is obtained formulating (2.17) in vector form as:

$$\begin{cases}
\dot{\boldsymbol{p}}_{\boldsymbol{a_e}} = -\hat{L}_m^{-1}\hat{R}_m\boldsymbol{p_{a_e}} - \hat{J}_m^{-1}\hat{k}_m\boldsymbol{p_{a_m}} + \boldsymbol{V_m} \\
\dot{\boldsymbol{p}}_{\boldsymbol{a_m}} = \hat{L}_m^{-1}\hat{k}_m\boldsymbol{p_{a_e}} - \hat{J}_m^{-1}\hat{c}_m\boldsymbol{p_{a_m}} + \boldsymbol{\tau_f} + N_t\Delta\boldsymbol{F_c} \\
\boldsymbol{v_a} = -N_t\hat{J}_m^{-1}\boldsymbol{p_{a_m}},
\end{cases} \tag{2.37}$$

where $\hat{L}_m$, $\hat{R}_m$, $\hat{J}_m$, $\hat{c}_m$, and $\hat{k}_m$ are diagonal matrices in which the elements on the diagonal are L_{m_i}, R_{m_i}, J_{m_i}, c_{m_i}, and k_{m_i} with $i = 1,\ldots,n_j$. Similarly, defining

$$\begin{aligned}
\Delta\boldsymbol{q_{c_1}} &= \left[\Delta q_{c_{11}},\ldots,\Delta q_{c_{1i}},\ldots,\Delta q_{c_{1n_j}}\right]^T \\
\Delta\boldsymbol{q_{c_2}} &= \left[\Delta q_{c_{21}},\ldots,\Delta q_{c_{2i}},\ldots,\Delta q_{c_{2n_j}}\right]^T
\end{aligned} \tag{2.38}$$

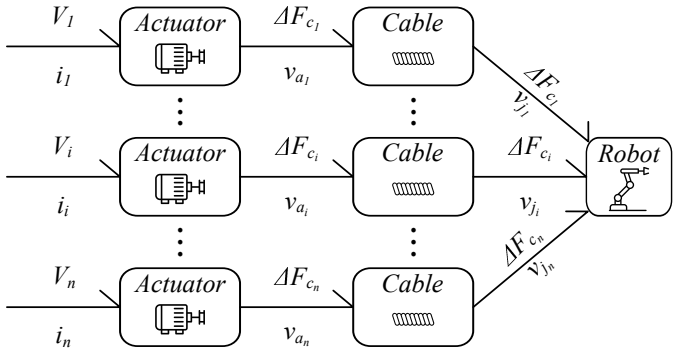

Figure 2.9 Bond graph describing the interaction between each subsystem composing a cable-driven hyper-redundant robot.

(2.25) can be formulated in vector form as

$$\begin{cases} \Delta\dot{\boldsymbol{q}}_{\boldsymbol{c_1}} = -K_1\left(\dfrac{c_2+c_3}{c_2c_3}\right)\Delta\boldsymbol{q}_{\boldsymbol{c_1}} + \dfrac{k_3}{c_3}\Delta\boldsymbol{q}_{\boldsymbol{c_2}} + 2\hat{L}_c^{-1}\left(\boldsymbol{v_j}-\boldsymbol{v_a}\right) \\ \Delta\dot{\boldsymbol{q}}_{\boldsymbol{c_2}} = \dfrac{K_1}{c_3}\Delta\boldsymbol{q}_{\boldsymbol{c_1}} - \dfrac{k_3}{c_3}\Delta\boldsymbol{q}_{\boldsymbol{c_2}} \\ \Delta\boldsymbol{F_c} = K_1\Delta\boldsymbol{q}_{\boldsymbol{c_1}}, \end{cases} \tag{2.39}$$

where $\hat{L}_c$ is a diagonal matrix in which the elements on the diagonal are l_{c_i}.

Connecting all the subsystem through power bond the model of the entire system is obtained. Figure 2.9 shows the equivalent bond-graph representation, from which it is possible to derive the dynamic equations of the entire system as

$$\begin{cases} \dot{\boldsymbol{p}}_{\boldsymbol{a_e}} = -\hat{L}_m^{-1}\hat{R}_m\boldsymbol{p}_{\boldsymbol{a_e}} - \hat{J}_m^{-1}\hat{k}_m\boldsymbol{p}_{\boldsymbol{a_m}} + \boldsymbol{V_m} \\ \dot{\boldsymbol{p}}_{\boldsymbol{a_m}} = \hat{L}_m^{-1}\hat{k}_m\boldsymbol{p}_{\boldsymbol{a_e}} - \hat{J}_m^{-1}\hat{c}_m\boldsymbol{p}_{\boldsymbol{a_m}} + \boldsymbol{\tau_f} + N_tK_1\Delta\boldsymbol{q}_{\boldsymbol{c_1}} \\ \Delta\dot{\boldsymbol{q}}_{\boldsymbol{c_1}} = -K_1\left(\dfrac{c_2+c_3}{c_2c_3}\right)\Delta\boldsymbol{q}_{\boldsymbol{c_1}} + \dfrac{k_3}{c_3}\Delta\boldsymbol{q}_{\boldsymbol{c_2}} + 2\hat{L}_c^{-1}\left(J_l\left(\boldsymbol{q_r}\right)M^{-1}\left(\boldsymbol{q_r}\right)\boldsymbol{p_r} - N_t\hat{J}_m^{-1}\boldsymbol{p}_{\boldsymbol{a_m}}\right) \\ \Delta\dot{\boldsymbol{q}}_{\boldsymbol{c_2}} = \dfrac{K_1}{c_3}\Delta\boldsymbol{q}_{\boldsymbol{c_1}} - \dfrac{k_3}{c_3}\Delta\boldsymbol{q}_{\boldsymbol{c_2}} \\ \dot{\boldsymbol{q}}_{\boldsymbol{r}} = M^{-1}\left(\boldsymbol{q_r}\right)\boldsymbol{p_r} \\ \dot{\boldsymbol{p}}_{\boldsymbol{r}} = \left(\dfrac{1}{2}\dot{M}\left(\boldsymbol{q_r}\right) - C\left(\boldsymbol{q_r},\boldsymbol{p_r}\right)\right)M^{-1}\left(\boldsymbol{q_r}\right)\boldsymbol{p_r} - \boldsymbol{g}\left(\boldsymbol{q_r}\right) + J_l^T\left(\boldsymbol{q_r}\right)K_1\Delta\boldsymbol{q}_{c_1}. \end{cases} \tag{2.40}$$

Equation (2.40) highlights that, starting from the dynamic equations of each subsystem obtained through the bond-graph formalism, it is possible to build the model of the entire system terms of Hamiltonian equations obtaining a unified modelling framework for cable-driven hyper-redundant robots.

CHAPTER 3

CONTROL ALGORITHM

Cable-driven mechanisms are intrinsically compliant. As for flexible joints robots, elasticity decreases performances concerning trajectory tracking, stability margin, and residual vibrations. Thus appropriate controller needs to be designed to achieve the desired requirements. In this work, a cascade control architecture is proposed. The inner loop is used to control the forces applied by cables. This controller is designed considering the visco-elasto-plastic model of synthetic fibre cables, presented in section 2.5, by exploiting the $\mathscr{H}_\infty$ control theory to achieve robust stability to parameters uncertainty and neglected dynamics. The outer loop, employed to control the joints motion, consists of a PD controller with gravity compensation. Its stability is analysed by exploiting the properties of port-Hamiltonian systems. In this chapter, the workflow to derive the control law is presented by showing the main results. All the details and parameters necessary to compute the specific control law for each joint are listed in appendix B.

3.1 LITERATURE REVIEW

Controlling flexible joints motion is a crucial topic in robotic research and was extensively treated in literature. Spong in [30] presented a global feedback linearisation of flexible joints robots which stabilises the system through static state feedback. The global feedback linearisation for flexible joints robots usually

needs an accurate model description. Furthermore, up to the third derivative of the joint position is necessary to perform full state feedback [62]. Tomei in [63] proposed a simple PD controller for robots with elastic joints demonstrating its robustness to uncertainty on the mass matrix parameters and friction model.

A different approach consists of considering flexible joints robots as port-hamiltonian systems [64]. This representation highlights the passivity properties of mechanical systems [65]. Passivity and other properties of port-Hamiltonian systems can be employed to verify the stability of a closed-loop dynamic system [66]. Albu-Schaffer et al. presented a unified passivity-based control framework for the position, torque, and impedance control of flexible joints robots [67].

A possible solution to simplify the control algorithm design is to exploit the stability properties of cascade controllers [68]. Tagliamonte et al. proposed a cascade controller in which the parameters were tuned through the passivity criterion [69]. A comparison between passivity-based and cascade controllers for flexible joints robots is presented in [70].

Even if cable-driven mechanisms are a subset of flexible joints, they present visco-elastic behaviour that is usually neglected in control design procedures. In this work, a cascade controller is presented in which the inner force loop is designed according to the $\mathscr{H}_\infty$ control theory starting from the visco-elastic model of synthetic fibre cables. The $\mathscr{H}_\infty$ theory is extensively applied in linear control problem because it allows robustly stabilising dynamic systems subject to model uncertainties and disturbances. A state-space formulation of the $\mathscr{H}_\infty$ control problem is presented in [71]. McFarlen et al. presented a design procedure that translates the loop shaping technique into a $\mathscr{H}_\infty$ control problem to obtain at the desired performances guaranteeing robust stability at all the frequencies [72]. A comprehensive review of this technique can be found in [73]. A non-linear variant of this technique is presented by Schaft in [74]. Different examples of $\mathscr{H}_\infty$ controller that robustly stabilises elastic joint robots can be found in the literature [75, 76]. The outer loop consists of a PD plus gravity compensation. Its stability is analysed by exploiting the properties of port-Hamiltonian systems.

3.2 CASCADE CONTROL ARCHITECTURE

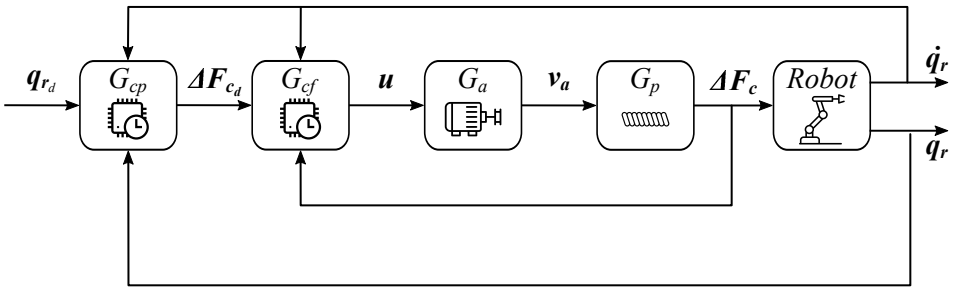

Figure 3.1 Cascade control architecture block diagram for a cable-driven hyper-redundant robot.

The model described by (2.40) allows simulating the behaviour of the entire system. Even if this model is accurate for simulation purposes, it reveals to be practically useless to design control algorithms without introducing simplification. Consider, for example, using global feedback linearisation [77] to control the motion of the previously described robotic arm. The global feedback linearisation consists of finding a suitable change of variables that transforms the non-linear system into a linear one. This transformation is obtained by differentiating the output to control until the input variable appears explicitly in the dynamic equation. Considering the system described by (2.40), it is necessary to derive the output variable five times to obtain an explicit dependency from the input variable. Thus the obtained linearised system is a series of five integrators, which can be stabilised through static full state feedback if the measure of up to the fourth time derivative of the joint position is available. Furthermore, the function which linearises the system contains up to the third derivative of the inertia matrix. Usually, both these quantities have to be computed numerically. This operation introduces noise and makes it hard to close the control loop in real-time.

A cascade control architecture reveals to be an effective solution to deal with this type of models. This approach allows splitting the control problem into two more manageable sub-problems. First, the inner loop, designed through

the $\mathscr{H}_\infty$ control theory, stabilises the dynamics of the actuators to control the forces applied by cables. Then, the outer loop, based on a PD controller with gravity compensation, stabilises the robot dynamics to control the joints motion. Figure 3.1 shows the block diagram representing the cascade control architecture applied on a cable-driven robot.

3.2.1 Inner Loop Controller Design

Mixed-Sensitivity $\mathscr{H}_\infty$ Synthesis

The mixed-sensitivity approach consists of shaping sensitivity and complementary sensitivity functions of closed-loop systems to achieve target performances and robustness. The idea is to translate time-domain requirements into frequency-domain specifications by choosing suitable frequency-dependent weighting functions such that

$$\begin{aligned} &\| W_S(s)\, S_n(s) \|_\infty < 1 \\ &\| W_T(s)\, T_n(s) \|_\infty < 1, \end{aligned} \tag{3.1}$$

where $S_n(s)$ and $T_n(s)$ are the sensitivity and complementary sensitivity functions associated to the nominal plant respectively, and $W_S(s)$ and $W_T(s)$ are their weighting functions.

This technique also allows for dealing with model uncertainties. Employing approximated models is often preferable to simplify controller synthesis. Consequently, to obtain robust control laws, the uncertainties associated with neglected dynamics, uncertain parameters estimation, or neglected non-linearities have to be considered. There are several methods to describe model uncertainty. In this work, unstructured multiplicative uncertainty is considered, thus the plant, $G_p(s)$, is modelled as an element of a set of systems described as

$$\mathscr{M}_m = \left\{ G_p(s) : G_p(s) = G_{p_n}(s)\left[1 + W_u(s)\,\Delta(s)\right], \|\Delta(s)\| \le 1 \right\}, \tag{3.2}$$

where $W_u(s)$ is the radius of uncertainty, and $G_{p_n}(s)$ is the nominal model. $W_u(s)$ describes at each frequency the uncertainty as a ball of radius $|W_u(s)\, L_n(s)|$,

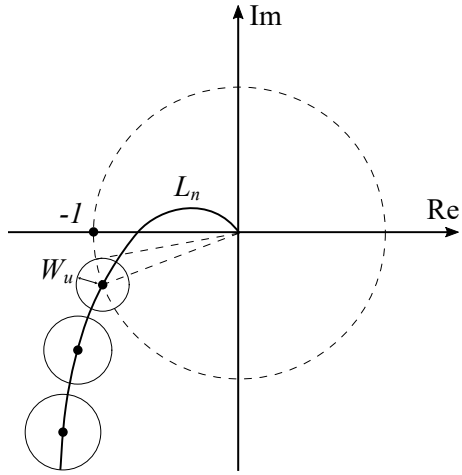

Figure 3.2 Nyquist plot for uncertain systems.

where $L_n(s)$ is the nominal loop function. Thus the real model can assume any possible value inside such ball affecting the stability margin of the system. A graphical interpretation of this phenomenon is given by the Nyquist plot depicted in Fig. 3.2 in which the effects of uncertainties on the phase margin are evident. By definition, a feedback system is robustly stable if and only if it is internally stable for each G_p belonging to the selected uncertain set. Using the Nyquist stability criterion, it is possible to demonstrate that a system $G_p \in \mathscr{M}_m$ is robustly stable if

$$\|W_u(s)\, T_n(s)\| < 1. \tag{3.3}$$

The mixed sensitivity $\mathscr{H}_\infty$ control allows finding the optimal controller, which minimises the $\mathscr{H}_\infty$ norm of performance and stability indicators. Let consider the general formulation of the feedback control problem shown in Fig. 3.3 in which $\mathcal{P}$ is the generalised plant, $\mathcal{K}$ is the controller, u are the control variables, w are exogenous inputs, and v and z are the measured and exogenous outputs respectively. The exogenous inputs and outputs are not necessarily physical variables of the control system. They have to be chosen to include the performance and stability requirements of the control problem considered. Defining $T_{wz}(s)$ as the closed-loop transfer matrix between w and z, the $\mathscr{H}_\infty$

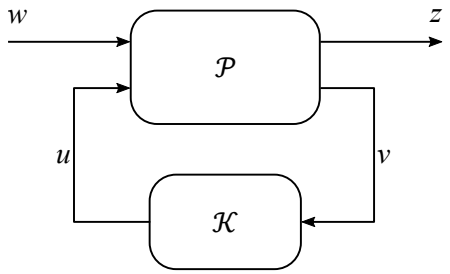

Figure 3.3 General configuration of a feedback control system.

optimal controller is computed as

$$\mathcal{K}^* = \arg\min_{\mathcal{K}\in\mathcal{K}_s} \|T_{wz}(s)\|_\infty, \tag{3.4}$$

where $\mathcal{K}_s$ is the class of all the controllers which provide internal stability of the feedback system. This optimisation problem can be written in a linear matrix inequalities form and solved using well known and robust convex optimisation algorithm.

Let now consider the problem of designing a controller G_c which robustly stabilises an uncertain system described by unstructured multiplicative uncertainty while at the same time allows satisfying nominal performances minimising the control effort. The exogenous outputs related to nominal performances and robust stability can be derived from (3.1) and (3.3). To bound the control effort an additional exogenous output which weights the control variable u is taken into account. Figure 3.4 shows the generalised plant required for this problem, where $W_1 = W_s$, $W_2 = W_s G_c$, and $W_3 = \max(|W_T|, |W_u|)$. Defined the generalised plant and using (3.4) the solution for this specific control problem is given by

$$G_c^* = \arg\min_{G_c\in\mathcal{K}_s} \left\| \begin{bmatrix} W_1 S_n \\ W_2 G_c S_n \\ W_3 T_n \end{bmatrix} \right\|_\infty. \tag{3.5}$$

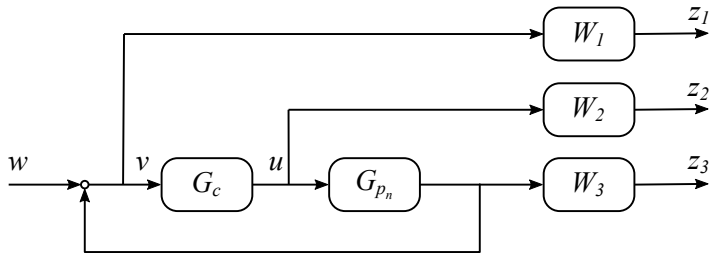

Figure 3.4 Generalised plant to design a controller G_c which robustly stabilises an uncertain system described by unstructured multiplicative uncertainty while at the same time allows satisfying nominal performances minimising the control effort.

LINEAR ACTUATOR CONTROLLER DESIGN

In this section the procedure for defining the control law for the inner force loop is presented considering just an actuator as an example. The procedure is the same also for the others actuators and a complete derivation of the control law is detailed in appendix B.

Let consider the feedback control system described by the block diagram depicted in Fig. 3.5. It represents a dynamic system composed of a linear actuator, described by the transfer function G_a, and a pair of cables, described by the transfer function G_p. The actuator is connected to a motor driver which allows controlling the actuator in torque mode.

The effects of coupling between cables and joints are modelled as disturbances. The joint velocity is modelled as a ramp disturbance, d_a, on the actuator, while the effects of elasticity are modelled as a low frequency sinusoidal disturbance, d_p, on the output signal.

The friction, modelled as a step signal d_f, enters the control problem as disturbance on the control variable. It is scaled by the coefficient $K_{f_{dc}}/K_{a_{dc}}$ where the numerator is the DC gain of the transfer function between friction signal and actuator velocity while the denominator is the DC gain of the transfer function between the torque command and the actuator velocity.

A high-frequency disturbance, d_s, is introduced in the feedback path to model the force sensor noise. The force sensors used to monitor the cable tensions are custom made and their parameters are listed in appendix A.2. The

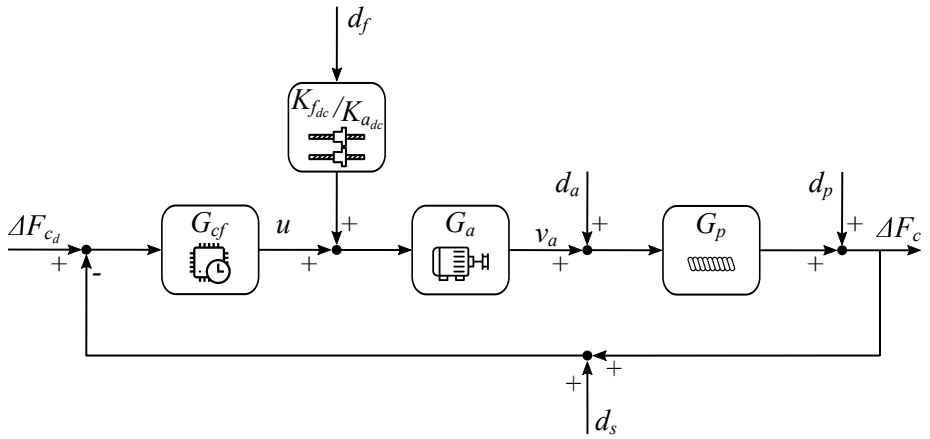

Figure 3.5 Inner force loop block diagram.

reference signal and disturbances assume the following form:

$$\begin{aligned}
\Delta F_{c_d} &= r_0\, t\varepsilon(t), \\
d_f &= d_{f_0}\varepsilon(t), \\
d_a &= d_{a_0}\, t\varepsilon(t), \\
d_p &= d_{p_0}\sin\left(\omega_p t\right), \\
d_s &= d_{s_0}\sin\left(\omega_s t\right),
\end{aligned} \tag{3.6}$$

where $\varepsilon(t)$ represents the step function. The other coefficients describing the signals are listed in appendix B.

The first step to find the optimal controller using the mixed-sensitivity $\mathscr{H}_\infty$ control theory consists of defining the uncertainty model and the nominal plant of the system to control. The cables transfer function, derived directly from (2.25), has the following structure:

$$G_p = K_{p_{dc}} \frac{1+\frac{s}{z_p}}{\left(1+\frac{s}{p_{p_1}}\right)\left(1+\frac{s}{p_{p_2}}\right)}. \tag{3.7}$$

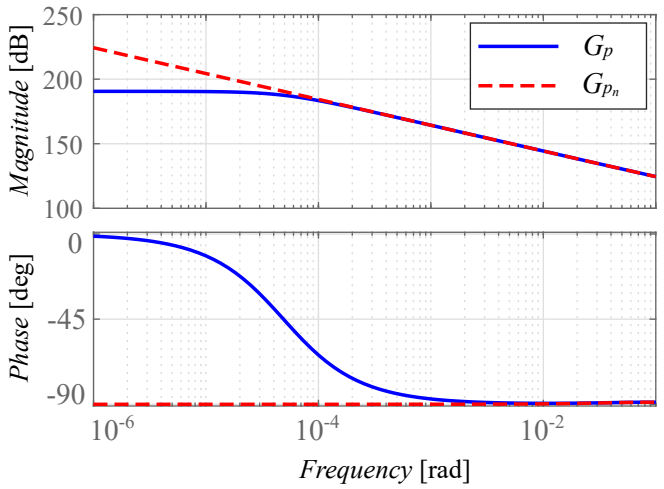

Figure 3.6 Bode diagram of the real, solid blue line, and approximated, dashed red line, cable model.

As described in appendix B, $p_{p_1} \approx 0$, then the nominal plant is approximated as

$$G_{p_n} = K_{p_n} \frac{1 + \frac{s}{z_p}}{s\left(1 + \frac{s}{p_p}\right)}. \tag{3.8}$$

Furthermore, since the model parameters K_1, c_2, K_3, and c_3 are estimated through an identification procedure, it is necessary to describe the system as an uncertain model set. The frequency domain comparison between the nominal and the real plant is presented in Fig. 3.6.

Considering the actuator dynamics, and the PI controller implemented on the motor driver, the transfer function between the torque command and the velocity of the actuator has the following form:

$$G_a = K_{a_{dc}} \frac{1 + \frac{s}{z_a}}{\left(1 + \frac{s}{p_{a1}}\right)\left(1 + \frac{s}{p_{a_2}}\right)\left(1 + \frac{s}{p_{a_3}}\right)}. \tag{3.9}$$

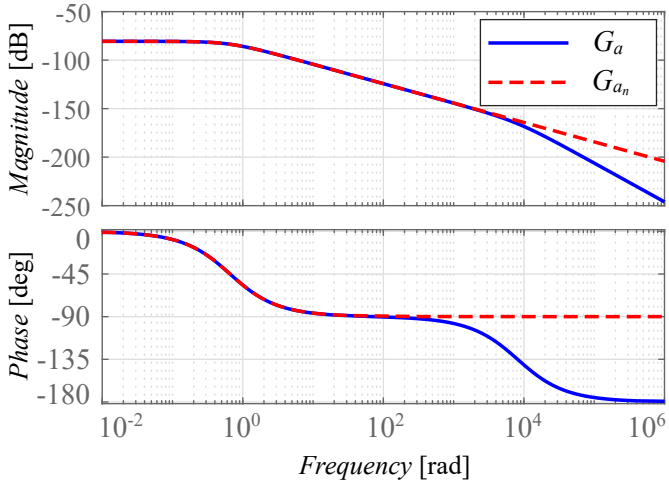

Figure 3.7 Bode diagram of the real, solid blue line, and approximated, dashed red line, actuator model.

Neglecting the high-frequency dynamics, the nominal transfer function for the actuator can be written as

$$G_{a_n} = \frac{K_{a_{dc}}}{\left(1 + \frac{s}{p_a}\right)}. \tag{3.10}$$

The frequency domain comparison between the nominal and the real actuator is presented in Fig.3.7

The neglected dynamics, and the uncertainty of the parameters can be modelled as unstructured multiplicative uncertainty. Defining the real and nominal system as

$$P(s) = G_p(s)\, G_a(s) \tag{3.11}$$

$$P_n(s) = G_{p_n}(s)\, G_{a_n}(s) \tag{3.12}$$

respectively, the radius of uncertainty can be computed exploiting the definition (3.2) as

$$W_u(s) = \max_{P(s)} \left| \frac{P(s) - P_n(s)}{P_n(s)} \right|. \tag{3.13}$$

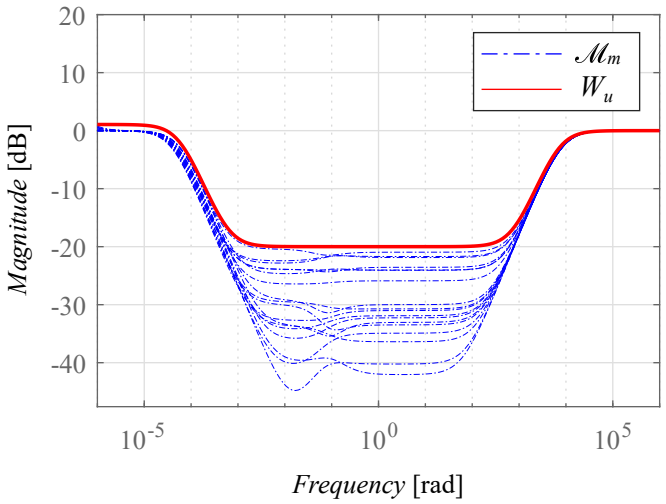

Figure 3.8 Bode diagram describing the model uncertainty and neglected dynamics. The dashed blue line represents the uncertainty model, the solid red line the corresponding weighting function.

Figure 3.8 shows the selected weighting function which gives an upper limit to the model uncertainty.

The second step concerns the translation of time-domain requirements in terms of the weighting functions W_1, W_2, and W_3 in the frequency domain. The steady-state desired error, $e_{\Delta F_c}$, due to a polynomial reference input, and the steady-state output, $\Delta F_{c_{dp}}$ due to a low-frequency sinusoidal disturbance in the direct path can be translated as requirements on the sensitivity function. The steady-state response to high-frequency sinusoidal disturbance in the feedback path, $\Delta F_{c_{ds}}$, becomes a requirement on the complementary sensitivity function. The transient requirements define constraints on both sensitivity and complementary sensitivity functions. In particular, the overshoot, $\hat{s}$, defines the bound of the resonance peak for both sensitivity and complementary sensitivity functions, while the rise time, t_r, and settling time, $t_{s,\alpha_\%}$, allow selecting the minimum cutoff frequency. The maximum admissible value for the input signal affects the weight W_2. Disturbances d_f and d_a can be compensated in feedforward, the first

Requirement	Maximum value	Unit
$e_{\Delta F_c}$	5	N
$\Delta F_{c_{dp}}$	0.01	N
$\Delta F_{c_{ds}}$	0.01	N
t_r	0.5	s
$t_{s,2_{\%}}$	1.5	s
$\hat{s}$	15	%

Table 3.1 Inner force loop requirements.

using the friction model described in 2.4, while the second measuring the joint velocity. Table 3.1 lists the desired steady states and transient specifications.

The controller is computed as solution of (3.5) using the Robust Control Toolbox of Matlab. Then several simulation are performed to verify if the closed loop system satisfies the desired performances. Figure 3.9 shows the performances obtained by the inner loop. Figure 3.9a shows the system transient response to a step signal. The steady-state response to ΔF_{c_d} is presented in Fig. 3.9b. The disturbances rejection is highlighted in Figs. 3.9c, 3.9d, and 3.9e. The frequency domain performance indicators are depicted in Fig. 3.9f. All the requirements are satisfied by the proposed controller.

3.2.2 Outer Loop Controller

The performances provided by the inner controller allows considering the actuator-cables system as a unitary static gain if the input signal has a bandwidth lower than the cutoff frequency of the closed loop system. Under this assumption, it is possible to study the stability of the outer position loop as for classical industrial manipulators.

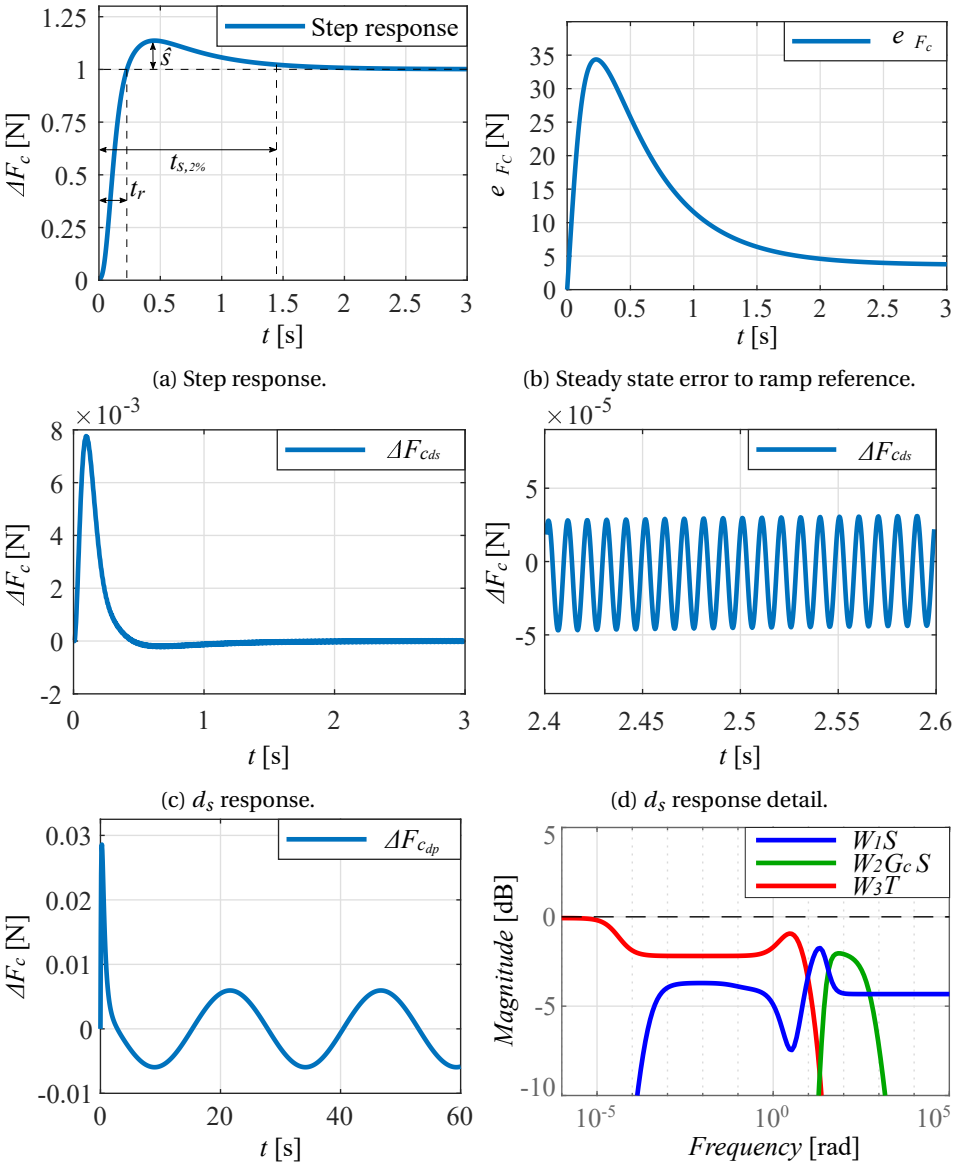

(a) Step response.

(b) Steady state error to ramp reference.

(c) d_s response.

(d) d_s response detail.

(e) d_p response.

(f) Performance indicator.

Figure 3.9 Inner loop controller design results.

According to the Hamiltonian mechanics [78], (2.35) can be written as

$$\begin{cases} \dot{\boldsymbol{q}}_{\boldsymbol{r}} = \dfrac{\partial \mathcal{H}}{\partial \boldsymbol{p}_{\boldsymbol{r}}} \left(\boldsymbol{q}_{\boldsymbol{r}}, \boldsymbol{p}_{\boldsymbol{r}} \right) \\ \dot{\boldsymbol{p}}_{\boldsymbol{r}} = -\dfrac{\partial \mathcal{H}}{\partial \boldsymbol{q}_{\boldsymbol{r}}} \left(\boldsymbol{q}_{\boldsymbol{r}}, \boldsymbol{p}_{\boldsymbol{r}} \right) + J_l \left(\boldsymbol{q}_{\boldsymbol{r}} \right) \boldsymbol{u} \\ \boldsymbol{y} = J_l^T \left(\boldsymbol{q}_{\boldsymbol{r}} \right) \dfrac{\partial \mathcal{H}}{\partial \boldsymbol{p}_{\boldsymbol{r}}} \left(\boldsymbol{q}_{\boldsymbol{r}}, \boldsymbol{p}_{\boldsymbol{r}} \right) \end{cases} \tag{3.14}$$

where $\mathcal{H}$, called Hamiltonian, represents the total energy of the system, $\boldsymbol{u} = \Delta \boldsymbol{F_c}$, and $\boldsymbol{y} = \boldsymbol{v_j}$ represent the input and output variables of the system respectively. The Legendre transform relates the Hamiltonian to Lagrangian [78] as follows:

$$\mathcal{H} = \boldsymbol{p_r}^T \dot{\boldsymbol{q}}_{\boldsymbol{r}} - \mathcal{L} = \mathcal{T} + \mathcal{U}. \tag{3.15}$$

Let now consider the well known PD plus gravity compensation controller defined as

$$\boldsymbol{u} = \boldsymbol{g} \left(\boldsymbol{q}_{\boldsymbol{r}} \right) + K_P \left(\boldsymbol{q_d} - \boldsymbol{q}_{\boldsymbol{r}} \right) - K_D J_l^T \left(\boldsymbol{q}_{\boldsymbol{r}} \right) \dot{\boldsymbol{q}}_{\boldsymbol{r}}, \tag{3.16}$$

where $K_P = K_P^T \succ 0$ and $K_D = K_D^T \succ 0$. This controller can be written as

$$\boldsymbol{u} = \beta \left(\boldsymbol{q}_{\boldsymbol{r}} \right) + \boldsymbol{v} \left(\boldsymbol{q}_{\boldsymbol{r}}, \dot{\boldsymbol{q}}_{\boldsymbol{r}} \right), \tag{3.17}$$

where $\beta \left(\boldsymbol{q}_{\boldsymbol{r}} \right) = \boldsymbol{g} \left(\boldsymbol{q}_{\boldsymbol{r}} \right) + K_P \left(\boldsymbol{q_d} - \boldsymbol{q}_{\boldsymbol{r}} \right)$ and $\boldsymbol{v} \left(\boldsymbol{q}_{\boldsymbol{r}}, \dot{\boldsymbol{q}}_{\boldsymbol{r}} \right) = -K_D J_l^T \left(\boldsymbol{q}_{\boldsymbol{r}} \right) \dot{\boldsymbol{q}}_{\boldsymbol{r}}$. The gravity compensation and the proportional terms allow shaping the storage function as

$$\mathcal{H}_d = \frac{1}{2} \boldsymbol{p_r}^T M^{-1} \left(\boldsymbol{q}_{\boldsymbol{r}} \right) \boldsymbol{p}_{\boldsymbol{r}} + \frac{1}{2} \left(\boldsymbol{q_d} - \boldsymbol{q}_{\boldsymbol{r}} \right)^T K_p \left(\boldsymbol{q_d} - \boldsymbol{q}_{\boldsymbol{r}} \right) \tag{3.18}$$

to force an equilibrium point in the desired joint position, $\left(\boldsymbol{q}_{\boldsymbol{r}}, \boldsymbol{p}_{\boldsymbol{r}} \right) = \left(\boldsymbol{q_d}, \boldsymbol{0} \right)$. The derivative term add some damping to ensure the convergence to the equilibrium

point. Then the dynamic equations of the closed loop system become

$$\begin{cases} \dot{\boldsymbol{q}}_{\boldsymbol{r}} = \dfrac{\partial \mathcal{H}_d}{\partial \boldsymbol{p}_{\boldsymbol{r}}} \left(\boldsymbol{q}_{\boldsymbol{r}}, \boldsymbol{p}_{\boldsymbol{r}} \right) \\ \dot{\boldsymbol{p}}_{\boldsymbol{r}} = -\dfrac{\partial \mathcal{H}_d}{\partial \boldsymbol{q}_{\boldsymbol{r}}} \left(\boldsymbol{q}_{\boldsymbol{r}}, \boldsymbol{p}_{\boldsymbol{r}} \right) + J_l \left(\boldsymbol{q}_{\boldsymbol{r}} \right) \boldsymbol{v} \left(\boldsymbol{p}_{\boldsymbol{r}} \right) \\ \boldsymbol{y} = J_l^T \left(\boldsymbol{q}_{\boldsymbol{r}} \right) \dfrac{\partial \mathcal{H}_d}{\partial \boldsymbol{p}_{\boldsymbol{r}}} \left(\boldsymbol{q}_{\boldsymbol{r}}, \boldsymbol{p}_{\boldsymbol{r}} \right) \end{cases} \tag{3.19}$$

It is possible to demonstrate the stability of the closed loop system considering $\mathcal{H}_d$ as Lyapunov candidate function. Differentiating $\mathcal{H}_d$ with respect to time yields

$$\begin{aligned} \dot{\mathcal{H}}_d \left(\boldsymbol{q}_{\boldsymbol{r}}, \boldsymbol{p}_{\boldsymbol{r}} \right) &= \frac{\partial^T \mathcal{H}_d}{\partial q_r} \left(\boldsymbol{q}_{\boldsymbol{r}}, \boldsymbol{p}_{\boldsymbol{r}} \right) \dot{\boldsymbol{q}}_{\boldsymbol{r}} + \frac{\partial^T \mathcal{H}_d}{\partial q_r} \left(\boldsymbol{q}_{\boldsymbol{r}}, \boldsymbol{p}_{\boldsymbol{r}} \right) \dot{\boldsymbol{p}}_{\boldsymbol{r}} \\ &= \left(J_l \left(\boldsymbol{q}_{\boldsymbol{r}} \right) \boldsymbol{v} \left(\boldsymbol{p}_{\boldsymbol{r}} \right) - \dot{\boldsymbol{p}}_{\boldsymbol{r}} \right)^T \dot{\boldsymbol{q}}_{\boldsymbol{r}} + \dot{\boldsymbol{q}}_{\boldsymbol{r}}{}^T \dot{\boldsymbol{p}}_{\boldsymbol{r}} \\ &= \boldsymbol{v}^T \left(\boldsymbol{p}_{\boldsymbol{r}} \right) J_l^T \left(\boldsymbol{q}_{\boldsymbol{r}} \right) \dot{\boldsymbol{q}}_{\boldsymbol{r}} \\ &= -\dot{\boldsymbol{q}}_{\boldsymbol{r}}{}^T J_l \left(\boldsymbol{q}_{\boldsymbol{r}} \right) K_D J_l^T \left(\boldsymbol{q}_{\boldsymbol{r}} \right) \dot{\boldsymbol{q}}_{\boldsymbol{r}}. \end{aligned} \tag{3.20}$$

Recalling that $K_P \succ 0$, $K_D \succ 0$, and $J_l \left(\boldsymbol{q}_{\boldsymbol{r}} \right)$ is full rank, then $\mathcal{H}_d > 0$ and $\dot{\mathcal{H}}_d < 0$ and the Lyapunov stability criterion is satisfied. All the parameters of the outer loop controller are listed in appendix B.

3.3 Results

The performances of the proposed cascade control algorithm were verified first through a simulation and then experimentally on the last two links of the prototype presented in section 1.2 whose parameters are listed in appendix A. It was possible to test the algorithm only on the last two joints of the robot due to the number of available sensors.

The model of the two links cable-driven robot, described by (2.40), was implemented in Simulink, including the friction model described by (2.22). The entire controller derived in the previous sections is described by Fig. 3.10. Both friction and disturbance induced by the joint velocity are compensated in feedforward. The reference signal $\boldsymbol{q}_{\boldsymbol{r}_d}$ is defined by a trajectory from 0 to $\pi/6$ rad with

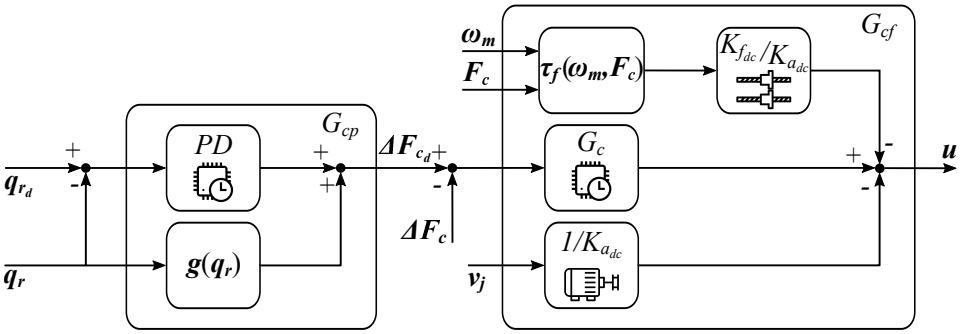

Figure 3.10 Entire cascade controller for a two links cable-driven robot.

	Acceleration		Constant velocity		Unit
	Simulation	Experiment	Simulation	Experiment	
e_{q_5}	2.7×10^{-3}	4.9×10^{-3}	1.5×10^{-3}	1.4×10^{-3}	[rad]
e_{q_6}	3.7×10^{-3}	7.1×10^{-3}	1.5×10^{-3}	0.7×10^{-3}	[rad]
$e_{\Delta_{F_{c_5}}}$	6.7	18.3	0.8	6.8	[N]
$e_{\Delta_{F_{c_6}}}$	10.6	27.9	0.5	10.0	[N]

Table 3.2 Maximum tracking error using the cascade controller in both acceleration and constant velocity phase.

a trapezoidal velocity profile. The maximum profile velocity and acceleration are 0.02 rad/s and 0.01 rad/s^2. The maximum position, and force errors are achieved during the acceleration phase for both the controlled joints. Table 3.2 lists the maximum value of the error for both the inner and outer loop during the acceleration phase and the constant velocity phase. Figure 3.11 compares the simulation and experimental results for the outer and inner loops.

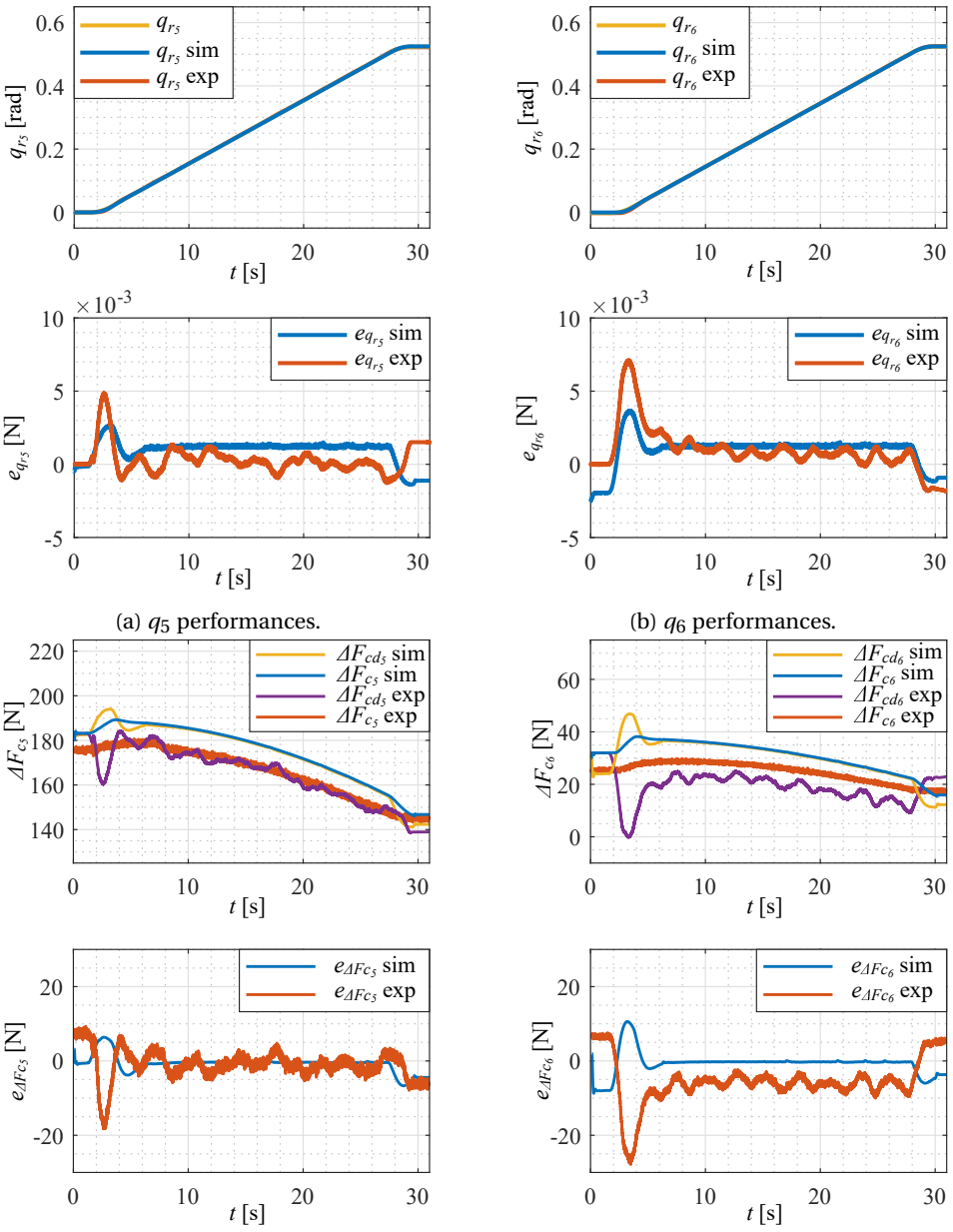

(a) q_5 performances.

(b) q_6 performances.

(c) ΔF_{c_5} performances.

(d) ΔF_{c_6} performances.

Figure 3.11 Inner loop controller design results for a two links cable-driven robot.

CHAPTER 4

GRAVITY COMPENSATION

Cable-driven hyper-redundant robots for inspection usually need to have a large workspace. Even if cable-driven actuation allows moving the actuator from the joints to the chassis, reducing the overall mass of the system, long structures cause the need for more powerful actuators, or a high reduction ratio in order to overcome the pull of gravity. In this scenario, the study of mechanisms reducing static force is crucial to increasing energy efficiency, and improving dynamic response. In particular, the vibration introduced by the elasticity of cable-driven transmissions needs for fast actuators to be damped. This requirement is in contrast with the need of high reduction ratio. In this chapter a convex optimisation method to design passive torque generators [79] is presented with the aim of reducing the static torque due to gravity forces allowing to design faster actuators able to deal with the vibration of the system.

4.1 LITERATURE REVIEW

Different types of weight compensation mechanisms are presented and categorised in [80]. The counterweight mechanism in [81] allows moving the centre of mass of each link to the joint axis of rotation. This technique allows smooth dynamic behaviours but has the drawback of increasing the total inertia and volume of the system.

Authors in [82] propose a magnetic balancing mechanism by exploiting the fact that two nested Halbach cylinders produce a sinusoidal torque enabling the compensation of that produced by a gravitational load over a complete rotation of a revolute joint. Even if this solution is difficult to finely tune and obtaining perfect compensation is not possible, it has the advantages of being extremely compact with the cylinders mounted in axis with the joint as well as the possibility to be modular; several modules can thus be combined in series to increasing torques.

Spring mechanisms are widely studied because they add less inertia than counterweight and are simpler to implement than the magnetic mechanism, but, on the other side, it is more difficult to perfectly match the non-linear joint torque induced by gravity and to obtain a smooth dynamic behaviour.

Torsional springs are rarely used compared to axial ones since it is more complex to adapt and adjust their behaviour to achieve static balance [83]. Radaelli et al. obtain good results for balancing an inverted pendulum with pre-stressed torsion bars [84].

The use of axial springs is well-documented in [85]. There are different ways to connect the spring to the system to compensate for the gravity torques. The simplest one is to connect the springs directly to the manipulator links. However, this technique leads to an exact compensation only if a zero-free length spring is used, and even in this case, it is complex to fine-tune the mechanism [86]. Besides, there is also the risk that the protruded spring may interfere with other parts of the robot. To improve the gravity compensation of the before-mentioned mechanisms Arakelian et al. introduce auxiliary links to minimise the residual unbalance [87]. Kim et al. in [88] design a device partially compensating the torque produced by gravity force on a 6 degrees of freedom manipulator using a linear spring. Axial springs are applied to compensate for the gravity torque acting on robotic waists. Yun et al. design a 3 degrees of freedom mechanism capable of compensating up to 23 kg load [89]. Reinecke et al. present a 2 degrees of freedom device able to balance the weight of the upper body of a robot that moves dynamically[90].

More elaborated techniques involving cables, additional links, pulleys, and cams solve the problems related to zero-free length spring and interference with other parts of the mechanism. For example, a pulley and a cable can be arranged to simulate a zero-free length spring by storing away the initial length of the spring [91, 92]. Nguyen et al. in [93, 94] considerably reduce the peak torque produced by gravity force acting on a planar articulated robotic arm and a parallel delta robot employing gear-spring modules.

Pulleys and cams with non-circular shapes increase the number of design parameters in the system, simplifying the optimisation of gravity compensation mechanisms [95–97]. Fedorov et al. propose mechanisms based on a pair of differential non-circular pulleys to generate non-monotonic torque profiles through a geometrical method [98]. In [99], Kim et al. define an analytical solution to find the shape of non-circular pulleys employed to generate an arbitrary torque profile. One of the limits of this work is that the authors do not consider all the constraints on the feasibility of the pulley. In particular, they do not count the potential presence of non-regular points [100], where the rope cannot perfectly wrap the pulley. Furthermore, during the design phase, evaluating constraints is not possible, so it is necessary to iterate the design by tuning some parameters, such as the spring stiffness, the spring initial length, or the insertion point, until a feasible solution is obtained.

4.2 Baseline: Analytic Solution for Non-Circular Pulleys Design

Consider the mechanism represented in Fig. 4.1, where O is the origin of the reference frame O_{xy}. The pulley, body B_1, is fixed to the ground. On one side, the linear extension spring is attached to the link, body B_2, at insertion point R. On the other side, it is fixed at the anchor point A through a cable that wraps around the pulley. $r_m(\theta)$ represents the moment arm that, multiplied by the spring force at joint position θ, determines the torque applied to the joint. The spring force line of action is tangent to the pulley and passes through the insertion point

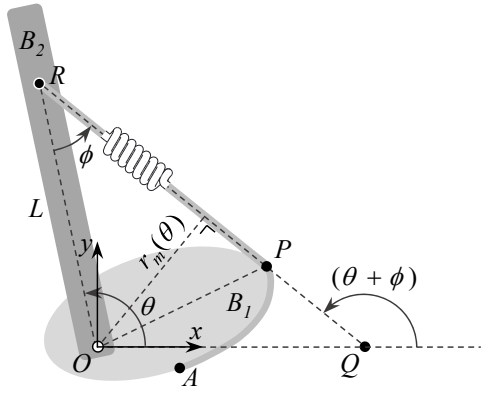

Figure 4.1 Schematic diagram of a passive torque generator composed of a spring and a non-circular pulley.

R and the point Q. R is located at a distance L from the origin O. The point P represents the tangent point between $\overline{RQ}$ and the pulley. The angle formed by the intersection of the direction of the spring force and the line passing through the point O and R is called ϕ.

Given the spring stiffness k, and its initial length, u_0, the pulley profile is determined in closed form, as shown in [99] under the assumptions that the spring behaviour is linear, no pulley is present on the insertion point, and the cable is rigid with negligible diameter. The derivation of such closed form solution is summarised as follows:

$$r_m(\theta) = \frac{\tau_d(\theta)}{\sqrt{2k\int_{\theta_0}^{\theta}\tau_d(\alpha)\,d\alpha + k^2u_0^2}}, \tag{4.1}$$

$$\phi = \sin^{-1}\left(\frac{r_m(\theta)}{L}\right), \tag{4.2}$$

$$S(\theta) = \tan\left(\theta+\phi\right), \tag{4.3}$$

$$Y(\theta) = L\left[\sin\theta - \cos\theta\cdot\tan\left(\theta+\phi\right)\right], \tag{4.4}$$

$$\left(x_p(\theta), y_p(\theta)\right) = \left(-\frac{Y'(\theta)}{S'(\theta)}, Y(\theta) - \frac{Y'(\theta)}{S'(\theta)}S(\theta)\right), \tag{4.5}$$

where x_p and y_p are x- and y-Cartesian coordinates of the pulley profile represented in the frame O_{xy}, respectively.

However, it is worth noticing that the pulley shape obtained through this method could be unrealistic. As discussed in previous works [99, 101], to get a feasible pulley, it is necessary to avoid that the radius of the pulley contour goes to infinite and the shape must be convex. This condition can be translated into a constraint on the curvature of the profile as follows:

$$1 + \phi'(\theta) \neq 0. \tag{4.6}$$

Besides, the pulley profile cannot have non-regular points because, in these points, the rope cannot wrap perfectly. This condition is satisfied if the zeros of $x'_P(\theta)$ are different from the zeros of $y'_P(\theta)$.

4.3 Proposed Method Based on Convex Optimisation

In this section, a convex optimisation problem to compute the moment arm $r_m(\theta)$ as its solution, guaranteeing the feasibility of the pulley shape, has been formulated. This approach enables conditions on the pulley profile to be included as constraints of the optimisation problem and promises a feasible shape at the expense of introducing an error in the torque generation.

4.3.1 Cost function definition

The objective function of the optimisation problem is derived directly from (4.1). The angle θ is discretised over the range of motion of the joint from the initial angle θ_i to the final θ_f, given by

$$\boldsymbol{\theta} \in \mathbb{R}^n : \ \boldsymbol{\theta} = \begin{bmatrix} \theta_0 & \theta_1 & \dots & \theta_{n-1} \end{bmatrix}^T.$$

Without loss of generality it is possible to parametrise the moment arm as a polynomial of order m as follows:

$$\begin{aligned} \boldsymbol{r}_m &= \beta_0 \mathbb{1} + \beta_1 \boldsymbol{\theta} + \beta_2 \boldsymbol{\theta}^2 + \ldots + \beta_m \boldsymbol{\theta}^m = \\ &= \begin{bmatrix} \mathbb{1} & \boldsymbol{\theta} & \boldsymbol{\theta}^2 & \ldots & \boldsymbol{\theta}^m \end{bmatrix} \cdot \boldsymbol{\beta} = \\ &= H \cdot \boldsymbol{\beta}. \end{aligned} \tag{4.7}$$

Define the angle increment as $d\alpha = \frac{\theta_f - \theta_i}{n}$ and the vector $\boldsymbol{v}$ as

$$\boldsymbol{v} \in \mathbb{R}^{\mathrm{n}} : \mathrm{v_i} = \sqrt{2\mathrm{k} \sum_{\alpha=0}^{\mathrm{i}} \tau_{\mathrm{d}}(\theta_\alpha)\, \mathrm{d}\alpha + \mathrm{k}^2 \mathrm{u}_0^2}, \quad \forall \theta_\alpha \in \boldsymbol{\theta}. \tag{4.8}$$

Substituting $\boldsymbol{v}$ in (4.1) yields the moment arm equation rewritten as

$$\mathrm{diag}(\boldsymbol{v}) \cdot \left(H \cdot \boldsymbol{\beta}\right) - \boldsymbol{\tau}_d = 0. \tag{4.9}$$

By squaring the ℓ_2-norm of (4.9), one can then obtain a convex objective function which minimises the sum of the torque residuals squared as follows:

$$f_0\left(\boldsymbol{\beta}\right) = \left\| \mathrm{diag}(\boldsymbol{v}) \cdot \left(H \cdot \boldsymbol{\beta}\right) - \boldsymbol{\tau}_d \right\|_2^2. \tag{4.10}$$

4.3.2 Constraints definition

Moment arm bounds

The moment arm $r_m(\theta)$ must be greater than 0 and smaller than the insertion length L. Otherwise, the mobile link would hit the non-circular pulley and there would be no space to insert the spring. These conditions can be written as follows:

$$\left\| H \cdot \boldsymbol{\beta} \right\|_\infty < L, \tag{4.11}$$

$$\left\| H \cdot \boldsymbol{\beta} \right\|_\infty > 0. \tag{4.12}$$

CURVATURE CONSTRAINT

As discussed in Section 4.2, to avoid collision between the cable and other parts of the non-circular pulley, the pulley shape needs to be convex. The straightforward way to satisfy this condition is to introduce a constraint on the curvature of the pulley, so that it does not change the sign.

Starting from (4.6) it is possible to write this constraint as

$$\begin{aligned} 1+\phi' > 0 \quad \cup \quad 1+\phi' < 0 \quad \Rightarrow \\ 1+\frac{r'_m}{\sqrt{L^2-r_m^2}} > 0 \quad \cup \quad 1+\frac{r'_m}{\sqrt{L^2-r_m^2}} < 0. \end{aligned} \tag{4.13}$$

The disequalities (4.13) can be written as

$$\begin{aligned} & r'_m > -\sqrt{L^2-r_m^2} \quad \cup \quad r'_m < -\sqrt{L^2-r_m^2} \quad \Rightarrow \\ & \begin{cases} r_m^2 < L^2 \\ r'_m \leq 0 \\ r_m^2 + r_m'^2 < L^2 \end{cases} \cup \begin{cases} r_m^2 < L^2 \\ r'_m \geq 0 \end{cases} \cup \begin{cases} r_m^2 < L^2 \\ r'_m \leq 0 \\ r_m^2 + r_m'^2 > L^2. \end{cases} \end{aligned} \tag{4.14}$$

The set generated by (4.14) is not convex, as shown in Fig. 4.2a. Many different convex subsets of (4.14) can be considered to obtain a convex formulation of the curvature constraint. The main effect of reducing the feasible set is not to reach the global optimum, but the optimal solution belonging to the convex subset considered. A possible choice for the convex approximation of (4.14) is represented by

$$r_m^2 + r_m'^2 < L^2. \tag{4.15}$$

As shown in Fig. 4.2b, the set described by (4.15) is convex and satisfies the constraint on the curvature of the pulley profile. Furthermore, choosing (4.15) as curvature constraint, the variation of the moment arm is bounded. This additional condition makes r_m smooth allowing to obtain a pulley on which the rope can perfectly wrap.

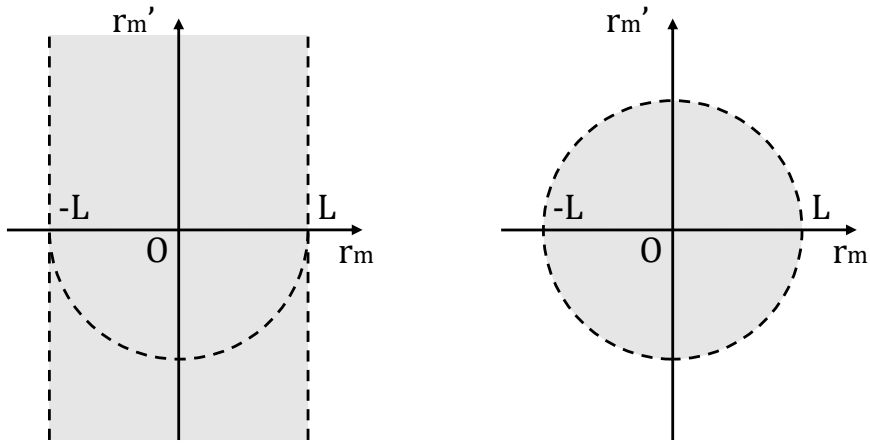

(a) Curvature constraint defined by the set (4.14).

(b) Curvature constraint defined by the convex approximation of (4.14) as (4.15).

Figure 4.2 Geometric representation of the curvature constraint. Dashed lines and White regions represent the points excluded in the set.

As for r_m, r'_m can be written in terms of the discretised angle $\boldsymbol{\theta}$ and the design variables $\boldsymbol{\beta}$

$$\begin{aligned} \boldsymbol{r}'_m &= \beta_1 \mathbb{1} + 2\beta_2\boldsymbol{\theta} + 3\beta_3\boldsymbol{\theta}^2 + \ldots + m\beta_m\boldsymbol{\theta}^{m-1} = \\ &= \begin{bmatrix} \mathbb{1} & 2\boldsymbol{\theta} & 3\boldsymbol{\theta}^2 & \ldots & m\boldsymbol{\theta}^{m-1} \end{bmatrix} \cdot \boldsymbol{\beta} = \\ &= H_d \cdot \boldsymbol{\beta}. \end{aligned} \tag{4.16}$$

Finally, by substituting (4.16) into (4.15), the curvature constraint can be written as a set of quadratic constraints in $\boldsymbol{\beta}$ as follows:

$$\boldsymbol{\beta}^T \cdot \left(H_i^T H_i + H_{d_i}^T H_{d_i} \right) \cdot \boldsymbol{\beta} < L^2, \quad i = 1 \ldots n, \tag{4.17}$$

where H_i and H_{d_i} are respectively the rows of H and H_d. This type of constraint can be easily implemented using well-known convex optimisation algorithms.

NON-REGULAR POINTS AVOIDANCE

Consider the parametric curve defined in (4.5)

$$\gamma(\theta) = \begin{cases} x_p(\theta) = -\dfrac{Y'(\theta)}{S'(\theta)} \\ y_p(\theta) = Y(\theta) - \dfrac{Y'(\theta)}{S'(\theta)} S(\theta). \end{cases}$$

Non-regular points of $\gamma(\theta)$ are all the values of θ such that $\gamma'(\theta) = \mathbf{0}$ [100].
The derivative of $\gamma(\theta)$ can be written as

$$\gamma'(\theta) = \begin{cases} x'_p(\theta) = -h(\theta) \\ y'_p(\theta) = -h(\theta) S(\theta). \end{cases} \tag{4.18}$$

where

$$h(\theta) = \frac{Y''S' - Y'S''}{S'^2}. \tag{4.19}$$

From (4.3) and (4.4), one can compute Y and its derivatives as

$$Y = L[\sin(\theta) - \cos(\theta) S], \tag{4.20}$$

$$Y' = L\left[\cos(\theta)\left(1 - S'\right) + \sin(\theta) S\right], \tag{4.21}$$

$$Y'' = L\left[\sin(\theta)\left(2S' - 1\right) + \cos(\theta)\left(S - S''\right)\right]. \tag{4.22}$$

Substituting (4.20)-(4.22) into (4.19) gives h as a function of θ, S, S' and S'' only,

$$h = L\frac{\sin(\theta)\left[2S'^2 - S' - SS''\right] + \cos(\theta)\left[SS' - S''\right]}{S'^2}. \tag{4.23}$$

The points in which $\gamma'(\theta) = \mathbf{0}$ are the zeros of the function $h(\theta)$. Since S'^2 is always different from zero, and imposing $h(\theta) = 0$, the following equation is obtained:

$$\tan(\theta) = \frac{SS' - S''}{2S'^2 - S' - SS''}. \tag{4.24}$$

Moreover considering that

$$S'(\theta) = \left(1+S^2\right)\left(1+\phi'\right), \tag{4.25}$$

$$S''(\theta) = \left(1+S^2\right)\left[2S\left(1+\phi'\right)^2+\phi''\right], \tag{4.26}$$

equation (4.24) can be rewritten as

$$\tan(\theta) = \frac{\phi'' + Sg\left(\phi'\right)}{-S\phi'' + g\left(\phi'\right)}, \tag{4.27}$$

where

$$g\left(\phi'\right) = \left(1+\phi'\right)\left[2\left(1+\phi'\right)-1\right]. \tag{4.28}$$

By using (4.3) and (4.27), the following equation is obtained:

$$\begin{aligned}\phi'' &= -g\left(\phi'\right)\frac{\tan\left(\theta+\phi\right)-\tan(\theta)}{1+\tan(\theta)\tan\left(\theta+\phi\right)} = \\ &= -g\left(\phi'\right)\tan\left(\phi\right).\end{aligned} \tag{4.29}$$

Finally computing the derivatives of ϕ and substituting (4.2) and (4.28) into (4.29) gives

$$r_m'' + r_m\left(1+3\frac{r_m'}{\sqrt{L^2-r_m^2}}+3\frac{r_m'^2}{L^2-r_m^2}\right) = 0. \tag{4.30}$$

Considering that

$$1+3\frac{r_m'}{\sqrt{L^2-r_m^2}}+3\frac{r_m'^2}{L^2-r_m^2} \geq \frac{1}{4}, \tag{4.31}$$

it is possible to write the following inequality:

$$r_m'' + r_m\left(1+\frac{3r_m'}{\sqrt{L^2-r_m^2}}+\frac{3r_m'^2}{L^2-r_m^2}\right) \geq r_m'' + \frac{1}{4}r_m. \tag{4.32}$$

Equation (4.32) demonstrates that

$$r''_m + \frac{1}{4} r_m > 0 \Rightarrow h(\theta) \neq 0. \tag{4.33}$$

Note that r''_m and r_m can be written in terms of the discretised angle $\boldsymbol{\theta}$ and the design variables $\boldsymbol{\beta}$ as

$$\begin{aligned} \boldsymbol{r}''_m &= 2\beta_2 \mathbb{1} + 6\beta_3 \boldsymbol{\theta} + \ldots + m(m-1)\beta_m \boldsymbol{\theta}^{m-2} = \\ &= \begin{bmatrix} 2 \cdot \mathbb{1} & 6\boldsymbol{\theta} & \ldots & m(m-1)\boldsymbol{\theta}^{m-2} \end{bmatrix} \cdot \boldsymbol{\beta} = \\ &= H_{dd} \cdot \boldsymbol{\beta}. \end{aligned} \tag{4.34}$$

Accordingly, to avoid non-regular points in the pulley shape, it is enough to add the following linear constraints:

$$\left\| \left(H_{dd} + \frac{1}{4} H \right) \cdot \boldsymbol{\beta} \right\|_\infty > 0. \tag{4.35}$$

4.3.3 Optimisation problem

With considering the cost function (4.10) and constraints (4.11), (4.12), (4.17) and (4.35), the problem of designing a non-circular pulley for torque generation can be solved as the convex optimisation problem described by

$$\begin{aligned} \min_{\boldsymbol{\beta}} \quad & \left\| \operatorname{diag}(\boldsymbol{v}) \cdot \left(H \cdot \boldsymbol{\beta} \right) - \boldsymbol{\tau}_d \right\|_2^2 \\ \text{s.t.} \quad & \left\| H \cdot \boldsymbol{\beta} \right\|_\infty > 0 \\ & \left\| H \cdot \boldsymbol{\beta} \right\|_\infty < L \\ & \left\| \left(H_{dd} + \frac{1}{4} H \right) \cdot \boldsymbol{\beta} \right\|_\infty > 0 \\ & \boldsymbol{\beta}^T \cdot \left(H_i^T H_i + H_{d_i}^T H_{d_i} \right) \cdot \boldsymbol{\beta} < L^2 \quad i = 1 \ldots N. \end{aligned} \tag{4.36}$$

In this optimisation problem, the cost function is quadratic and the constraints are linear or quadratic inequalities. This family of convex problems can be solved as a semidefinite program using robust and efficient algorithms.

4.4 Design examples

In this section, the comparison between the analytical and the proposed convex optimisation solution is presented through two examples. The first describes the design of non-circular pulleys for compensating the gravity force acting on an inverted pendulum. The second presents the design of non-circular pulleys able to produce a generic torque profile. This example highlights the benefit introduced by the convex optimisation approach. The design algorithm is implemented in Matlab, and the optimisation problem is solved using the CVX toolbox [102, 103].

4.4.1 Gravity compensation of the inverted pendulum

In this example, the inverted pendulum presented in Fig. 4.3 is taken into account. The desired torque for compensating the gravity force acting on this mechanism is represented in Fig. 4.5a and is defined as follows:

$$\tau_d(\theta) = \tau_{max}\cos(\theta), \tag{4.37}$$

where $\tau_{max} = F_g\,\overline{OG}$.

As described in [99], to generate a bidirectional torque, two antagonistic pulleys are necessary. The desired torque has to be divided into two different sub-profiles to compensate for the gravity force acting on the pendulum in the

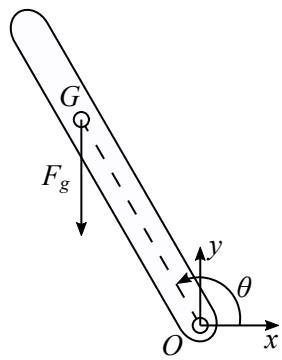

Figure 4.3 Schematic of the force acting on an inverted pendulum.

range of motion $[\theta_i, \theta_f]$. The symmetry of τ_d and the choice of the splitting torque coefficient $\lambda = 0.5$ entail that the profile of the two antagonistic pulleys is symmetric, as explained in [99]. Table 4.1 lists the parameters selected to define the torque sub-profiles.

Figure 4.4 presents both profiles obtained by the analytical and convex optimisation solution. The algorithm provides only the profile points generated by the angles belonging to the desired range of motion. Accordingly, the two boundary points have to be connected by any smooth curve to produce the entire profile. The light blue shape in Fig. 4.4 shows a possible complete pulley profile for the convex optimisation solution.

The design result highlights that the proposed algorithm generates a pulley profile able to approximate the desired torque with a maximum error of 2.2 Nm while the analytical solution has a maximum error of 0.9 Nm better approximating the desired torque. Figure 4.5b shows the torque error produced by both the solutions.

Symbol	Value	Unit	Description
M	15	Kg	Pendulum mass
l	1	m	Pendulum length
τ_{max}	147.1	Nm	Maximum desired torque
d_{off}	79.6	Nm	Torque offset
λ	0.5	-	Splitting torque coefficient
k	$30 \cdot 10^3$	N/m	Spring stiffness
u_0	0.015	m	Spring initial elongation
L	0.25	m	Spring insertion point
θ_i	$\pi/6$	rad	Initial angle
θ_f	$5/6\pi$	rad	Final angle
m	5	-	Cost function polynomial order
$d\alpha$	$8.378 \cdot 10^{-3}$	rad	Motion range discretisation

Table 4.1 Inverted pendulum example parameters.

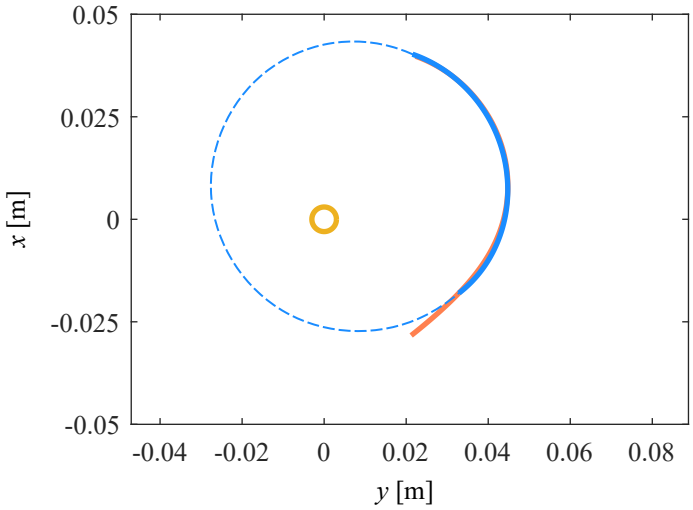

Figure 4.4 Pulley shape for the inverted pendulum. The solid red line represents the shape obtained with the analytical solution. The solid blue line represents the convex optimisation solution. The complete pulley shape is represented by the dashed blue for the convex optimisation solution. The jellow circle represents the joint shaft

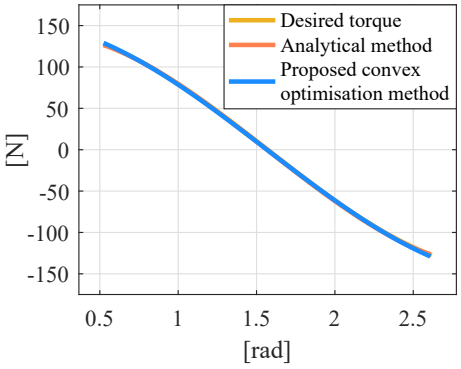

(a) Comparison of the desired torque with the torque produced by the analytical solution and the proposed convex optimisation solution.

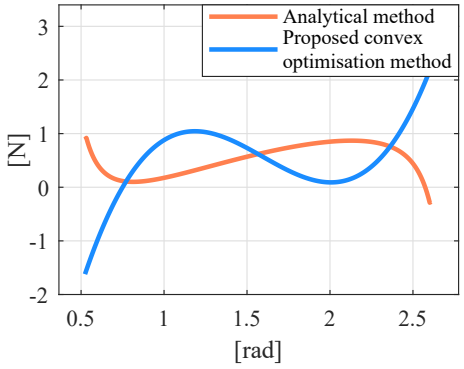

(b) Torque error produced by the analytical (red) and the convex optimisation (blue) solution for the inverted pendulum.

Figure 4.5 Design results for the inverted pendulum example.

To better evaluate the results, the error has been put in perspective with the desired torque. The percentage error is computed as the relative percent

difference as follows:

$$e_{\%} = \left(2\frac{\tau_d - \tau}{|\tau_d| + |\tau|}\right) \times 100. \tag{4.38}$$

This formulation allows to bound the value of the percentage error in the range $[-200, 200]$ even if the desired torque is equal to zero. Table 4.2 compares the absolute and percentage error, respectively e_{abs} and $e_{\%}$, for both the analytical and the proposed convex optimisation method in different joint configurations. When $\theta = \pi/2$, the desired torque is zero, so the percentage error reaches the maximum value. Nevertheless, the residual torque is about 0.6 Nm.

The stiffness and the initial length of the spring have to be set before running the optimisation algorithm. These parameters can be employed to define the size of pulleys or, when the analytical solution is unfeasible, to find a realistic shape. Knowing the maximum desired torque, τ_{max}, the size of the pulley is strictly related to the spring constant and initial length. Let assume to wrap the cable on a circular pulley. Under this assumption the maximum elongation of the spring is

$$u_{max} = \left(\theta_f - \theta_i\right) r + u_0, \tag{4.39}$$

Angle [rad]	Analytical solution		Convex solution	
	e_{abs} [Nm]	$e_{\%}$	e_{abs} [Nm]	$e_{\%}$
$\pi/6$	0.9	0.7	−1.6	−1.2
$\pi/4$	0.1	0.1	0.2	0.2
$\pi/3$	0.2	1.1	0.9	1.0
$5\pi/12$	0.4	2.0	1.0	2.6
$\pi/2$	0.6	(200.0)*	0.6	(200.0)*
$7\pi/12$	0.8	1.2	0.2	0.5
$2\pi/3$	0.9	0.7	0.1	0.2
$3\pi/4$	0.8	−0.2	0.7	0.7
$5\pi/6$	0.3	−1.2	2.2	1.8

* Bounded to the maximum value since the desired torque is zero.

Table 4.2 Torque error for the inverted pendulum example.

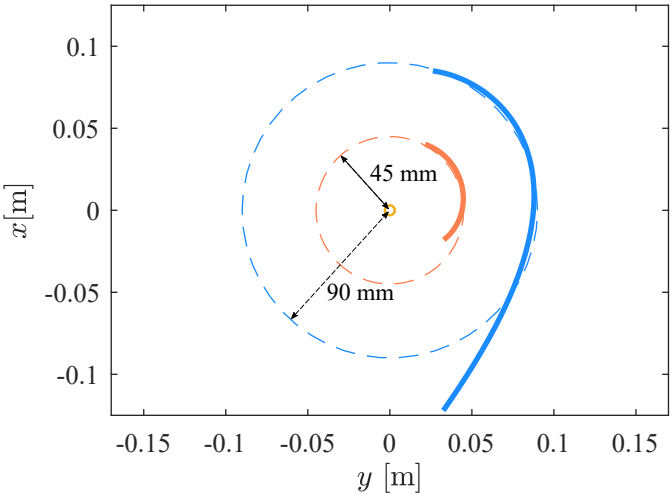

Figure 4.6 Comparison between the obtained pulley with a desired radius of 90 mm and of 45 mm.

where r is the pulley radius and u_0 the initial elongation. Thus the maximum torque acting on the pulley is computed as

$$\tau_{max} = k u_{max} r = k r \left[\left(\theta_f - \theta_i \right) r + u_0 \right]. \tag{4.40}$$

Given the desired radius and a preliminary initial elongation, the order of magnitude of the spring constant is estimated from (4.40) as follows:

$$k = \frac{\tau_{max}}{\left(\theta_f - \theta_i \right) r^2 + u_0 r}. \tag{4.41}$$

As for any commercial components, the stiffness of springs can take a finite number of values. Thus, the initial elongation of the spring is computed as

$$u_0 = \frac{\tau_{max}}{kr} - \left(\theta_f - \theta_i \right) r, \tag{4.42}$$

to obtain the desired radius using the stiffness of the selected commercial spring. To verify this relation let assume that a radius of about 45mm and a preliminary

Symbol	Value	Unit	Description
a	147.1	Nm	Torque parameter
c	84.4	Nm	Torque parameter
d_{off}	86.4	Nm	Torque offset
λ	0.5	-	Splitting torque coefficient
k	$30 \cdot 10^3$	N/m	Spring stiffness
u_0	0.015	m	Spring initial elongation
L	0.25	m	Spring insertion point
θ_i	$\pi/6$	rad	Initial angle
θ_f	$5/6\pi$	rad	Final angle
m	5	-	Cost function polynomial order
$d\alpha$	$8.378 \cdot 10^{-3}$	rad	Motion range discretisation

Table 4.3 Generic torque example parameters.

initial elongation of 0.015mm are required. Then from (4.41) it is possible to estimate the spring stiffness as $k \approx 30 \cdot 10^3$N/m. Let now assume that a radius of about 90mm and a preliminary initial elongation of 0.015mm are required. Then from (4.41) it is possible to estimate the spring stiffness as $k \approx 8 \cdot 10^3$N/m. Figure 4.6 shows the two pulley profile obtained with the different spring elastic constant and the circles of the desired radius.

4.4.2 Generic torque profile creation

To verify that the proposed convex optimisation method always finds a feasible solution, in this example, the generic torque, represented in Fig. 4.8a and defined as

$$\tau_d(\theta) = a(\cos(\theta) - \sin(\theta)) + c, \tag{4.43}$$

is considered.

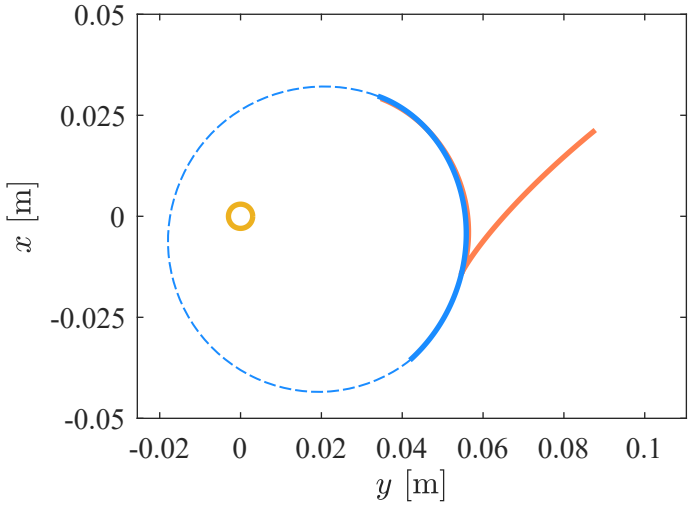

Figure 4.7 Pulley shape to produce the generic torque (4.43). The solid red line represents the shape obtained with the analytical solution. The solid blue line represents the convex optimisation solution. The complete pulley shape is represented by the dashed blue line for the convex optimisation solution. The jellow circle represents the joint shaft

Since τ_d is not symmetric, both the analytical and convex optimisation methods generate two antagonistic pulleys with different profiles. Table 4.3 lists the selected parameters to designing the pulleys.

In this torque profile, the analytical solution produces an unfeasible shape for both the antagonistic pulleys. The first pulley does not satisfy the curvature constraints, whereas the second contains a non-regular point. Since the two pulleys have unfeasible shapes, the length of the cables wrapping on the pulleys is not defined, making it impossible to compute the torque produced by the analytical solution

The convex optimisation approach, instead, can satisfy all the constraints producing feasible shapes. Figure 4.7 shows one of the two pulley profile obtained by both the convex optimisation and the analytical solution where the presence of a non-regular point is evident.

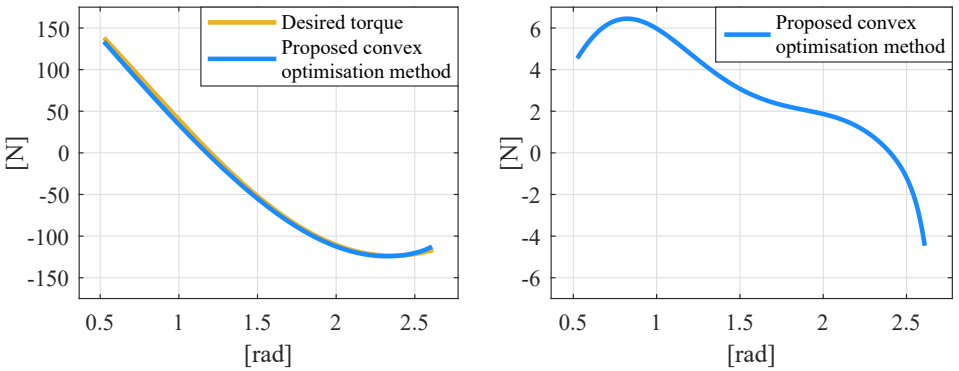

(a) Profile of the desired torque (4.43) and the torque generated by the convex optimisation solution.

(b) Torque error produced by the convex optimisation solution for the desired torque (4.43).

Figure 4.8 Design results for the generic torque example.

Angle [rad]	Convex solution	
	e_{abs} [Nm]	$e_{\%}$
$\pi/6$	4.5	3.3
$\pi/4$	6.4	7.9
$\pi/3$	5.7	20.4
$5\pi/12$	4.1	19.5
$\pi/2$	2.8	4.4
$7\pi/12$	2.1	2.2
$2\pi/3$	1.7	1.4
$3\pi/4$	0.4	0.3
$5\pi/6$	-4.5	-3.9

Table 4.4 Torque error for the generic torque example.

The two antagonist pulleys, generated by the convex optimisation solution, can approximate the desired torque with a maximum error of 6.4 Nm, as shown in Fig. 4.8b. Percentage errors are given in Table 4.4.

The curvature constraint for both analytical and convex optimisation solution is shown in Fig. 4.9a, where it is possible to notice that the analytical solution

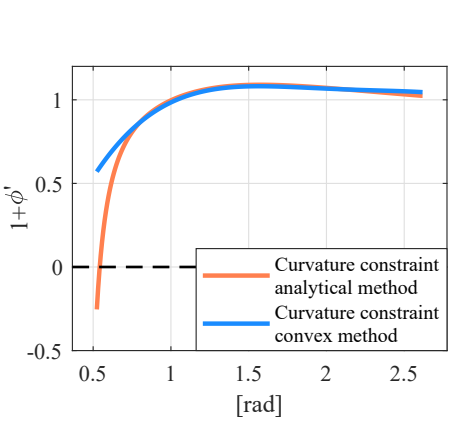

(a) Graphical representation of curvature constraint for both the analytical and convex optimisation solution.

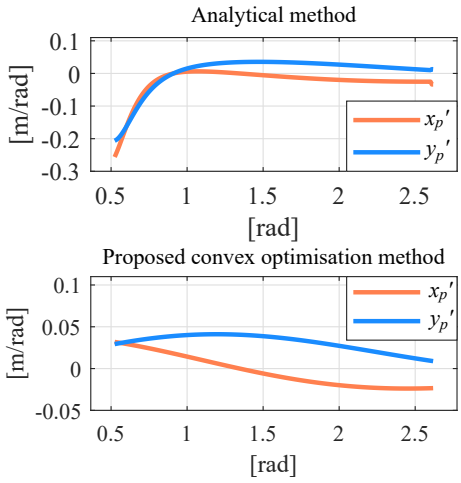

(b) Graphical representation of non-regular point constraint for both the analytical and convex optimisation solution.

Figure 4.9 Graphical representation of constraint satisfaction.

has a zero in $\theta = 0.54$ rad, violating the constraint. In Fig. 4.9b, the non-regular point constraint is represented for both the analytical and convex optimisation solution. In the analytical solution appears a non-regular point in $\theta = 0.91$ rad.

CHAPTER 5

SPATIAL ROBOT PRELIMINARY STUDIES

The modelling framework, developed in chapter 2, can be applied to any cable-driven hyper-redundant robot. In this chapter preliminary analysis on modelling a fully actuated cable-driven hyper-redundant robot able to move in three-dimensional space is presented. A description of the joint kinematics and dynamics is presented, then a novel friction model for cable sliding into bushing is proposed. A preliminary prototype composed of a single joint, whose parameters are listed in appendix A.5, has been developed to validate the proposed friction model.

5.1 SPATIAL ROBOT MODEL

A first concept of a spatial cable-driven hyper-redundant robot has been designed. The robot, shown in Fig. 5.1, is composed of five joints whose kinematics allows the two driving cables not to lose tension during the motion. This property comes out from the constraint that forces the shortening and the lengthening of the two driving cables to be the same. A dedicated device, such as a 3-axis gimbal system, can be also added to the end-effector to reach any attitude in the Cartesian space. So, for the task of positioning the end-effector in the Cartesian space, this robot has two degrees of redundancy. The cables are routed along the structure of the robot through bushings. The cables pass straight inside

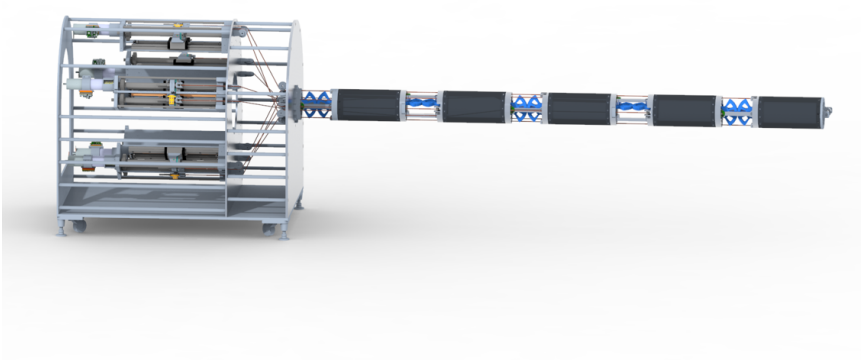

Figure 5.1 CAD model of the novel three-dimensional motion cable-driven hyper-redundant robot.

the joints, but they change direction passing inside the link from one joint to the other. Furthermore, the twin cables pass always in diametrically opposite locations inside the joint. Table 5.1 lists the DH parameters [7] describing the kinematics of the robot.

Joint	a_i [mm]	α_i [rad]	d_i [mm]	θ_i [rad]
1	0	$\pi/2$	0	q_{r_1}
1_c	150	0	0	q_{r_1}
2	350	$-\pi/2$	0	q_{r_2}
2_c	150	0	0	q_{r_2}
3	350	$\pi/2$	0	q_{r_3}
3_c	150	0	0	q_{r_3}
4	350	$-\pi/2$	0	q_{r_4}
4_c	150	0	0	q_{r_4}
5	350	$\pi/2$	0	q_{r_5}
5_c	150	0	0	q_{r_5}

Table 5.1 DH parameters of the robot.

5.1.1 Actuator Model

In the actuator employed to perform the preliminary experiments on the gear joint, the linear motion necessary to move the cables is obtained through ball-screws coupled with a brushless DC electric motor through an harmonic gear. The parameters describing the actuator are listed in appendix A.5. In this mechanism the friction phenomena are mainly related to harmonic drives. The four dominant aspects of harmonic gears are: non-linear viscous friction, nonlinear stiffness, hysteresis, and kinematic error [104]. Since load applied on the actuator by a single joint is low, and the cable actuation has a much lower stiffness than the harmonic gear, the dominant behaviour of the transmission is the non-linear viscous friction that can be modelled as

$$\tau_{f_i} = \alpha_i \arctan\left(\beta_i \omega_{m_i}\right). \tag{5.1}$$

where α_i and β_i are the model parameters and ω_{m_i} is the i^{th} motor velocity.

5.1.2 Joint Model

The cable-driven joint proposed for the design of the three-dimensional motion hyper-redundant robot consists of two rigid links and two parallel revolute joints whose rotation angles are constrained to be same through a gear system. Figure 5.2 shows the mechanism schematic, where O_1 and O_2 represent the first and second rotation axes respectively, and $P_{c_{m_1}}$ and $P_{c_{m_2}}$ are the centre of mass of the first and second links, respectively, while P_{ee} is the end effector position. $P_{c_{m_1}}$, $P_{c_{m_2}}$ and P_{ee} are described as follows:

$$P_{c_{m_1}} = \begin{bmatrix} d_{11}\cos\left(q_r\right) \\ d_{11}\sin\left(q_r\right) \end{bmatrix}, \tag{5.2}$$

$$P_{c_{m_2}} = \begin{bmatrix} l_1\cos\left(q_r\right) + d_{21}\cos\left(2q_r\right) \\ l_1\sin\left(q_r\right) + d_{21}\sin\left(2q_r\right) \end{bmatrix}, \tag{5.3}$$

$$P_{ee} = \begin{bmatrix} l_1\cos\left(q_r\right) + l_2\cos\left(2q_r\right) \\ l_1\sin\left(q_r\right) + l_2\sin\left(2q_r\right) \end{bmatrix}, \tag{5.4}$$

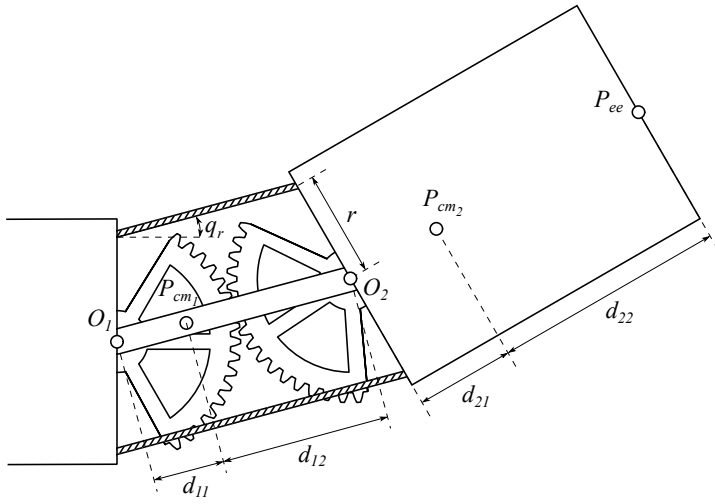

Figure 5.2 Schematic of the cable driven joint proposed for the design of the three-dimensional motion hyper-redundant robot.

where q_r denotes the angular position of the joint, d_{11} and d_{12} represent the distance between the centre of mass of the first link and O_1 and O_2, respectively, d_{21} and d_{22} represent the distance between the centre of mass of the second link and O_2 and P_{ee}, respectively, and $l_1 = d_{11} + d_{12}$ and $l_2 = d_{21} + d_{22}$ represent the length of the first and second links.

The bond-graph representing this mechanical system, depicted in Fig. 5.3, can be easily obtained through (5.2), (5.2), and (5.4). The state equation of the system is given by

$$\dot{p}_r = \frac{\left[-4m_2 l_1 d_{21} \sin\left(q_r\right)\right] p_r^2 + J_1^2 r \cos\left(q_r\right) \Delta F_{c_i} + J_1^2 \tau_g}{J_1 \left[J_1 + 4J_2 + m_1 d_{11}^2 + m_2 \left(l_1^2 + 4 l_1 d_{21} \cos\left(q_r\right) + 4 d_{21}^2\right)\right]}, \tag{5.5}$$

where p_r denotes the state variable representing the angular momentum of the joint, m_1, J_1, and m_2, J_2 are respectively the mass and inertia of the first and second links, r is the distance of the cable anchor point from the centre of the flange, ΔF_{c_i} is the difference between the forces applied by the two cables, and

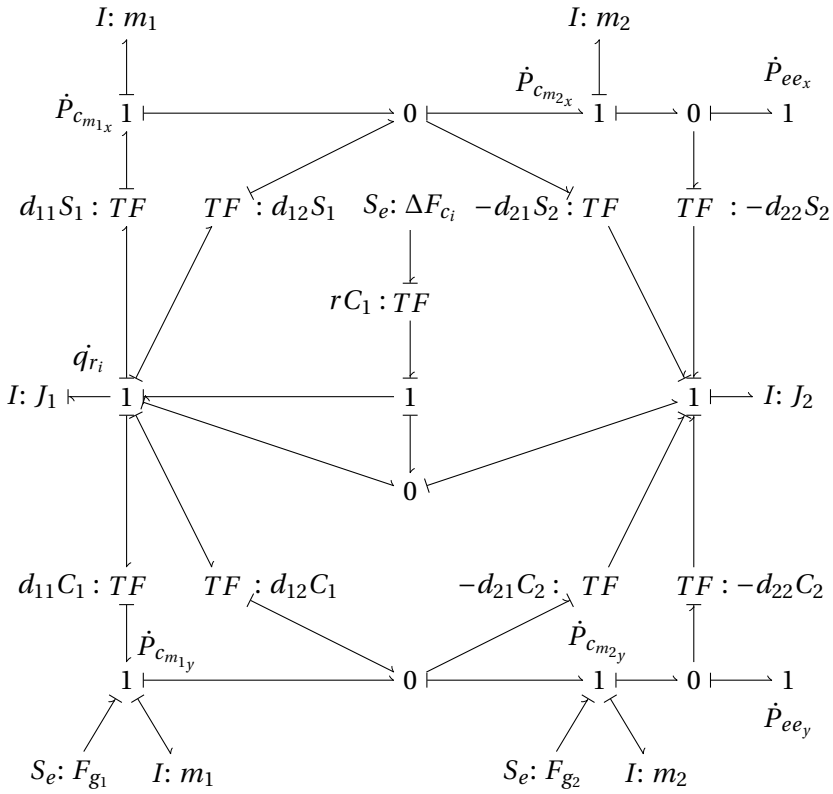

Figure 5.3 Bond graph model of the joint proposed for the design of the three-dimensional motion robot.

τ_g is the torque due to gravity which is described as

$$\tau_g = d_{11}\cos(q_r)F_{g_1} + (l_1\cos(q_r) + 2d_{21}\cos(2q_r))F_{g_2}, \tag{5.6}$$

where F_{g_1} and F_{g_2} are the gravity forces acting on the first and second links respectively.

5.1.3 MULTIBODY MODEL

As described in section 2.6 the dynamic equation of the multibody system is computed exploiting the Hamiltonian mechanics and is described by 2.35. Dif-

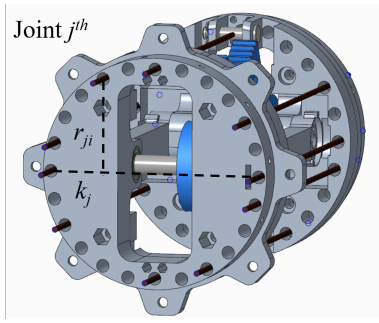

Figure 5.4 Schematic of the distribution of the routing bushings on the joint.

ferently from the prototype presented in chapter 1, in this device the cables need for being routed along the structure producing a coupling between the joint variables. This coupling is reflected in the Jacobian matrix, $J_l(\boldsymbol{q_r})$. The map between the joints configuration, $\boldsymbol{q_r}$, and the i^{th} linear position of cables anchor points, L_i, is computed as

$$L_i = \sum_{j=1}^{i} r_{ji} \sin(q_{r_j}), \tag{5.7}$$

where r_{ji} represents the distance between the i^{th} cable and the line k_j which lies on the input flange of the j^{th} joint. Figure 5.4 shows the schematic of the cable routing in the j^th joint. The derivative respect to time of (5.7) leads to define the Jacobian matrix as

$$J_l(\boldsymbol{q_r}) = \begin{bmatrix} r_{11}\cos(q_{r_1}) & 0 & \dots & 0 \\ r_{12}\cos(q_{r_1}) & r_{22}\cos(q_{r_2}) & \ddots & \vdots \\ \vdots & \vdots & \ddots & 0 \\ r_{1n}\cos(q_{r_1}) & r_{2n}\cos(q_{r_2}) & \dots & r_{nn}\cos(q_{r_n}) \end{bmatrix} \tag{5.8}$$

highlighting the coupling between the linear motion of the i^{th} anchor point and the motion of the joint variables. Since the range of motion of the joint is defined as $q_r \in [-\pi/3, \pi/3]$ by geometry, $J_l(\boldsymbol{q_r})$ is always full rank .

5.1.4 Sliding Cable Friction Model

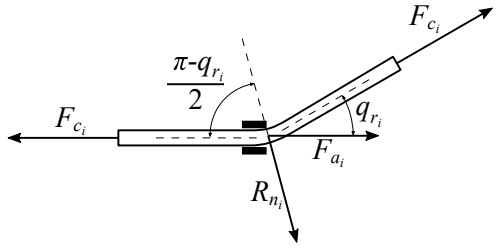

Figure 5.5 Schematic of the forces acting on the i^{th} sliding cable.

Friction is one of classic, yet challenging problems in practical system modelling. Several friction models have been defined in literature: static friction model consists in a combination of Coulomb, viscous, stiction and Stribeck terms, and an accurate description of friction is given by dynamic models such as Dahl or LuGree friction model [105]. For cable-driven mechanisms, friction forces produced by pulleys can be modelled as a function of the cable tension, velocity, wrap angle and number of pulleys [106]. An attempt to define a general formulation for multi-node sliding cable is presented in [107]. To describe the friction force produced by sliding rope into bushing a modified version of the Dahl's model has been proposed [108]. However, aforementioned models are not able to correctly describe the friction forces generated by cables sliding into bushings or are too complex to be easily implemented in a real time controller.

In this section the mathematical friction model of cables sliding into a bushing is presented [109]. The aim is to define a simple model that can be easily employed as feedforward term in a control scheme to improve the trajectory tracking performances of cable-driven mechanisms.

Under the assumption that the relative velocity between cables and bushings is low it is possible to neglect viscous friction phenomena and consider only stiction. Then the static friction acting on the i^{th} cable is computed as

$$F_{a_i} = \mu_i \left| F_{n_i} \right|, \tag{5.9}$$

where μ_i represents the static friction coefficient and F_{n_i} is the force normal to the contact point. Fig. 5.5 shows a schematic of the forces acting on the cable in a given joint configuration q_{r_i}. From the equilibrium equation it is possible to find the reaction force R_{n_i} given by the bushing as follows:

$$R_{n_i} = \begin{bmatrix} F_{c_i}\left(1-\cos\left(q_{r_i}\right)\right) \\ -F_{c_i}\sin\left(q_{r_i}\right) \end{bmatrix}, \tag{5.10}$$

where F_{c_i} is the norm of the force applied to the cable. Considering that F_{n_i} lies on the bisector of the angle between the entrance and exit direction of the cable the module of F_{n_i} can be computed as the projection of R_{n_i} on such bisector

$$\left|F_{n_i}\right| = 2F_{c_i}\left|\sin\left(\frac{q_{r_i}}{2}\right)\right|. \tag{5.11}$$

By substituting (5.11) into (5.9), the static friction force can be determined as

$$F_a = 2\mu F_{c_i}\left|\sin\left(\frac{q_{r_i}}{2}\right)\right|. \tag{5.12}$$

Equation (5.12) shows that static friction in cable-driven mechanism is not constant with respect to joint configuration. To deal with possible asymmetries in the mechanism due to manufacturing imperfection and uncertainties on parameters, such as friction coefficient between cables and bushings, a generalised model for the stiction of a cable driven mechanism can be described by the following equation:

$$F_{a_i} = \begin{cases} a_{1_i} + b_{11_i}F_{c_i}\sin\left(\dfrac{q_{r_i}-c_{1_i}}{2}\right) & v_{s_i} > 0, \quad q_i \geq c_{1_i} \\ a_{1_i} + b_{12_i}F_{c_i}\sin\left(\dfrac{q_{r_i}-c_{1_i}}{2}\right) & v_{s_i} > 0, \quad q_i < c_{1_i} \\ 0 & v_{s_i} = 0 \\ a_{2_i} + b_{21_i}F_{c_i}\sin\left(\dfrac{q_{r_i}-c_{2_i}}{2}\right) & v_{s_i} < 0, \quad q_i \geq c_{2_i} \\ a_{2_i} + b_{22_i}F_{c_i}\sin\left(\dfrac{q_{r_i}-c_{2_i}}{2}\right) & v_{s_i} < 0, \quad q_i < c_{2_i}, \end{cases} \tag{5.13}$$

where v_{s_i} is the relative velocity between the i^{th} cable and the bushing, a_{k_i} is a static force related to the inversion of motion, b_{kj_i} is the double of the friction coefficient between the cable and the bushing and c_{k_i} takes into account the manufacturing error.

5.2 Parameter Identification

The hardware setup used to identify the model parameters consists of a gear joint driven by a linear actuator able to move two twin cables in opposite directions and a pulley mechanism that aligns the cables with the joint geometry. Two force sensors are used to measure the forces applied to the joint. All the parameters of the testbench are reported in appendix A.2

5.2.1 Harmonic Gear Friction Parameters Identification

To identify the α and β parameters of (5.1), the actuator has been driven in velocity mode with no load attached. In this configuration an array of velocity set points has been sent to the motor. For each velocity set point the mean value of the torque and its standard deviation have been computed. Such values have been used to identify the friction model parameters using the non-linear least square algorithm provided by the curve fitting toolbox of Matlab. Figure 5.6 shows the fit result and the uncertainty associated to each point. The identified

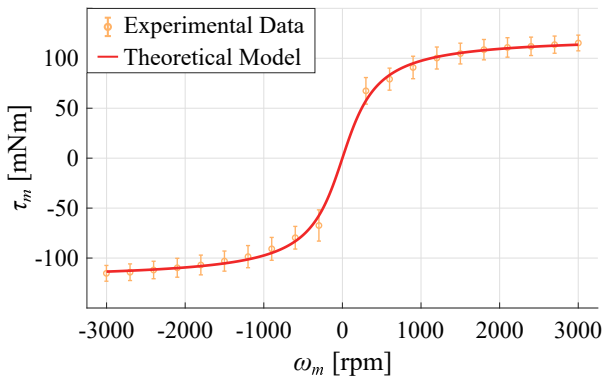

Figure 5.6 Actuator friction parameter identification.

coefficients and their 95% confidence level bounds are listed in table 5.2.

Coefficient	Value	Uncertainty	Unit
α	77.7	± 1.9	mNm
β	20×10^{-3}	$\pm 4 \times 10^{-3}$	s/rad

Table 5.2 Harmonic gear friction parameters.

5.2.2 Sliding Cable Friction Parameters Identification

The coefficients of the sliding cable friction model are estimated measuring the cables forces in the whole range of motion of the joint. The trajectory implemented to estimate the sliding cable friction is made by three set-points to explore the whole range of motion of the joint under investigation. Every movement is implemented with a trapezoidal velocity profile. During the motion the cable tension force, the angular position of the joint, and the linear velocity of the actuator are recorded. The acquired data are lowpass filtered with a cut-off frequency of 1Hz in order to reduce high frequency noise. Then the mean value of the force measured is subtracted to remove the bias induced by the preload of the cable. Finally the non linear fit algorithm has been implemented to find the friction coefficients for both the cables. Fig. 5.7 shows fit results while the identified parameters and their 95% confidence level bounds are listed in Table 5.3.

To validate the sliding cable friction model the entire systems has been simulated in Simulink. Figures 5.8a and 5.8b show the forces measured during the experiment on the first and the second cable respectively and the corresponding forces obtained by the simulation. The joint velocity has been computed by numerically differentiating the joint angular position. Figs. 5.8c and 5.8d depict the joint angular velocity and position measured during the experiment and simulation. During the test, the measured velocity plot shows a sinusoidal disturbance, which is caused by the harmonic gear torque ripple not considered in the modeling. As shown by plots Figs. 5.8a and 5.8b , the forces measured on

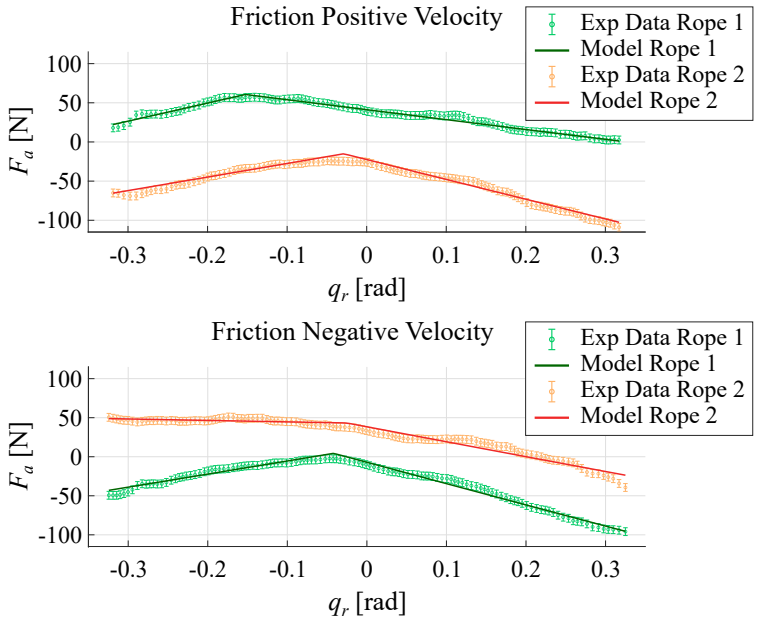

Figure 5.7 Cable friction identification.

Coefficient	Cable 1		Cable 2		Unit
	Value	Uncertainty	Value	Uncertainty	
a_1	60.60	$\pm 5 \times 10^{-}2$	-15.11	$\pm 6 \times 10^{-}2$	N
a_2	4.35	$\pm 5 \times 10^{-}2$	43.24	$\pm 1 \times 10^{-}1$	N
b_{11}	-0.7088	$\pm 1 \times 10^{-3}$	-1.411	$\pm 2 \times 10^{-}3$	-
b_{12}	1.283	$\pm 5 \times 10^{-3}$	0.966	$\pm 3 \times 10^{-}3$	-
b_{21}	-1.5211	$\pm 2 \times 10^{-3}$	-1.066	$\pm 3 \times 10^{-}3$	-
b_{22}	0.9346	$\pm 2 \times 10^{-3}$	-0.104	$\pm 3 \times 10^{-}3$	-
c_1	-0.1524	$\pm 3 \times 10^{-4}$	-0.0289	$\pm 3 \times 10^{-}4$	rad
c_2	-0.04185	$\pm 2 \times 10^{-4}$	-0.0254	$\pm 7 \times 10^{-}4$	rad

Table 5.3 Sliding cable friction parameters.

both the cables are accurately described by the forces computed by the proposed friction model. Furthermore the experimental data lie under the uncertainty bounds obtained from the identification procedure. Figs. 5.8a and 5.8b present a

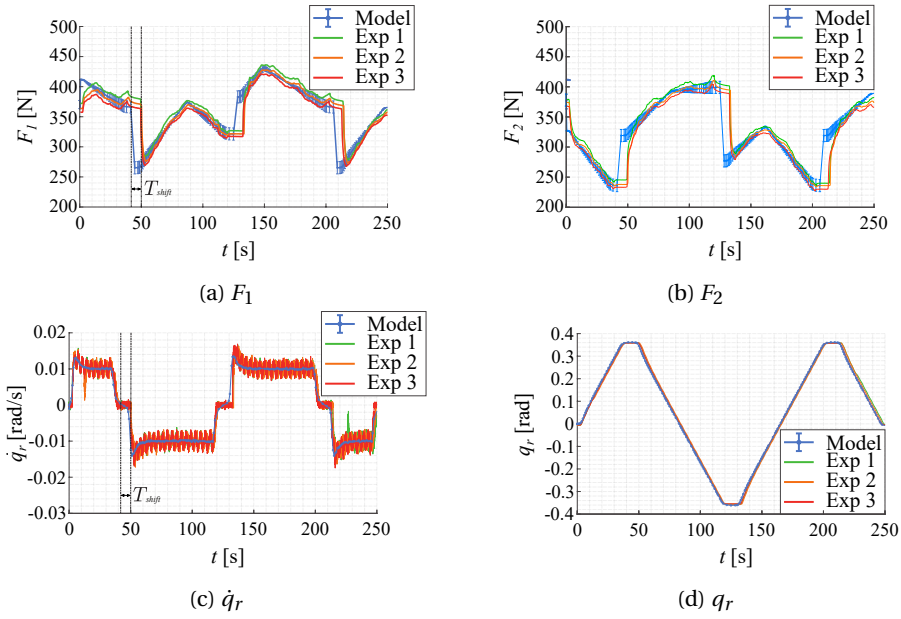

(a) F_1 (b) F_2

(c) $\dot{q}_r$ (d) q_r

Figure 5.8 Sliding cable friction comparison between simulation and experimental data.

temporal shift T_{shift} in force discontinuities. This phenomenon arises because, even if the joint velocity is almost zero, in the simulation appears a change of direction of the motion not present in the real joints. This small difference cause an ill-timed jump in the forces observed. This timing issue is not a problem in implementing this friction model as a feedforward term in a control scheme since the velocity reference is a priori known and does not suffer from such error.

CHAPTER 6

CONCLUSION AND FUTURE WORKS

6.1 CONCLUSION

In this work, the bond-graph formalism has been exploited to derive a unified modelling framework for cable-driven hyper-redundant robots. First, each subsystem composing a cable-driven hyper-redundant robot has been analysed. Therefore its dynamic equations derived. Then all the subsystems have been connected to obtain the model of the entire system in Hamiltonian form.

The obtained model has been employed to formulate a cascade control algorithm composed of two loops. The inner force loop is designed according to the $\mathscr{H}_\infty$ control theory. This theory allows finding the optimal controller able to robustly stabilise a system subject to uncertainties satisfying at the same time the requirements about nominal performances. First, the uncertainty model related to synthetic fibre cables has been derived. This model also included the neglected dynamics of the actuators. Then, time-domain requirements have been translated into weighting functions to shape the sensitivity and complementary sensitivity function. The simulation results show that the proposed controller can robustly stabilise the inner loop providing the desired time-domain requirements. The outer loop consists of a PD plus gravity compensation controller. Its stability has been demonstrated using the Lyapunov stability criterion. The

obtained cascade controller was verified on a two links cable-driven robot by comparing the experimental data with the simulation results.

Damping residual vibrations induced by cables need for fast actuators. Thus, a novel methodology to design passive torque generators based on non-circular pulleys and axial springs has been proposed. Relieving the actuators from generating static torques due to gravity allows improving the dynamic response of the system. The design of the pulley profile has been framed as a convex optimisation problem. This approach allows considering all the geometric constraints from the beginning. The proposed method always produces feasible pulley shapes even if a small error is introduced in the approximation of the desired torque.

Finally, the proposed modelling framework has been applied to a novel fully actuated cable-driven hyper-redundant robot to check its versatility. In particular, a novel friction model for cables sliding into bushing has been proposed and verified experimentally.

The unified modelling framework proposed in this dissertation proves to be an effective tool for designing novel robotic devices. It allows building both a simulation environment and a design framework systematically interconnecting simple or complex models of all the subsystems composing the different devices. In a context where it is necessary to develop highly customised solutions, this modelling approach allows speeding up the preliminary analysis on the proposed devices to evaluate the effectiveness of different solutions highlighting possible critical aspects. Furthermore, describing each subsystem by different complexity models allows employing the optimal model for the various scenarios the designer would analyse. Simplified models are preferred to design control algorithms, while complex models are favoured to obtain accurate simulations to observe secondary dynamics.

6.2 Future Works

Building on the achievements reached through this dissertation, different paths open up to advance the modelling and control of cable-driven hyper-redundant robots described in this work. Further analyses on synthetic fibre cables could be

performed to improve the model proposed in section 2.5 by including hysteresis phenomena not considered in this work. The control algorithm described in chapter 3 could be modified for implementing it on the entire robot proposed in section 1.2. Different control algorithms could be investigated with the aim to remove the force sensors in the control loop. The gravity compensation mechanism presented in chapter 4 could be integrated on the robots described in section 1.2 and 5.1 to partially relieve actuators from overcoming the pull of gravity and increase their dynamic response. The design of an active pulley able to modify its shape in real-time could be investigated to improve the gravity compensation acting on articulated mechanisms in which the torque depends on all the joint angles. A prototype of the novel cable-driven hyper-redundant robot described in 5.1 could be built to test the control algorithm discussed in chapter 3 including the friction model of sliding cables as feedforward term.

The proposed unified modelling framework is widely applicable. Consequently, it could be employed to describe a large variety of mechatronic systems. The multi-physics nature of the proposed approach allows defining accurate models for both actuators and sensors systems. This aspect could be explored in industrial applications, such as pick and place, to consider in the system modelling the dynamics of hydraulic or pneumatic grippers to obtain a more realistic simulation of the plant. Furthermore, it is possible to include interaction models as additional subsystems to simulate or design collaborative robots that have to interact safely with workers or unstructured environments.

REFERENCES

[1] European commission, "PETROBOT." http://petrobotproject.eu/.

[2] European commission, "ROBINS." https://www.robins-project.eu/.

[3] SPARC, "Robotics 2020 Multi-Annual Roadmap." https://www.eu-robotics.net/sparc/about/index.html, 2016.

[4] A. Pistone, C. Canali, C. Gloriani, S. Leggieri, P. Guardiani, and D. Caldwell, "Reconfigurable inspection robot for industrial applications," *Procedia Manufacturing*, vol. 38, pp. 597–604, 2019.

[5] Microdrones, "Drone inspection." https://www.microdrones.com/en/industry-experts/inspection/.

[6] S. Ma, S. Hirose, and H. Yoshinada, "Development of a hyper-redundant multijoint manipulator for maintenance of nuclear reactors," *Advanced robotics*, vol. 9, no. 3, pp. 281–300, 1994.

[7] W. Khalil and E. Dombre, *Modeling, identification and control of robots*. Butterworth-Heinemann, 2004.

[8] N. Mansard, O. Khatib, and A. Kheddar, "A unified approach to integrate unilateral constraints in the stack of tasks," *IEEE Transactions on Robotics*, vol. 25, no. 3, pp. 670–685, 2009.

[9] T. Petrič, A. Gams, N. Likar, and L. Žlajpah, "Obstacle avoidance with industrial robots," in *Motion and Operation Planning of Robotic Systems*, pp. 113–145, Springer, 2015.

[10] H. Abidi, G. Gerboni, M. Brancadoro, J. Fras, A. Diodato, M. Cianchetti, H. Wurdemann, K. Althoefer, and A. Menciassi, "Highly dexterous 2-module soft robot for intra-organ navigation in minimally invasive surgery," *The International Journal of Medical Robotics and Computer Assisted Surgery*, vol. 14, no. 1, p. e1875, 2018.

[11] N. Simaan, K. Xu, W. Wei, A. Kapoor, P. Kazanzides, R. Taylor, and P. Flint, "Design and integration of a telerobotic system for minimally invasive surgery of the throat," *The International journal of robotics research*, vol. 28, no. 9, pp. 1134–1153, 2009.

[12] R. Buckingham and A. Graham, "Dexterous manipulators for nuclear inspection and maintenance—case study," in *2010 1st International Conference on Applied Robotics for the Power Industry*, pp. 1–6, IEEE, 2010.

[13] R. Buckingham, V. Chitrakaran, R. Conkie, G. Ferguson, A. Graham, A. Lazell, M. Lichon, N. Parry, F. Pollard, A. Kayani, *et al.*, "Snake-arm robots: a new approach to aircraft assembly," tech. rep., SAE Technical Paper, 2007.

[14] G. Endo, A. Horigome, and A. Takata, "Super dragon: a 10-m-long-coupled tendon-driven articulated manipulator," *IEEE Robotics and Automation Letters*, vol. 4, no. 2, pp. 934–941, 2019.

[15] J. Uicker, J. J., "Dynamic Force Analysis of Spatial Linkages," *Journal of Applied Mechanics*, vol. 34, pp. 418–424, 06 1967.

[16] A. K. Bejczy, "Robot arm dynamics and control," tech. rep., National Aeronautics and Space Administration, 1974.

[17] J. M. Hollerbach, "A recursive lagrangian formulation of maniputator dynamics and a comparative study of dynamics formulation complexity," *IEEE Transactions on Systems, Man, and Cybernetics*, vol. 10, no. 11, pp. 730–736, 1980.

[18] D. E. Orin, R. McGhee, M. Vukobratović, and G. Hartoch, "Kinematic and kinetic analysis of open-chain linkages utilizing newton-euler methods," *Mathematical Biosciences*, vol. 43, no. 1-2, pp. 107–130, 1979.

[19] M. W. Walker and D. E. Orin, "Efficient dynamic computer simulation of robotic mechanisms," *Dynamic Systems, Measurement and Control*, vol. 104, no. 3, pp. 205–211, 1982.

[20] R. Featherstone, "The calculation of robot dynamics using articulated-body inertias," *The international journal of robotics research*, vol. 2, no. 1, pp. 13–30, 1983.

[21] R. Featherstone and D. Orin, "Robot dynamics: equations and algorithms," in *Proceedings 2000 ICRA. Millennium Conference. IEEE International Conference on Robotics and Automation. Symposia Proceedings (Cat. No. 00CH37065)*, vol. 1, pp. 826–834, IEEE, 2000.

[22] W. M. Silver, "On the equivalence of lagrangian and newton-euler dynamics for manipulators," *The International Journal of Robotics Research*, vol. 1, no. 2, pp. 60–70, 1982.

[23] W. J. Book, "Recursive lagrangian dynamics of flexible manipulator arms," *The International Journal of Robotics Research*, vol. 3, no. 3, pp. 87–101, 1984.

[24] A. De Luca and B. Siciliano, "Closed-form dynamic model of planar multilink lightweight robots," *IEEE Transactions on Systems, Man, and Cybernetics*, vol. 21, no. 4, pp. 826–839, 1991.

[25] X. Wang and J. K. Mills, "Dynamic modeling of a flexible-link planar parallel platform using a substructuring approach," *Mechanism and machine theory*, vol. 41, no. 6, pp. 671–687, 2006.

[26] R. Belotti, R. Caracciolo, I. Palomba, D. Richiedei, and A. Trevisani, "An updating method for finite element models of flexible-link mechanisms based on an equivalent rigid-link system," *Shock and Vibration*, vol. 2018, 2018.

[27] F. Boyer and P. Coiffet, "Generalization of newton-euler model for flexible manipulators," *Journal of robotic systems*, vol. 13, no. 1, pp. 11–24, 1996.

[28] L. Bascetta and P. Rocco, "Modelling flexible manipulators with motors at the joints," *Mathematical and Computer Modelling of Dynamical Systems*, vol. 8, no. 2, pp. 157–183, 2002.

[29] S. Nicosia, F. Nicolo, and D. Lentini, "Dynamical control of industrial robots with elastic and dissipative joints," *IFAC Proceedings Volumes*, vol. 14, no. 2, pp. 1933–1940, 1981.

[30] M. W. Spong, "Modeling and control of elastic joint robots," *Dynamic Systems, Measurement and Control*, vol. 109, no. 4, pp. 310–318, 1987.

[31] G. Buondonno and A. De Luca, "A recursive newton-euler algorithm for robots with elastic joints and its application to control," in *2015 IEEE/RSJ International Conference on Intelligent Robots and Systems (IROS)*, pp. 5526–5532, IEEE, 2015.

[32] M. Vakil, R. Fotouhi, and P. Nikiforuk, "A new method for dynamic modeling of flexible-link flexible-joint manipulators," *Journal of vibration and acoustics*, vol. 134, no. 1, 2012.

[33] A. Horigome and G. Endo, "Basic study for drive mechanism with synthetic fiber rope–investigation of strength reduction by bending and terminal fixation method," *Advanced Robotics*, vol. 30, no. 3, pp. 206–217, 2016.

[34] A. Horigome and G. Endo, "Investigation of repetitive bending durability of synthetic fiber ropes," *IEEE Robotics and Automation Letters*, vol. 3, no. 3, pp. 1779–1786, 2018.

[35] F. Fichera and M. Grossard, "On the modeling and identification of stiffness in cable-based mechanical transmissions for robot manipulators," *Mechanism and Machine Theory*, vol. 108, pp. 176–190, 2017.

[36] S.-H. Choi and K.-S. Park, "The integrated elasto-plastic cable modeling for cable driven parallel robots (cdprs)," in *2017 17th International Conference on Control, Automation and Systems (ICCAS)*, pp. 420–422, IEEE, 2017.

[37] A. Takata, G. Endo, K. Suzumori, H. Nabae, Y. Mizutani, and Y. Suzuki, "Modeling of synthetic fiber ropes and frequency response of long-distance cable–pulley system," *IEEE Robotics and Automation Letters*, vol. 3, no. 3, pp. 1743–1750, 2018.

[38] H. Paynter, "Generalizing the concepts of power transport and energy ports for system engineering," in *ASME Presented at the 1958 Annual Meeting New York. NY*, 1958.

[39] H. M. Paynter, "Hydraulics by analog-an electronic model of a pumping plant," *J. Boston Society of Civil Engineering*, vol. 3, no. 8, pp. 197–219, 1959.

[40] R. C. Rosenberg and D. C. Karnopp, "A Definition of the Bond Graph Language," *Journal of Dynamic Systems, Measurement, and Control*, vol. 94, pp. 179–182, 09 1972.

[41] D. Karnopp, "Power-conserving transformations: physical interpretations and applications using bond graphs," *Journal of the Franklin Institute*, vol. 288, no. 3, pp. 175–201, 1969.

[42] P. C. Breedveld, "A systematic method to derive bond graph models," in *Proc. of the 2nd European Simulation Congress*, pp. 38–44, 1986.

[43] M. Pan, P. J. Gawthrop, K. Tran, J. Cursons, and E. J. Crampin, "Bond graph modelling of the cardiac action potential: implications for drift and non-unique steady states," *Proceedings of the Royal Society A: Mathematical, Physical and Engineering Sciences*, vol. 474, no. 2214, p. 20180106, 2018.

[44] A. K. Pathak and A. Vaz, "An alternative model for contact interaction of mating bones with soft articular cartilage at synovial joints," *Mechanism and Machine Theory*, vol. 150, p. 103858, 2020.

[45] J. T. Machado and M. E. Mata, "A fractional perspective to the bond graph modelling of world economies," *Nonlinear Dynamics*, vol. 80, no. 4, pp. 1839–1852, 2015.

[46] J. W. Brewer, "Progress in the bond graph representations of economics and population dynamics," *Journal of the Franklin Institute*, vol. 328, no. 5-6, pp. 675–696, 1991.

[47] M. A. Djeziri, R. Merzouki, B. O. Bouamama, and G. Dauphin-Tanguy, "Robust fault diagnosis by using bond graph approach," *IEEE/ASME Transactions on Mechatronics*, vol. 12, no. 6, pp. 599–611, 2007.

[48] J. Wu, G. Yu, Y. Gao, and L. Wang, "Mechatronics modeling and vibration analysis of a 2-dof parallel manipulator in a 5-dof hybrid machine tool," *Mechanism and Machine Theory*, vol. 121, pp. 430–445, 2018.

[49] E. Shojaei Barjuei, D. G. Caldwell, and J. Ortiz, "Bond graph modeling and kalman filter observer design for an industrial back-support exoskeleton," *Designs*, vol. 4, no. 4, p. 53, 2020.

[50] R. C. Rosenberg, "State-Space Formulation for Bond Graph Models of Multiport Systems," *Journal of Dynamic Systems, Measurement, and Control*, vol. 93, pp. 35–40, 03 1971.

[51] H. R. Martens, "Simulation of Nonlinear Multiport Systems Using Bond Graphs," *Journal of Dynamic Systems, Measurement, and Control*, vol. 95, pp. 49–54, 03 1973.

[52] F. Lorenz and F. Wolper, "Assigning causality in the case of algebraic loops," *Journal of the Franklin Institute*, vol. 319, no. 1-2, pp. 237–241, 1985.

[53] R. C. Rosenberg, "Exploiting Bond Graph Causality in Physical System Models," *Journal of Dynamic Systems, Measurement, and Control*, vol. 109, pp. 378–383, 12 1987.

[54] S. Birkett and P. Roe, "The mathematical foundations of bond graphs—i. algebraic theory," *Journal of the Franklin Institute*, vol. 326, no. 3, pp. 329 – 350, 1989.

[55] S. Birkett and P. Roe, "The mathematical foundations of bond graphs—ii. duality," *Journal of the Franklin Institute*, vol. 326, no. 5, pp. 691 – 708, 1989.

[56] S. Birkett and P. Roe, "The mathematical foundations of bond graphs—iii. matroid theory," *Journal of the Franklin Institute*, vol. 327, no. 1, pp. 87 – 108, 1990.

[57] S. Birkett and P. Roe, "The mathematical foundations of bond graphs—iv. matrix representations and causality," *Journal of the Franklin Institute*, vol. 327, no. 1, pp. 109 – 128, 1990.

[58] D. C. Karnopp, D. L. Margolis, and R. C. Rosenberg, *System dynamics: modeling, simulation, and control of mechatronic systems*. John Wiley & Sons, 2012.

[59] D. Karnopp, "An approach to derivative causality in bond graph models of mechanical systems," *Journal of the Franklin Institute*, vol. 329, no. 1, pp. 65–75, 1992.

[60] D. Karnopp, "Understanding multibody dynamics using bond graph representations," *Journal of the Franklin Institute*, vol. 334, no. 4, pp. 631–642, 1997.

[61] J. E. Shigley, *Shigley's mechanical engineering design*. Tata McGraw-Hill Education, 2011.

[62] A. De Luca and P. Lucibello, "A general algorithm for dynamic feedback linearization of robots with elastic joints," in *Proceedings. 1998 IEEE International Conference on Robotics and Automation (Cat. No. 98CH36146)*, vol. 1, pp. 504–510, IEEE, 1998.

[63] P. Tomei, "A simple pd controller for robots with elastic joints," *IEEE Transactions on automatic control*, vol. 36, no. 10, pp. 1208–1213, 1991.

[64] A. Van Der Schaft, "Port-hamiltonian systems: an introductory survey," in *Proceedings of the international congress of mathematicians*, vol. 3, pp. 1339–1365, Citeseer, 2006.

[65] R. Ortega, A. J. Van Der Schaft, I. Mareels, and B. Maschke, "Putting energy back in control," *IEEE Control Systems Magazine*, vol. 21, no. 2, pp. 18–33, 2001.

[66] A. Van Der Schaft and D. Jeltsema, "Port-hamiltonian systems theory: An introductory overview," *Foundations and Trends in Systems and Control*, vol. 1, no. 2-3, pp. 173–378, 2014.

[67] A. Albu-Schäffer, C. Ott, and G. Hirzinger, "A unified passivity-based control framework for position, torque and impedance control of flexible joint robots," *The international journal of robotics research*, vol. 26, no. 1, pp. 23–39, 2007.

[68] P. Seibert and R. Suarez, "Global stabilization of nonlinear cascade systems," *Systems & Control Letters*, vol. 14, no. 4, pp. 347–352, 1990.

[69] N. L. Tagliamonte and D. Accoto, "Passivity constraints for the impedance control of series elastic actuators," *Proceedings of the Institution of Mechanical Engineers, Part I: Journal of Systems and Control Engineering*, vol. 228, no. 3, pp. 138–153, 2014.

[70] B. Brogliato, R. Ortega, and R. Lozano, "Global tracking controllers for flexible-joint manipulators: a comparative study," *Automatica*, vol. 31, no. 7, pp. 941–956, 1995.

[71] J. Doyle, K. Glover, P. Khargonekar, and B. Francis, "State-space solutions to standard H_2 and H_∞ control problems," in *1988 American Control Conference*, pp. 1691–1696, IEEE, 1988.

[72] M. Duncan and G. Keith, "A loop-shaping design procedure using H_∞ synthesis," *IEEE Transactions on Automatic Control*, vol. 37, no. 6, pp. 759–769, 1992.

[73] K. Zhou and J. C. Doyle, *Essentials of robust control*, vol. 104. Prentice hall Upper Saddle River, NJ, 1998.

[74] A. J. Van Der Schaft, "L_2-gain analysis of nonlinear systems and nonlinear state feedback H_∞ control," *IEEE transactions on automatic control*, vol. 37, no. 6, pp. 770–784, 1992.

[75] J. S. Yeon and J. H. Park, "Practical robust control for flexible joint robot manipulators," in *2008 IEEE international conference on robotics and automation*, pp. 3377–3382, IEEE, 2008.

[76] M. Makarov, M. Grossard, P. Rodríguez-Ayerbe, and D. Dumur, "Modeling and preview H_∞ control design for motion control of elastic-joint robots with uncertainties," *IEEE Transactions on Industrial Electronics*, vol. 63, no. 10, pp. 6429–6438, 2016.

[77] H. K. Khalil and J. W. Grizzle, *Nonlinear systems*, vol. 3. Prentice hall Upper Saddle River, NJ, 2002.

[78] C. Lanczos, *The variational principles of mechanics*. Courier Corporation, 2012.

[79] D. Ludovico, P. Guardiani, F. Lasagni, J. Lee, F. Cannella, and D. G. Caldwell, "Design of non-circular pulleys for torque generation: A convex optimisation approach," *IEEE Robotics and Automation Letters*, vol. 6, no. 2, pp. 958–965, 2021. *Copyright* © 2021, IEEE.

[80] V. Arakelian, "Gravity compensation in robotics," *Advanced Robotics*, vol. 30, no. 2, pp. 79–96, 2016.

[81] Y. Tojo, P. Debenest, E. F. Fukushima, and S. Hirose, "Robotic system for humanitarian demining," in *Robotics and Automation, 2004. Proceedings. ICRA'04. 2004 IEEE International Conference on*, vol. 2, pp. 2025–2030, IEEE, 2004.

[82] J. Boisclair, P.-L. Richard, T. Laliberté, and C. Gosselin, "Gravity compensation of robotic manipulators using cylindrical halbach arrays," *IEEE/ASME Transactions on Mechatronics*, vol. 22, no. 1, pp. 457–464, 2017.

[83] A. Rosyid, B. El-Khasawneh, and A. Alazzam, "Gravity compensation of parallel kinematics mechanism using torsional springs based on potential energy optimization," in *2018 11th International Symposium on Mechatronics and its Applications (ISMA)*, pp. 1–5, March 2018.

[84] G. Radaelli, R. Buskermolen, R. Barents, and J. Herder, "Static balancing of an inverted pendulum with prestressed torsion bars," *Mechanism and Machine Theory*, vol. 108, pp. 14 – 26, 2017.

[85] J. L. Herder, "Design of spring force compensation systems," *Mechanism and machine theory*, vol. 33, no. 1-2, pp. 151–161, 1998.

[86] J. Herder, *Energy-free Systems: Theory, Conception and Design of Statically Balanced Spring Mechanisms*. , 2001.

[87] V. Arakelian and Y. Zhang, "An improved design of gravity compensators based on the inverted slider-crank mechanism," *Journal of Mechanisms and Robotics*, vol. 11, no. 3, 2019.

[88] H. Kim and J. Song, "Multi-dof counterbalance mechanism for a service robot arm," *IEEE/ASME Transactions on Mechatronics*, vol. 19, pp. 1756–1763, Dec 2014.

[89] S. Yun, J. Seo, J. Yoon, H. Song, Y. Kim, and Y. Kim, "3-dof gravity compensation mechanism for robot waists with the variations of center of mass*," in *2019 IEEE/RSJ International Conference on Intelligent Robots and Systems (IROS)*, pp. 3565–3570, 2019.

[90] J. Reinecke, B. Deutschmann, A. Dietrich, and M. Hutter, "An anthropomorphic robust robotic torso for ventral/dorsal and lateral motion with weight compensation," *IEEE Robotics and Automation Letters*, vol. 5, no. 3, pp. 3876–3883, 2020.

[91] T. Rahman, R. Ramanathan, R. Seliktar, and W. Harwin, "A simple technique to passively gravity-balance articulated mechanisms," *ASME Journal of Mechanical Design*, vol. 117, pp. 655–658, Dec 1995.

[92] T. Morita, F. Kuribara, Y. Shiozawa, and S. Sugano, "A novel mechanism design for gravity compensation in three dimensional space," in *Proceedings 2003 IEEE/ASME International Conference on Advanced Intelligent Mechatronics (AIM 2003)*, vol. 1, pp. 163–168 vol.1, July 2003.

[93] V. L. Nguyen, C.-Y. Lin, and C.-H. Kuo, "Gravity compensation design of planar articulated robotic arms using the gear-spring modules," *Journal of Mechanisms and Robotics*, vol. 12, no. 3, 2020.

[94] V. L. Nguyen, C.-Y. Lin, and C.-H. Kuo, "Gravity compensation design of delta parallel robots using gear-spring modules," *Mechanism and Machine Theory*, vol. 154, p. 104046, 2020.

[95] N. Ulrich and V. Kumar, "Passive mechanical gravity compensation for robot manipulators," in *Robotics and Automation, 1991. Proceedings., 1991 IEEE International Conference on*, pp. 1536–1541, IEEE, 1991.

[96] I. Simionescu and L. Ciupitu, "The static balancing of the industrial robot arms: Part ii: Continuous balancing," *Mechanism and machine theory*, vol. 35, no. 9, pp. 1299–1311, 2000.

[97] G. Endo, H. Yamada, A. Yajima, M. Ogata, and S. Hirose, "A passive weight compensation mechanism with a non-circular pulley and a spring," in *Robotics and Automation (ICRA), 2010 IEEE International Conference on*, pp. 3843–3848, IEEE, 2010.

[98] D. Fedorov and L. Birglen, "Differential noncircular pulleys for cable robots and static balancing," *Journal of Mechanisms and Robotics*, vol. 10, no. 6, 2018.

[99] B. Kim and A. D. Deshpande, "Design of nonlinear rotational stiffness using a noncircular pulley-spring mechanism," *Journal of Mechanisms and Robotics*, vol. 6, no. 4, p. 041009, 2014.

[100] J. W. Rutter, *Geometry of Curves*. Chapman & Hall/CRC, 2000.

[101] A. J. McPhate, "Function generation with band mechanisms," *Journal of Mechanisms*, vol. 1, no. 1, pp. 85–94, 1966.

[102] M. Grant and S. Boyd, "CVX: Matlab software for disciplined convex programming, version 2.1." http://cvxr.com/cvx, Mar. 2014.

[103] M. Grant and S. Boyd, "Graph implementations for nonsmooth convex programs," in *Recent Advances in Learning and Control* (V. Blondel, S. Boyd, and H. Kimura, eds.), Lecture Notes in Control and Information Sciences, pp. 95–110, Springer-Verlag Limited, 2008. http://stanford.edu/~boyd/graph_dcp.html.

[104] C. Preissner, T. J. Royston, and D. Shu, "A high-fidelity harmonic drive model," *Journal of dynamic systems, measurement, and control*, vol. 134, no. 1, 2012.

[105] H. Olsson, K. J. Åström, C. C. De Wit, M. Gäfvert, and P. Lischinsky, "Friction models and friction compensation," *Eur. J. Control*, vol. 4, no. 3, pp. 176–195, 1998.

[106] M. Miyasaka, J. Matheson, A. Lewis, and B. Hannaford, "Measurement of the cable-pulley coulomb and viscous friction for a cable-driven surgical robotic system," in *2015 IEEE/RSJ international conference on intelligent robots and systems (IROS)*, pp. 804–810, IEEE, 2015.

[107] J. Coulibaly, M.-A. Chanut, S. Lambert, and F. Nicot, "Sliding cable modeling: An attempt at a unified formulation," *International Journal of Solids and Structures*, vol. 130, pp. 1–10, 2018.

[108] J. Jung, R. S. Penning, N. J. Ferrier, and M. R. Zinn, "A modeling approach for continuum robotic manipulators: Effects of nonlinear internal device friction," in *2011 IEEE/RSJ International Conference on Intelligent Robots and Systems*, pp. 5139–5146, IEEE, 2011.

[109] D. Ludovico, P. Guardiani, A. Pistone, J. Lee, F. Cannella, D. G. Caldwell, and C. Canali, "Modeling cable-driven joint dynamics and friction: a bond-graph approach," in *2020 IEEE/RSJ International Conference on Intelligent Robots and Systems, IROS 2020*, pp. 7285–7291, IEEE, 2020. *Copyright* © 2020, IEEE.

APPENDIX A

HARDWARE DESCRIPTION

A.1 CABLES

The cables selected for this application are made of a synthetic fibre called Zylon PBO whose mechanical properties are listed in table A.1. This fibre has the highest tensile strength and smallest elongation among synthetic fibres.

	Value	Unit	Description
d	3	mm	Diameter
m	6.5	g/m	Mass per unit lenght
E	270	GPa	Young modulus
R_m	5.8	GPa	Tensile strength

Table A.1 Zylon PBO cable mechanical properties.

The parameters of the four element model described in section 2.5 were estimated experimentally. Two samples have been tested with a length of (127 ± 1) cm and (165 ± 1) cm respectively. For each sample three experiments have been carried out. The identification procedure is composed of two steps. First the sample was loaded with a constant low velocity to estimate the stiffness K_1 through a linear regression. Then, to estimate the remaining parameters the

sample was loaded up to a maximum force of about 950 N to perform a non linear exponential fit on the free response of the system. Table A.2 lists the value of the identified parameters and the associated uncertainty.

	Value	Uncertainty	$e_{\%}$
K_1	2.933×10^5 N	1.73×10^4 N	5.9
c_2	5.78×10^9 Ns	1.33×10^9 Ns	23.0
K_3	7.67×10^6 N	1.74×10^6 N	22.7
c_3	9.08×10^7 Ns	2.23×10^7 Ns	24.6

Table A.2 Zylon PBO cables four element models parameters.

A.2 Force Sensors

The force applied by cables is measured using custom made force sensors which can be mounted directly on the cables. Their parameters are listed in table A.3

Parameter	Joint 5		Joint 6		Unit
	Top	Bottom	Top	Bottom	
Gain	787	764	363	393	N/V
Offset	-307	-152	-573	-580	N
Maximum force	2500	2500	1250	1250	N

Table A.3 Force sensors parameters

A.3 Absolute Encoders

The joint angular position is measured through the magnetic absolute encoders AkSim2 provided by Renishaw. This sensor have a resolution of 18 bits which corresponds to an angle of 2.4×10^{-5} rad.

A.4 Planar Cable-Driven Hyper-Redundant Robot

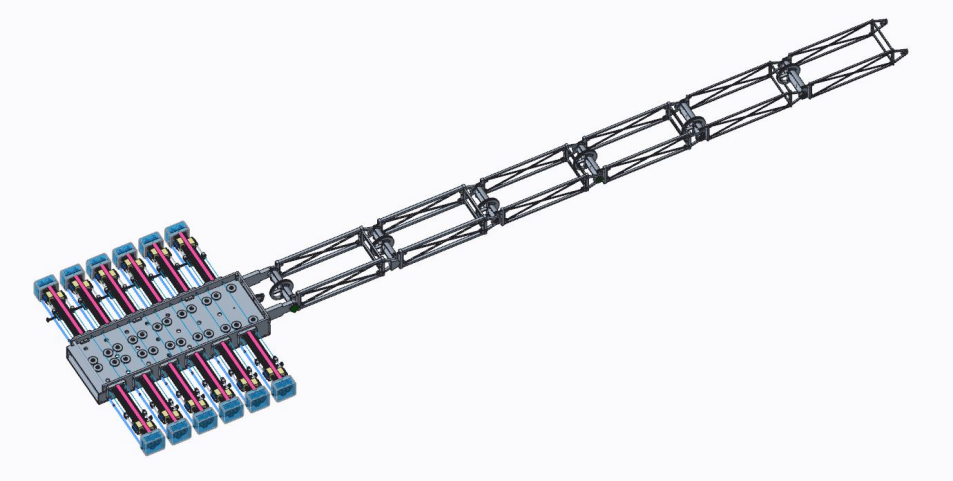

Figure A.1 Planar cable-driven hyper-redundant robot employed in the Ansaldo Energia project.

The cable-driven hyper-redundant robot designed for the Ansaldo Energia project is shown in Fig. A.1. The actuation box contains 6 linear actuators. Each actuator consists of a two poles SVTN B 01-3571 brushed DC motor and a three stages planetary gearbox, SVTG B 36, provided by Servotecnica. Each motor is controlled by an EPOS4 50/8 motor drivers provided by Maxon. They can be employed to control both brushless and brushed DC motors in torque, velocity and position mode. The linear motion is obtained through a screw-nut mechanism. Each module consists of a link, with length l, rigidly connected to a circular pulley of radius r. The mass, inertia about the z axis, and the location of the x-coordinate of the centre of mass of each module are defined as m, J_z, and CoM_x respectively. On one side the cables are fixed to the linear actuators, on the other side on circular pulleys to transmit the motion to the corresponding module. The cables have a length l_c and are preloaded with a force T_p. The main parameters of the robotic systems here presented are listed in table A.4.

	Joint 1	Joint 2	Joint 3	Joint 4	Joint 5	Joint 6	Unit
Geared motor							
R_m	4.198	2.434	2.397	2.325	2.546	2.497	Ω
L_m	1.139	0.691	0.682	0.694	0.690	0.679	mH
k_m	55.989	58.048	56.323	56.341	58.773	56.697	mNm/A
J_m	72.85	72.85	72.85	72.85	72.85	72.85	gcm^2
c_m	5.6280	5.8349	5.6615	5.6633	5.9078	5.6991	μNms/rad
ω_n	6118	6118	6118	6118	6118	6118	rpm
i_n	4.16	4.16	4.16	4.16	4.16	4.16	A
J_g	12	12	12	12	12	12	gcm^2
N_g	212.34	212.34	212.34	212.34	212.34	212.34	-
Motor driver							
K_p	9.030	5.219	5.139	4.969	5.477	5.370	V/A
K_i	30.945	17.147	16.849	15.578	18.789	18.365	V/(mAs)
V_{max}	48	48	48	48	48	48	V
i_{max}	8.32	8.32	8.32	8.32	8.32	8.32	A
Screw-nut mechanism							
d	15	15	15	15	15	15	mm
ϕ	0.471	0.471	0.471	0.471	0.471	0.471	rad
α	0.064	0.064	0.064	0.064	0.064	0.064	rad
p	3	3	3	3	3	3	mm/rev
Module							
m	2.16	2.16	1.55	1.55	1.3	1.3	kg
J_z	0.067	0.067	0.043	0.043	0.030	0.030	$kg\,m^2$
CoM_x	197	197	170	170	136	136	mm
l	500	500	500	500	500	500	mm
r	55	55	55	55	55	55	mm
l_c	1	1.5	2	2.5	2.9	3.4	m
T_p	990	825	610	400	210	150	N

Table A.4 Planar cable-driven hyper-redundant robot parameters.

A.5 Gear Joint Experimental Setup

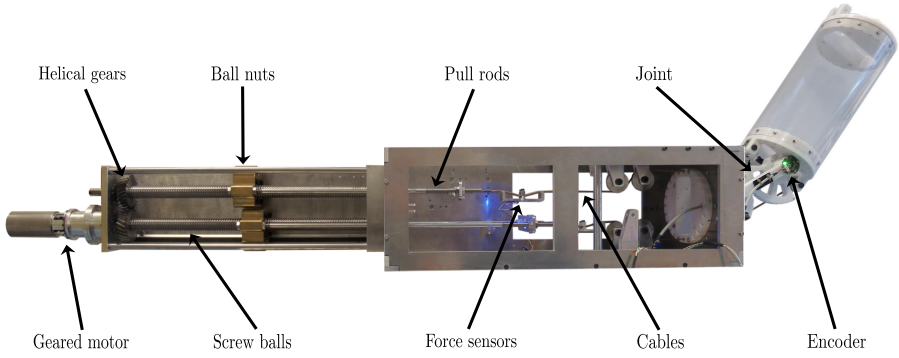

Figure A.2 Hardware setup for the experiments with the prototype of the cable-driven joint and its actuation system.

The prototype used to identify the friction parameters described in chapter 5, shown in Fig. A.2, consists of a gear joint driven by a linear actuator able to move two twin cables in opposite directions and a pulley mechanism that aligns the cables with the joint geometry. Two force sensors are used to measure the force applied to the joints. The cables are fixed by splicing around the anchor points in pulling rods and flanges. The actuation system is composed of a Maxon ECi52 brushless motor coupled to an harmonic gear. The geared motor, controlled by an EPOS4 50/8 motor driver, transfers the motion to the first ball-screw, which moves a helical gear mounted on it. The two gears with ratio 1:1 allow the two ball-nuts to move with the same speed but in opposite direction. A preliminary prototype of a gear joint, described in section 5.1.2, was 3D printed in polycarbonate. The main parameters of the setup for testing the gear joint prototype are listed in table A.5

Coefficient	Value	Unit	Description
		Geared motor	
R_m	0.444	Ω	Motor resistance
L_m	0.471	mH	Motor inductance
k_m	102.4	mNm/A	Motor torque constant
J_m	349.88	gcm^2	Total inertia
c_m	10.319	mNm/s	Motor viscous friction
ω_n	3610	rpm	Motor nominal velocity
i_n	5.44	A	Motor nominal current
N_g	1 : 80	-	Gear reduction ratio
N_s	5	mm	Screw pitch
		Motor driver	
K_p	2.134	V/A	Proportional gain
K_i	9.493	V/(mAs)	Integral gain
V_{max}	48	V	Maximum voltage
i_{max}	10.88	A	Maximum current
		Gear joint	
m_1	0.217	kg	1^{st} link mass
J_1	0.0007	kgm^2	1^{st} link inertia
m_2	0.806	kg	2^{nd} link mass
J_2	0.00016	kgm^2	2^{nd} link inertia
d_{11}	47	mm	$\overline{O_1P}_{c_{m_1}}$
d_{12}	103	mm	$\overline{O_2P}_{c_{m_1}}$
d_{21}	12	mm	$\overline{O_2P}_{c_{m_2}}$
d_{22}	338	mm	$\overline{P_{ee}P}_{c_{m_1}}$
r	65	mm	Anchor point distance

Table A.5 Gear joint setup parameters.

APPENDIX B

CONTROLLER DESIGN PARAMETERS

The experiments discussed in 3.3 were performed on a two links cable-driven robot. In this appendix, the derivation of both the inner and outer loop controller parameters are detailed.

B.1 INNER FORCE LOOP

As described in section 3.2.1 the first step to derive the control law consists of defining the nominal plant and the uncertainty model of the system. Using the parameters listed in appendix A.4 it is possible to derive the actuators and cables transfer functions which take on the following structure:

$$G_p = K_{p_{dc}} \frac{1 + \frac{s}{z_p}}{\left(1 + \frac{s}{p_{p_1}}\right)\left(1 + \frac{s}{p_{p_2}}\right)}, \tag{B.1}$$

$$G_a = K_{a_{dc}} \frac{1 + \frac{s}{z_a}}{\left(1 + \frac{s}{p_{a1}}\right)\left(1 + \frac{s}{p_{a_2}}\right)\left(1 + \frac{s}{p_{a_3}}\right)}. \tag{B.2}$$

Table B.1a lists the coefficients of the transfer functions for both the joints considered.

Since

$$\begin{aligned} 1+\frac{s}{p} &\approx \frac{s}{p} \quad \text{if} \quad p << 0, \\ 1+\frac{s}{p} &\approx 1 \quad \text{if} \quad p >> \omega_n, \end{aligned} \tag{B.3}$$

the nominal transfer functions are obtained neglecting the high frequency poles and zeros, and approximating low frequency poles as integrators obtaining transfer functions with the following structure

$$\begin{aligned} G_{p_n} &= K_{p_n} \frac{1+\frac{s}{z_p}}{s\left(1+\frac{s}{p_p}\right)}, \\ G_{a_n} &= K_{a_{dc}} \frac{1}{\left(1+\frac{s}{p_a}\right)}. \end{aligned} \tag{B.4}$$

Their parameters for both the joints are listed in table B.1b. Let now consider

	Joint 5	Joint 6
	G_p	
$K_{p_{dc}}$	3.96×10^9	3.38×10^9
z_p	8.44×10^{-2}	8.44×10^{-2}
p_{p_1}	4.89×10^{-5}	4.89×10^{-5}
p_{p_2}	8.76×10^{-2}	8.76×10^{-2}
	G_a	
$K_{a_{dc}}$	9.31×10^{-5}	9.31×10^{-5}
z_a	3.43×10^3	3.42×10^3
p_{a_1}	6.82×10^{-1}	6.58×10^{-1}
p_{a_2}	3.37×10^3	3.35×10^3
p_{a_2}	8.26×10^3	8.23×10^3

(a) Real plant parameters.

	Joint 5	Joint 6
	G_{p_n}	
K_{p_n}	1.71×10^5	1.65×10^5
z_p	8.44×10^{-2}	8.44×10^{-2}
p_p	8.76×10^{-2}	8.76×10^{-2}
	G_{a_n}	
K_{a_n}	9.31×10^{-5}	9.31×10^{-5}
p_{a_1}	6.82×10^{-1}	6.58×10^{-1}

(b) Nominal plant parameters.

Table B.1 Plant transfer function parameters.

the uncertainty bounds given by the identification of the cables parameters. As stated in section 3.2.1 it possible to compute the weighting functions related to

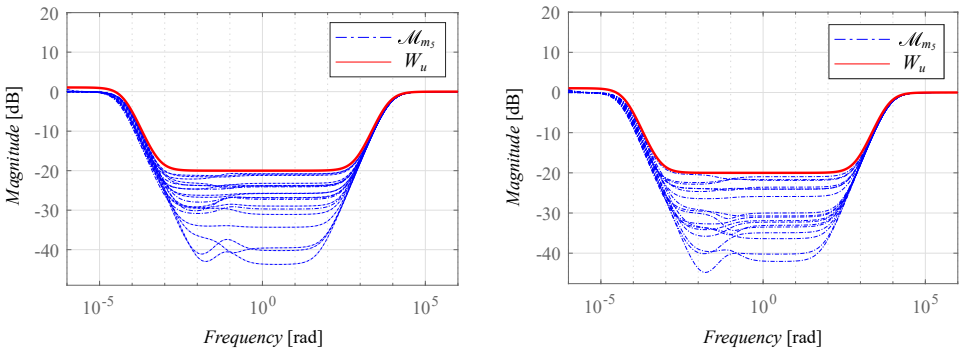

(a) W_{u_5} (b) W_{u_6}

Figure B.1 Uncertainty model for joint 5 and 6.

the model uncertainty using (3.13) and their values are

$$W_{u_5} = \frac{\left(s+6.36\times10^{-4}\right)\left(s+7.2\times10^{2}\right)}{\left(s+5.6\times10^{-5}\right)\left(s+7.2\times10^{3}\right)}, \tag{B.5}$$

$$W_{u_6} = \frac{\left(s+6.36\times10^{-4}\right)\left(s+7.2\times10^{2}\right)}{\left(s+5.6\times10^{-5}\right)\left(s+7.2\times10^{3}\right)}. \tag{B.6}$$

Figure B.1 shows the uncertainty model for both the joints considered.

The second step in defining the control low consists of translating the time domain requirements into weighting function in frequency domain. The a priori information about the input and disturbance signals described in (3.6) are listed in table B.2. Since the time domain requirements are the same for both the joints considered, also the weighting functions W_1 and W_2 are the same and their value is

$$W_1 = 0.69\frac{s^2+4.99s+12.47}{(s+0.14)\left(s+2.5\times10^{-5}\right)}, \tag{B.7}$$

$$W_3 = 1000\frac{s^2+83.34s+3473}{s^2+2802s+3.92\times10^{6}}. \tag{B.8}$$

	Value	Unit
r_0	300	N/s
d_{f_0}	1×10^{-2}	-
d_{a_0}	2×10^{-3}	rad/s
d_{p_0}	1	N
ω_p	0.25	rad
d_{s_0}	1	N
ω_s	628	rad

Table B.2 Input signals and disturbances a priori information.

Instead W_2 is computed considering the actuator dynamics. Thus,different weighting functions, one for each joint, are obtained:

$$W_{2_5} = 0.67\frac{s+0.682}{s+682}, \tag{B.9}$$

$$W_{2_6} = 0.67\frac{s+0.658}{s+658}. \tag{B.10}$$

The solution of the optimisation problem given by the Robust Control Toolbox of Matlab, after a appropriate simplification of the high-frequencies poles, returns the following controllers

$$G_{c_5} = 880.85\frac{(s+1.6)(s+0.682)}{(s+0.144)\left(s^2+52.55s+1376\right)}, \tag{B.11}$$

$$G_{c_6} = 873.24\frac{(s+1.61)(s+0.658)}{(s+0.144)\left(s^2+48.73s+1180\right)}. \tag{B.12}$$

Finally Fig. B.2 shows the performances index in frequency domain obtained with the controllers G_{c_5} and G_{c_6}. The step and steady state response requirements are compared with the results obtained with the proposed controllers. Their value are listed in table B.3.

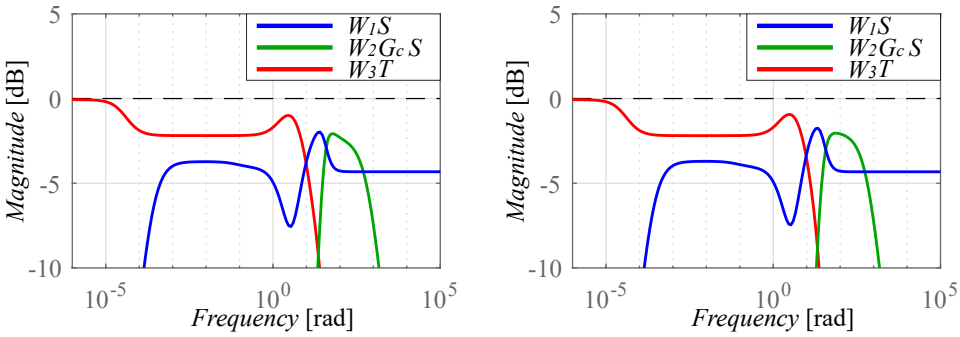

(a) Joint 5 performances.

(b) Joint 5 performances.

Figure B.2 Performances in frequency domain.

	Required	Joint 5	Joint 6	Unit
$e_{\Delta F_c}$	5	3.7	3.7	N
$\Delta F_{c_{dp}}$	10×10^{-3}	5.93×10^{-3}	5.95×10^{-3}	N
$\Delta F_{c_{ds}}$	10×10^{-3}	4.49×10^{-5}	3.75×10^{-5}	N
t_r	0.5	0.129	0.134	s
$t_{s,2\%}$	1.5	1.440	1.461	s
$\hat{s}$	15	13.0	13.7	%

Table B.3 Inner force loop steady state and step response.

B.2 Outer Position Loop

As demonstrated in section 3.2.2 to guarantee the stability of the outer loop K_P and K_D have to be symmetric and positive definite. In the experiments described in section 3.3 their value is selected as

$$K_P = \begin{bmatrix} 225 & 0 \\ 0 & 225 \end{bmatrix}, \quad K_D = \begin{bmatrix} 21.21 & 0 \\ 0 & 21.21 \end{bmatrix}. \tag{B.13}$$

APPENDIX C

SOFTWARE ARCHITECURE

The software architecture developed for this application is based on National Instrument CompactRIO system which consists of a processor running a Linux real-time operating system and a chassis that contains a user-programmable FPGA. On the FPGA the low level control logic and communication protocol are implemented, using external modules, to read sensors data and send the actuators command. FPGAs allow managing hard real-time tasks thanks to their ability to solve most operations in a single clock cycle. Furthermore, this technology allows hardware reconfiguration that, in the development phase, provides the necessary flexibility to perform changes in the hardware architecture, such as adding sensors measurement or implementing different communication protocols.

The magnetic absolute encoders described in appendix A.3 transmit data through BiSS-C, a serial point to point communication protocol. Since the point to point communication requires a cable for each node in the network, the encoder's data are acquired by a Texas Instrument Tiva C microcontroller with a sample rate of 16667 Hz to avoid to wire up a cable for each encoder along the whole robot structure. The acquired data are filtered and processed to numerically estimate the joint velocity. The microcontrollers are connected in daisy chain and transmit the joint position and velocity to the FPGA of the CompctRIO through a CAN Bus.

A second and independent CAN Bus is implemented to establish the communication with the motor drivers. In this case the standard CANopen protocol is employed to read the motor states and send the commands.

The force sensors described in appendix A.2 return analog signals which are read by the FPGA with a sample rate of 5000 Hz

The proposed control algorithm runs on the real-time processor at a frequency of 200 Hz. The real-time target manages the communication with both the FPGA and the host PC where a graphical user interface is implemented to drive the robot and log the data. Figure C.1 shows a schematic of the software architecture employed in this work.

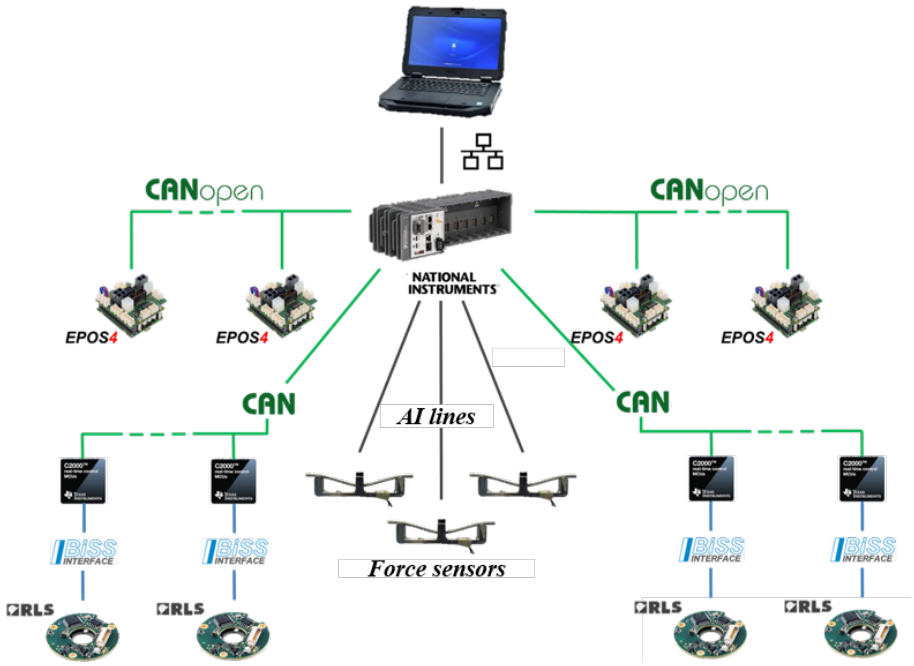

Figure C.1 Software architecture schematic.